THE UNIVERSITY *of* EDINBURGH

THE UNIVERSITY of EDINBURGH
Institute of Materials and Processes
School of Engineering

Surface nano-patterning using the coffee-stain effect

Alexandros Askounis

A thesis submitted to the University of Edinburgh
for the Degree of Doctor of Philosophy, 2014

Declaration

The candidate confirms that the work submitted is his own, except where work which has formed part of jointly-authored publications has been included. The contribution of the candidate and the other authors to this work has been explicitly indicated below. The candidate confirms that appropriate credit has been given within the thesis where reference has been made to the work of others.

Alexandros Askounis

Acknowledgements

I would like to dedicate this part of my thesis to acknowledge all the people who have supported me during my time in Edinburgh. Their support was paramount in the completion of this work.

First and foremost, I would like to thank my supervisor Prof. Khellil Sefiane who offered me the opportunity to undertake my PhD studies in his group. His guidance and advice were invaluable during each step of this work. He has always made himself available to even the smallest of my concerns, no matter how busy he may have been.

Secondly, I would like to thank Dr. Vasileios Koutsos. He has always been open to discuss about anything, scientific or not. His insights into this work have helped me approach various issues from different angles. Furthermore, I would like to show my appreciation to Prof. Martin E.R. Shanahan whose friendly manner and fruitful discussions made the composition of most of this work easier. The Eric Birse Trust should also be acknowledged for its financial support during these years. Lastly, I would also like to thank Jovana and Dani who have been two amazing colleagues and "lab-mates".

I have also met a number of people during my period in Edinburgh whom I came to call friends and who transformed everyday routine at the university into an enjoyable experience and of course proved to be a source of amusement outside it. To name but a few: Ares, Pedro, Alex, Eduardo, Peyman, Anna, Zoe, Enzo, Davide, Dimitris, Sotiris, Nelly, Adrian, Italo, Miguel, Pedro, Unai, Esme, Apostolos, Meropi and George.

Last but not least, I would like to specially thank my parents Vaso and Kostas for their unlimited support and love during my PhD, albeit the distance.

Abstract

Addition of nanopacticles in a base solvent leads to suspensions with enhanced physio-chemical properties, compared to base solvent. This new type of suspensions is called nanofluids, with applications ranging from biomedicine to automotives. As a consequence extensive research is being conducted in the field, in particular, on the evaporation of these fluids as it leads to well-defined and highly ordered coffee-rings. However, the exact physics governing this phenomenon remain elusive. The goal of this experimental investigation is to elucidate how various parameters affect the progression of nanofluid coffee-stain formation.

Examination of the coffee-ring structuring, produced by the *free* evaporation of sessile droplets containing nanoparticles, revealed an unexpected, disordered region at the exterior edge of the ring. A self-assembly mechanism with two components, particle velocity and wedge constraints, was proposed to describe the deposition of particles at contact lines of evaporating drops.

Environmental pressure was used as a method to control particle crystallinity in the coffee-rings. Essentially, evaporation rate and pressure were found to be inversely proportional. Macroscopically, lowering pressure led to a transition from “stick-slip” to constant pinning. Nanoscopically, lowering pressure promoted crystallinity. Findings supported the proposed, in this thesis, particle self-assembly mechanism.

Particle aspect ratio and flexibility were subsequently examined. Pinning strength was found to be a function of particle aspect ratio and rigidity, leading to constant pinning. The proposed, in this thesis, particle self-assembly mechanism was found to be applicable to a variety of aspect ratios and flexibilities. Lastly, particulate crystals grew following different pathways depending on particle flexibility.

Contents

List of publications

1. Askounis A, Sefiane K, Koutsos V, Shanahan MER,
   Effect of particle geometry on triple line motion of nano-fluid drops and deposit nano-structuring.
   Advances in Colloid and Interface Science, **In Press**

2. Askounis A, Sefiane K, Koutsos V, Shanahan MER.
   The effect of evaporation kinetics on nanoparticle structuring within contact line deposits of volatile drops.
   Colloids and Surfaces A: Physicochemical and Engineering Aspects, **2014**, 441, 855-866.

3. Askounis A, Sefiane K, Koutsos V, Shanahan MER.
   Structural transitions in a ring stain created at the contact line of evaporating nanosuspension sessile drops.
   Physical Review E, **2013**, 87, 012301.

List of figures

Chapter 1 Introduction

The ability of a liquid to wet a solid surface is an everyday phenomenon manifesting from rain drops on glass windows or plant leaves to paints, inks etc. Essentially, when a droplet of liquid encounters a solid surface it will attempt to minimise its energy and reach thermodynamic equilibrium between the three phases acting on the contact line (TL) of the droplet. This equilibrium is fundamentally the balance between the interactions of the liquid-solid, solid-vapour and liquid-vapour pairs.

Young was the first, back in the 1805, who related this balance of phases with the observed contact angle of the liquid front [1], which became the foundation of the field. Thorough investigations based on this statement allowed some insight into the physics of the phenomenon. For example, in a series of his contributions, de Gennes described extensively the motion of a liquid front [2, 3], sparking further research with potential applications such as lithography [4], microfluidics [5] and even in the formation of polymer films [6], to present but a few.

Energy minimisation or wetting of a liquid-solid-gas system, such as a water drop resting on a solid surface, is attained almost instantaneous, compared to the timescale of other processes such as evaporation. Typically, evaporation of the liquid should occur whenever the liquid molecules at the air-liquid interface have sufficient energy to escape and phase change from liquid to vapour. At the same time, the environment around the droplet should not be saturated with liquid vapour [7].

Droplet evaporation may seem simple at first, however it is a relatively complex system, which has attracted considerable scientific interest over the past years [8-12]. Essentially, droplet evaporation can be summarised as heat and mass transfer between the phases in the system. Parameters affecting the process such as wettability [7, 13], pressure [14] and temperature [15-17] have been investigated. The addition of particulate within the droplet has also attracted considerable scientific interest recently, as it enhances the properties of the base fluid [18]. Deegan and coworkers paved the way into the evaporation process of colloidal droplets and the patterns left behind [19-21]. Briefly, particulate pinned the TL of drops, inducing a convective outward flow which deposited the rest of the solute at the TL, thus forming coffee-rings [19-21]. This pioneering work led to investigations for potential applications in various fields such as inkjet printing [22], photovoltaics [23], the production of DNA microarrays [24] and even blood diagnosing techniques [25-27], where well defined patterned surfaces are required.

Stemming from the above mentioned findings, another area which has recently started evolving is the evaporation of nanofluids. Nanofluids are suspensions of particles with at least one dimension in the nanoscale (< 100 nm) dispersed in a medium and exhibiting enhanced properties compared to the base fluid [18]. Based on their unique properties, research into various potential applications ranging from automotives [28], industrial [29, 30] and microchips [31, 32] cooling, biomedical and detergents [33]. The evaporation of nanofluid droplets was thoroughly investigated both theoretically [34, 35] and experimentally [36-40].

Generally, spherical particles tend to form two-dimensional crystalline structures [41]. Therefore, drop drying can be employed as a "bottom-up" assembly technique to produce highly-ordered structures, similar to building structures with Lego bricks. Investigation into the exact structuring of particles within ring-stains showed that the particles tend to self-assemble within in sequential hexagonal and square packed regions with deposit thickness, in an attempt for particles to achieve the densest possible packing [42-46] . Some irregularities were also reported in terms of disordering at either the exterior [47, 48] or the interior [49] of the rings. Understanding the physics behind particle ordering within well-defined patterns could have potential biosensing [50, 51], optical [52, 53] applications and surface patterning applications such as lithography [54-56].

Although the applicability of the drop drying technique as a method to produce well-defined and ordered structures on surfaces cannot be disputed, still the dynamics governing the evaporation process and in extension the self-assembly of particles, remain somewhat elusive. It is the purpose of this thesis to present, analyse and discuss how a number of parameters affect the evaporation process of a nanofluid droplet and its resulting nanostructures. Hence, this thesis is divided in the following 8 chapters:
In chapter 1 and 2, the relevant theoretical background in wetting, droplet evaporation and particle self-assembly into ordered structures is discussed. These chapters should provide the reader with the necessary knowledge in order to understand the concepts discussed in this thesis.

In chapter 3, a detailed description on the preparation of the surfaces, particles, and suspensions used in this experimental study are presented. Additionally, the experimental processes and apparatuses are presented.

In chapter 4, insight into the effect of monodisperse nanoparticles on the coffee-ring formation mechanism is provided. In detail, the evolution of the evaporation is analysed and discussed. Nanoscale investigations unveiled particle nanostructuring tendencies near the edge of the coffee-ring and an unexpected disordered region at the edge of the coffee-stain. Increasing evaporation rate was found to promote particle crystallinity. Combination of experimental data with theoretical arguments allowed the proposition of a tentative particle self-assembly mechanism within coffee-rings.

In chapter 5, the effect of environmental process on coffee-stain formation mechanism is thoroughly examined. Pressure increases the evaporation rate of the droplet which induces a stronger outward flow and hence particle deposition rate. In turn, increased deposition rate results in promotion of droplet pinning. Quantification of the hysteretic energy barrier of each droplet shows a direct relation between evaporation/deposition rate and pinning strength. At the nanoscale, increase in deposition rate promoted crystallinity until a threshold pressure value. These findings further support the proposed particle self-assembly theory proposed in the previous chapter.

In chapter 6, a comparison of particle shape on the evaporative behaviour, resulting coffee-stain patterns and particle self-assembly behaviour is conducted. A wide variety of shapes categorised according to aspect ratio were studied, the actual particles being nanospheres, carbon nanotubes and graphene platelets. Increasing aspect ratio, promoted the pinning of the droplets. Nanoscopic examination of the resulting patterns, revealed that all particle shapes follow the previously proposed self-assembly mechanism granting it a universal character.

In chapter 7, the effect of particle flexibility on the evaporation process of droplets and on the deposition patterns is illustrated. Two different, in length, DNA strands were chosen, one above (flexible) and one below (rigid) its persistence length. Results show that particle flexibility plays a major role on the evaporation process, resulting ring-stains and particle structuring within. Quantification of energy barriers pinning each case exhibit an inverse relation between flexibility and pinning strength. At the nanoscale, flexibility promotes particulate alignment at the TL and affects crystal patterns.

In chapter 8, we conclude the findings of this experimental study. With consideration of these closing remarks, future work is also suggested to answer questions raised by this experimental study.

Chapter 2 Theoretical background

2.1. Wetting and droplet shape

Wetting is an everyday phenomenon, which can be defined as the ability of a liquid to wet/spread on a solid surface or another immiscible liquid. Manifestation of this phenomenon is ubiquitous in everyday life, from drops of rains resting on glass windows to inks and crops spraying. Given its ubiquitous nature the understanding of the complex physics behind this system could provide useful to various applications [18].

Fundamentally, wetting is the balance between the three phases, solid-liquid-vapour, acting on the interface of a liquid front resting on a solid surface. The liquid front will attempt to minimise its energy or attain thermodynamic equilibrium between these three phases. Depending on this balance, the liquid will either completely wet, corresponding to $\theta = 0^o$, dewet, corresponding to $\theta = 180^o$ or partially wet, $0^o < \theta < 180^o$ the surface. At equilibrium, the balance between the gas-liquid, γ_{GL}, liquid-solid, γ_{LS}, and gas-solid, γ_{GS}, surface tensions should dictate the shape of the droplet and the contact angle, θ, shown in Figure 2.1. Young was the first that related θ and the three phases in a statement in his essay about the cohesion of fluids [1]. The mathematical description of Young's statement is widely attributed to Dupré [57]:

$$\boldsymbol{\gamma_{GL} cos\theta = \gamma_{GS} - \gamma_{LS}} \tag{2.1}$$

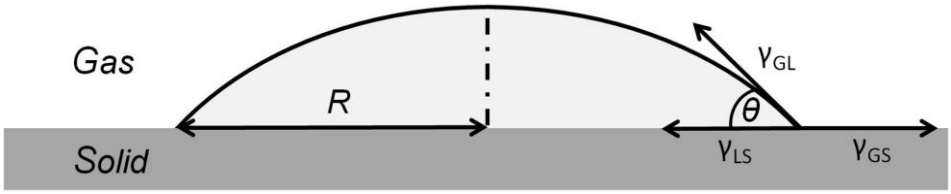

Figure 2.1: Schematic illustration of a sessile drop deposited on a solid surface, showing the three surface tensions acting on the TL and the corresponding contact angle, θ, and radius, R.

Provided that the droplet is sufficiently small, *i.e.* radius, R, is smaller than the capillary length of the liquid, $\kappa^{-1} = \sqrt{\gamma/\rho g}$ where γ, ρ and g are respectively surface tension, density and gravitational acceleration, then gravitational effects can be neglected and the droplet attains the shape of an axis-symmetric spherical cap, termed sessile drop.

2.2. Contact angle hysteresis

The value of the contact angle of a droplet is indicative of the wetting of a surface from a liquid, and is related to both compositional [58-60] and topographical [61-63] surface heterogeneities. Since most solids are never truly homogeneous, the surface defects interfere with the TL, making it difficult to determine the exact contact line of the drop. Assuming that θ lies somewhere between the advancing, θ_a, and receding, θ_r, contact angle, $\theta_a > \theta > \theta_r$, we can thus calculate the contact angle or wetting hysteresis, $H = \theta_a - \theta_r$ [64]. An example of θ_a and θ_r is given in Figure 2.2 (a, b), respectively. Contact angle hysteresis can vary widely between small values of ~ 2^o [65], which can be considered to be within experimental error, to larger values of 10^o [66, 67].

One of the first theoretical attempts to describe contact angle/wetting hysteresis was developed by Joanny and de Gennes [2]; albeit for the simple case of a straight liquid front. Initially, they developed a model accounting for the liquid front encountering a single, spherical defect which anchored the TL. Due to the anchoring, the TL deformed around the defect and returned to linearity away from it, as seen in Figure 2.2 (c). Subsequently, this model was developed further in order to incorporate a larger number of defects varying in size and geometry. Eventually, they successfully described the case of surface roughness. Later, de Gennes based on this model, developed a theory describing in depth the wetting of solids on liquids [3], which became the basis for considerable research in this area and resulted in the description of more complex cases [68-71].

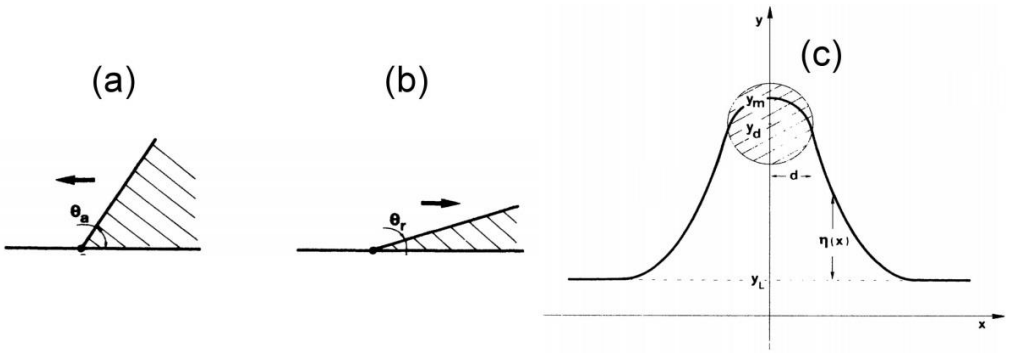

Figure 2.2: Schematic representation of an advancing (a) and a receding (b) liquid front and the corresponding angles and (c) TL anchoring on a spherical defect. Adapted from [3].

A model was later developed in order to assess the effect of a single and two defects, seen in Figure 2.3 (a) and (b) respectively, on a slightly deformed axisymmetric drop

[72]. This model also allowed the prediction of the shape and the contact angle of the drop. However, considering the complexity of the system, gravitational effects were neglected and only small contact angles were considered. Still, this model could be applied in a number of systems of sessile drops, in which gravitational effects are negligible. In addition, in systems with low contact angles, hysteretic effects are most apparent.

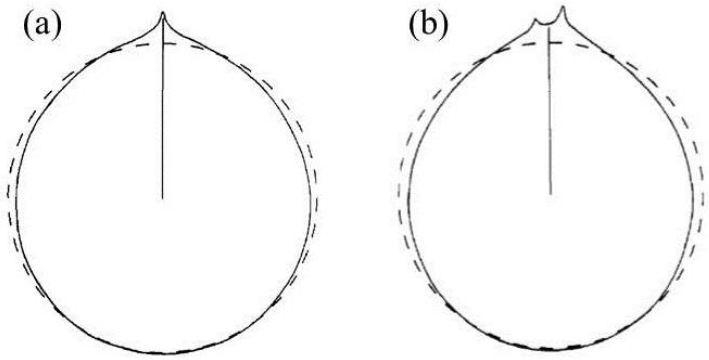

Figure 2.3: Schematic illustration of the deformation of an axisymmetric droplet from (a) a single and (b) two defects of different sizes. Dashed lines correspond to equilibrium shape. Image adapted from [23].

2.3. Pure liquid sessile droplet evaporation

Having established the fundamentals of droplet shape and contact angle hysteresis we will now describe the process of the evaporation of sessile droplets, which is the main focus of this thesis. Essentially, if the environment around the droplet is not saturated with the liquid of the droplet, then evaporation occurs. During evaporation, molecules are transferred from the liquid surface to the surrounding atmosphere. Experimental observations of the evaporation of organic liquids resting on polymer surfaces revealed

three distinct evaporation modes [9], which are schematically presented in Figure 2.4. These three modes are:

1. Constant contact angle, C*CA.* The droplet evaporates with a constant shape (height over radius aspect ratio). The constant shape results in constant angle and decreasing radius. This evaporation mode is considered as the ideal evaporation behaviour. In particular, both the advancing, θ_a, and receding, θ_r, contact angle are equal; absence of any contact angle hysteresis. The actual drop shape is dictated only by the surface tension balance acting at the TL.
2. Constant contact radius, CCR. The droplet evaporates with a constant contact area and hence radius, due to TL pinning/anchoring. Simultaneously, contact angle is constantly diminishing in order to accommodate the volume loss. This mode of evaporation originates in contact angle hysteresis.
3. Mixed mode. Evaporation occurs with either or both contact angle and radius decreasing. One of the most common behaviours is that of an initial CCR stage until the contact angle attains the value of the receding contact angle, θ_r, at which point evaporation enters a CCA regime.

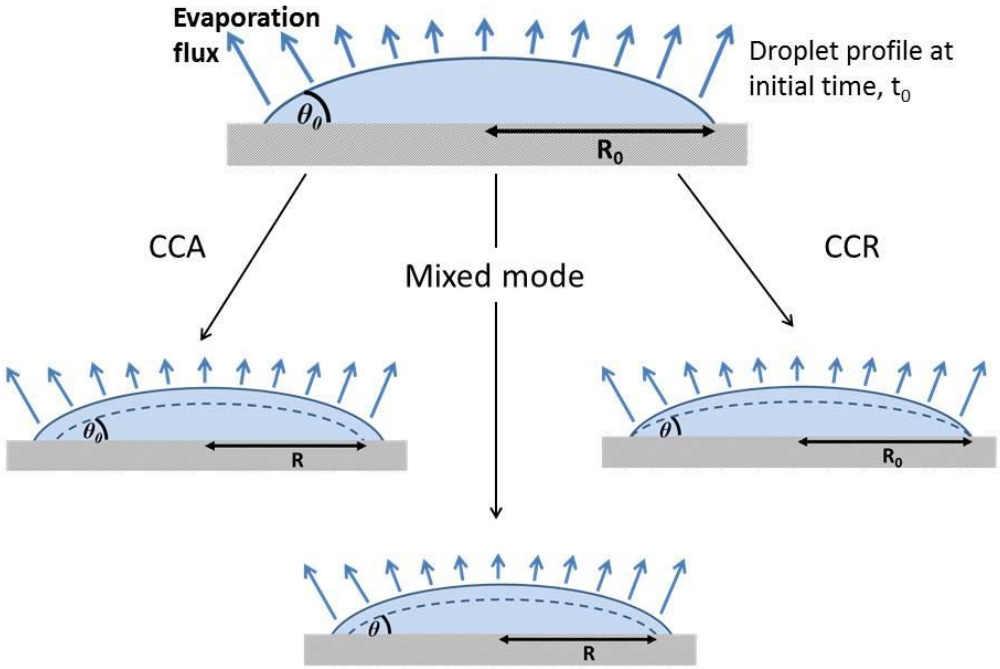

Figure 2.4: Schematic representation of the three evaporative modes: Constant contact angle, CCA, constant contact radius, CCR, and the mixed one with characteristics of both modes. Dashed lines represent the droplet profile soon after t_0.

A drying pure water droplet exhibited an evaporative behaviour with alternating cycles of CCR and CCA, as seen in Figure 2.5 [8] Initially, during period (t_0-t_1), the droplet evaporates under the CCR regime. Upon θ attaining the value of the receding contact angle, $\theta = \theta_r$, then the evaporation enters the CCA mode, period (t_1-t_4), until it finally enters a second CCR mode until full evaporation (t_4-t_5) [8].

.

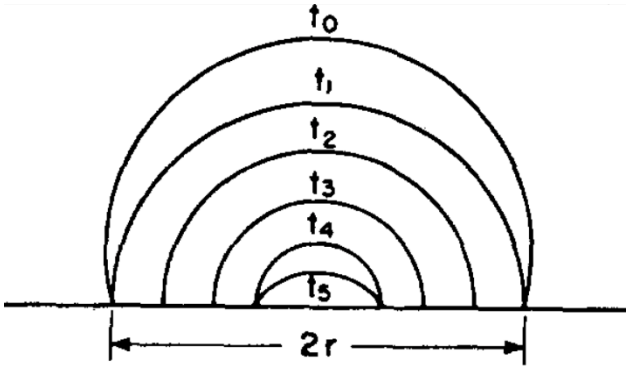

Figure 2.5: Evaporation stages of a pure water drop resting on a smooth, flat surface. Image taken from [8].

Picknett and Bexon further investigated this unexpected evaporation behaviour both theoretically and experimentally [9]. Experimentally, they investigated the evaporation of a methyl acetoacetate drop which exhibited three distinct evaporation modes: the CCR and CCA, as discussed above, and a mixed mode as discussed above. They also developed a theory in order to predict the mass loss/ evaporation rate and droplet lifetime of sessile droplets evaporating under either the CCR or the CCA regime. The theory was based on Maxwell's equation describing the evaporation of a sphere in an infinite medium, where an analogy between diffusive flux and electrostatic potential, as both satisfy Laplace equation, was used:

$$dW/dt = -4\pi Dr(c_0 - c_i) \quad (1.2)$$

, where dW/dt is mass rate change of the drop, R is the radius, D is the diffusion constant of the vapour in air, and c_0 and c_i are vapour concentration close and away from the sphere respectively. Theoretical results were in good agreement with experimental ones and with results from the literature. Interestingly, liquid mass loss rate was reported to be a function of both contact angle and radius [9].

Birdi *et al.*, shed further light into the evaporation of pure liquid sessile drops [10]. Experimentally, they measured the evaporation rate of a water drop by measuring the weight loss over time. The evaporation rate of the water droplet was found to be linear over time, meaning that the process is stationary. Experimenting with different substrates and liquids revealed a relationship between evaporation rate and surface wetting. Notably, wetting contact angles, $\theta < 90^o$, exhibited linear evaporation rates whereas non-wetting liquids, $\theta > 90^o$, showed non-linear rates [10].

Bourgès and Shanahan extensively studied the evaporation of pure liquid sessile droplets on polymer surfaces [7, 13]. Aspects such as surface roughness and atmospheric conditions (saturation of atmosphere around the droplet with liquid vapour) and a number of different liquid-solid pairs were probed. In most cases, the droplets evaporated following the three distinct modes reported previously by Picknett and Bexon [9]. As demonstrated in Figure 2.6, during stage I and II, the droplet evaporated under the CCR regime. The difference between these two stages is the saturation of the atmosphere with vapour during stage I. It should be noted that during this stage all measured quantities $(\text{diameter}, d, \text{height}, h, \text{contact angle}, \theta)$ remained constant, while they followed the typical CCR when the atmosphere was no longer saturated. Once $\theta = \theta_r$ (with the value of θ_r measured separately by slowly withdrawing liquid with a syringe), the evaporation entered stage III. In this stage evaporation followed the CCA regime. Eventually, the droplet shrank to such an extent

that shape could no longer be followed, giving rise to the erratic behaviour of stages IV.

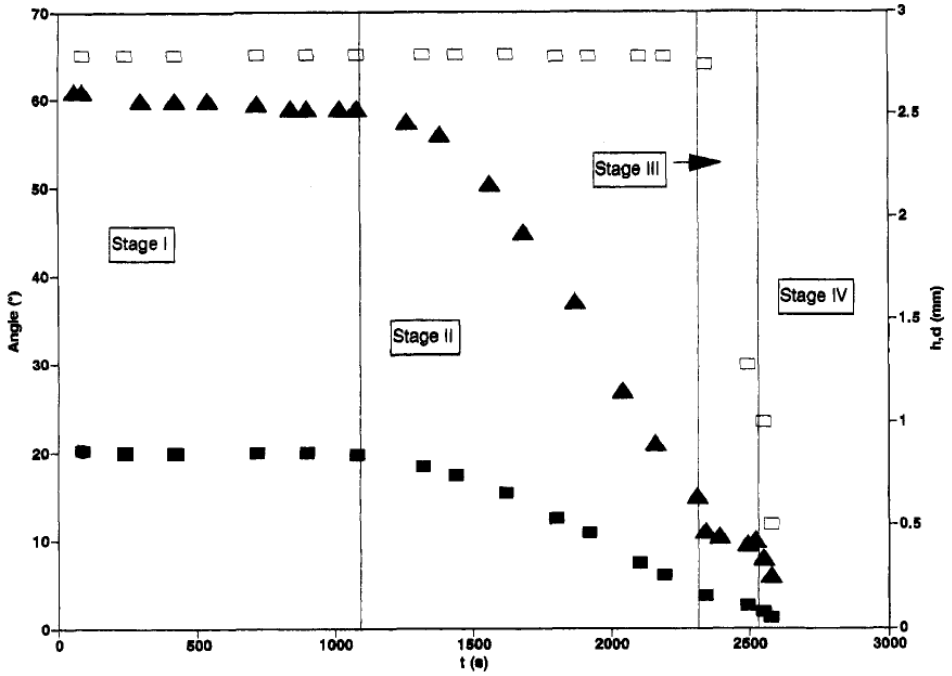

Figure 2.6: Evolution over time of (open square) diameter, *d*, (dark square) height, *h*, and (triangle) angle, θ, for a pure water droplet. Image taken from [7].

Surface roughness was found to be significant as the topographical defects of the surface anchored the TL and led to evaporation under mainly CCR, stage I, and disappearance of stage II or the CCA evaporation mode. Afterwards, Bourgès and Shanahan developed a model describing the evaporation process which compared well with the literature. At this point, we should note the different evaporation behaviour of a drop of n-decane drying on a Teflon surface. Essentially, during the third stage of the evaporation (stage III), which in this particular case was more prolonged, evaporation followed alternating cycles of CCR and CCA, before finally entering the

last stage of evaporation (stage IV). This new evaporative behaviour was termed "stick-slip".

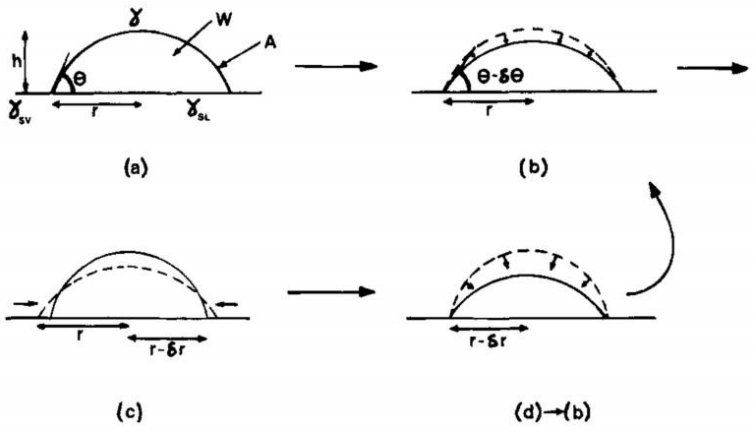

Figure 2.7: Schematic illustration of the "stick-slip" mechanism. Moving from the equilibrium stage (a) to the pinned stage (b) the evaporation evolves under the CCR regime, with the height, h, and the contact angle, θ,decreasing. Upon θ reaching a lower critical value, the TL jumps to a new, smaller position, $r - \delta r$, with h and hence θ increasing (c), (d) where it is pinned again and the evaporation proceeds as in (b) with the new initial radius of $r - \delta r$. Image obtained from [73].

Shanahan formulated a simple model describing the "stick-slip" motion of the TL of a drying drop [73]. Certain assumptions were made in order to simplify the problem: initial contact angle was smaller than 90º and the droplet was assumed to be a sessile droplet, which as described above is small enough for gravitational effects to be negligible, of an axisymmetric spherical cap shape, as seen in Figure 2.7 (a). As the environment around the droplet is not saturated with solvent vapour, evaporation occurs. However, the TL is pinned, perhaps as a result of a surface heterogeneity, which leads to a period of CCR evaporation (Figure 2.7 (b)), corresponding to a "stick" period. The pinned TL and the corresponding decrease in θ, indicate that the droplet

is not in thermodynamic equilibrium, therefore an excess free energy should build up due to contact angle hysteresis [67, 73]. Once the contact angle reaches a lower critical value, the excess free energy accumulated in the system should be sufficient for the system to overcome the anchoring of the TL. At this point, a sudden and instantaneous (when compared to droplet lifetime) "slip" event occurs and the TL retracts to a new and energetically more favourable position, potentially indicative of the hysteretic energy barrier pinning the TL, Figure 2.7(c). The droplet then continues drying, with alternating cycles of "stick-slip". A mathematical description of the excess free energy per unit length, $\delta\bar{G}$, accumulating in the system was also proposed, which accounted for volume change in terms of contact radius change, δR, in the following equation [73]:

$$\delta\bar{G} = \frac{\gamma sin^2\theta_0(2+cos\theta_0)(\delta R)^2}{2R} \quad (1.3)$$

, where θ_0 corresponds to initial contact angle of the "stick" cycle. The importance of this equation lies to the fact that it is an indirect way of quantifying the hysteretic energy barrier pinning the droplet; at the moment of TL "slipping" the excess free energy should be equivalent to the pinning barrier [73]. The simplifying assumptions made in order to produce this mathematical description were the following: axisymmetric and sessile drop was considered to be resting on a flat smooth surface (surface roughness considered much smaller than droplet radius) and the contact angle ranged from 0^o to 90^o. An attempt to refine this model by incorporating some of these effects was discussed in detail elsewhere [74].

More recently, a study on the TL motion kinetics of drying ethanol drops yielded some rather interesting results [75]. The pinning barrier was calculated with a slightly modified version of the theory proposed in [73]. In this new equation, $\delta\bar{G}$ is written as a function of $\delta\theta$ as this quantity decreases physically during either a "stick" event or CCR evaporation, thus making the shape/volume change easier to follow [75]:

$$\delta\bar{G} = \frac{\gamma R(\delta\theta)^2}{2(2+cos\theta_0)} \quad (1.4)$$

$\delta\bar{G}$ was found to be in the order of 10^{-7} N per unit length. This value lies somewhere between the experimental and predicted value of line tension and is of similar units [74, 76]. We can only speculate at this point that line tension effects and pinning barrier are related.

As the process of evaporation is fundamentally the exchange of molecules between the liquid surface and the environment, various parameters should affect it. For example, lowering the environmental pressure resulted in an increase in the diffusion of the evaporating molecules into the surrounding atmosphere and hence lead to increasing evaporation rate [14]. Increasing substrate temperature reduced the interfacial surface tensions and hence the Young's forces acting on the TL. Therefore, these weakened forces could not overcome the adhesion forces opposed on the TL due to surface roughness effect [15]. In a similar manner, surface roughness was found to increase the contact angle hysteresis which, in turn, promoted the TL pinning stage (CCR behaviour) of the evaporation process [77]. Artificial defects, *i.e.* pillars, were found to have the same effect; albeit for stick-slip or oscillating TL motion. The actual number of oscillations was found to be directly related to the size of the pillar and

attributed to the increasing pinning barrier the barriers impose on the TL [78]. On the other hand, the systematic study of the effect of substrate pores on droplet evaporation behaviour yielded two notable results. The degree of pore ordering and evaporation rate were found to be inversely proportional, as droplet spreading increased and hence the actual contact angle decreased which resulted in increasing evaporation rates [79]. Lastly, substrate hydrophobicity was found to be directly related to droplet lifetime due to the fact that contact angle and evaporation rate are inversely proportional [36, 80].

2.4. Colloidal droplets evaporation – coffee-stain effect

In their pioneering work, in 1997, Deegan *et al.* unveiled the underlying mechanism governing the everyday phenomenon of "coffee-stain" formation, by studying the evaporation of a suspension droplet containing microspheres. Essentially, the microspheres enhance CCR evaporation by increasing the pinning of the TL and result in the formation of a deposit at the periphery of the droplet or a "coffee-stain", presented in Figure 2.8 [19].

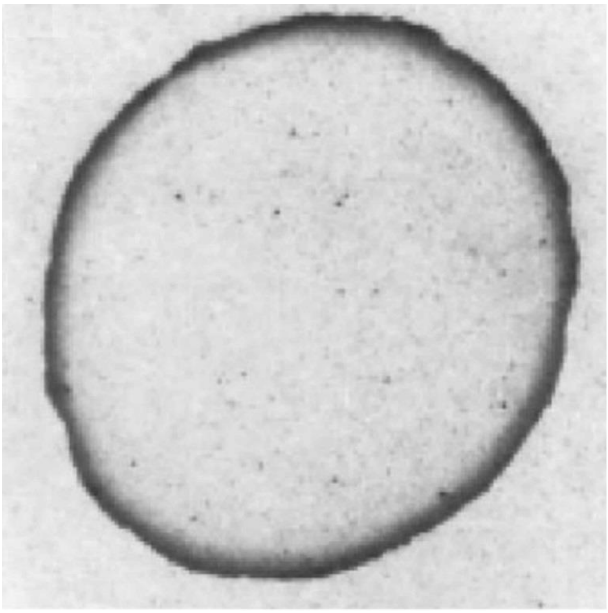

Figure 2.8: Coffee-stain deposit resulting from the evaporation of a microspheres drop evaporating under the CCR mode. Image obtained from [21].

In follow-up works, Deegan *et al.* complemented further experimental evidence with theoretical arguments which led to the first plausible description of the "coffee-stain" phenomenon [20, 21]. In more detail, the anchoring of the TL due to a surface defect, *i.e.* contact angle hysteresis, induces an outwards fluid flow from the bulk of the droplet in order to replenish the evaporated liquid at the periphery and keep the liquid front constant. Since particles are suspended in the droplet, the outwards flow carries and deposits the particles at the periphery (TL). Particle deposition promotes the pinning of the TL, as the liquid front now has to overcome both the surface defect and the particle deposit. As the deposit grows in size, the TL cannot de-pin, leading to the formation of a single ring-stain, Figure 2.8. Based on this mechanism, a series of different ring-stain patterns were produced [21]. Evaporation flux distribution on droplet surface was found to be irregular. In more detail, the evaporation rate, at the

periphery, was found to be much higher than at the rest of the droplet. To support this claim, three identical droplets were left to evaporate. The first droplet evaporated freely, the second was placed on a pedestal and was surrounded by water and the third was covered by a box with a hole directly above the top/middle of the drop. The first two cases left behind a ring-stain pattern (similar to the one seen in Figure 2.8). However, the third one, left behind a uniform disk-like pattern, as a result of suppressing evaporation at the drop's periphery due to the hole above the apex of the drop and hence the only possible path for the liquid vapour to escape. These findings are indicative of evaporation flux increasing greatly at the periphery due to a greater probability of an evaporating molecule to evaporate at the droplet edge than in the centre [20]. A theory was then developed, describing the evaporation process, in which evaporation rate was found to be proportional to the radius, R [20]. Results from this theory were found to be in agreement with those reported in [10] for pure liquids.

These findings peaked scientific interest over the past few years and numerous investigations soon followed. For example, further experimentations with droplet evaporation allowed the development of a numerical approximation of the process [12]. This approximation was then complemented with computer simulations, leading to the refinement of the theory proposed by Deegan *et al.* [20], incorporating the effect of a wide range of contact angles, $0° < \theta < 90°$ [12], which was further refined in a later contribution [81].

The more complex evaporation behaviour of "stick-slip" produced distinctive patterns, as the exemplary one shown in Figure 2.9. Adachi *et al.*, were amongst the first who reported the formation of a series of particulate stripes resulting from the drying of suspension drops. The number of stripes was found to be dependent on particulate concentration [82]. In a more recent contribution [83], the addition of nanoparticles in a droplet led to the formation of a series of concentric rings with a preferential, one-sided pinning, seen in Figure 2.9. This one-sided pinning of the droplet was reported to be rather random and was attributed to surface defects. This issue was not pursued further as the surface defects were measured with white light interferometry to be in the order of a few nano-meters, making them almost impossible to identify and experiment with. In the same contribution, the pinning barrier was quantified and found to be in the order of magnitude of 10^{-7} N per unit of TL length, using Equation 1.3. Elsewhere, the energy barrier value for the first jump of a "stick-slip" nanofluid system was calculated using both Equation 1.3 and 1.4 and was reported to be in the same order of magnitude for nanofluid concentrations up to 0.1 % wt. The comparison of the two showed some small discrepancies, but of similar order of magnitude, attributable to uncertainties in the experimental measurement of $\delta\theta$ and δR [36].

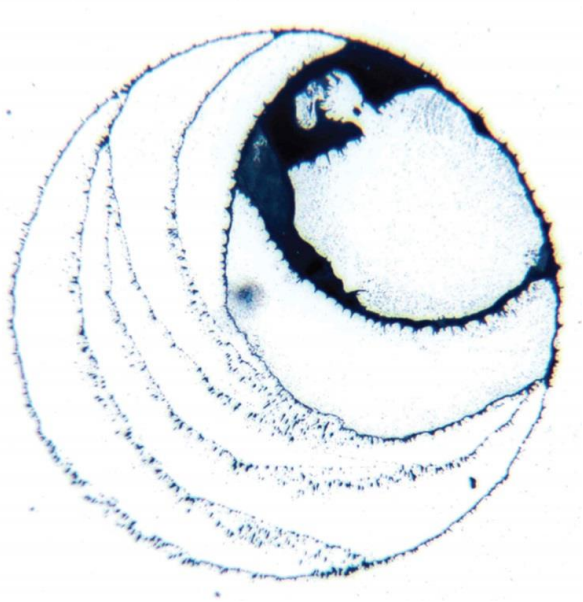

Figure 2.9: Characteristic pattern resulting from the evaporation of a nanosuspension droplet under the "stick-slip" mode. Image obtained from [83].

Various parameters affecting the evaporation process and especially the resulting ring-patterns were considered. For example, surface hydrophobicity, and hence contact angle since the two are directly linked, was reported to be inversely proportional to droplet lifetime [15, 84]. Elsewhere, increasing contact angle and hence hydrophobicity resulted in a transition in the evaporation behaviour from CCR to "stick-slip" [36, 85]. Controlling the evaporation rate was found to be of paramount importance to the evaporation process and the resulting pattern. Humidity, one of the parameters affecting evaporation rate, was reported to be inversely proportional to evaporation rate; a dictating factor of droplet spreading and hence resulting pattern [86, 87].

2.5. Particle self-assembly within ring-stains

For the purposes of this thesis, particles are divided mainly into two categories: hard and soft. Polymers and DNA molecules can be considered as soft/flexible objects, whereas rigid particles like colloidal spheres, carbon nanotubes (CNTs), etc. can be considered as hard ones.

2.5.1. Hard objects self-assembly

Particles within the ring-stain deposits typically form ordered crystalline structures. As the shape of spheres is the easiest to realise mathematically, they have been extensively used in droplet evaporation experiments with anchored, CCR [49], or intermittently moving, “stick-slip” [83], contact lines.

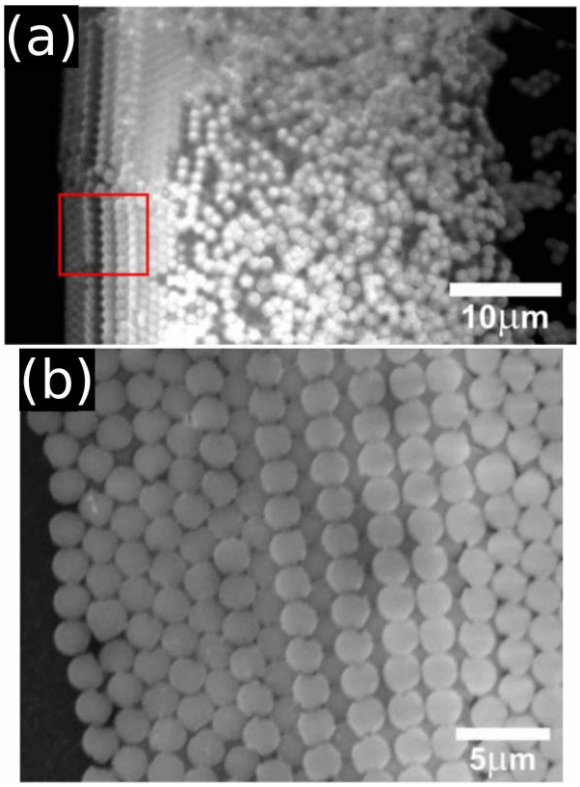

Figure 2.10: (a) Order to disorder transition in the self-assembly behaviour of spherical particles within a ring deposit. (b) Magnification of the area inside the box in (a). Droplet centre lies to the right in both images. Image adapted from [49].

The formation of particle terraces, which is indicative of ordering, was predicted for nanosuspension droplets, using lubrication theory and accounting for particles as structural disjoining pressure [35]. Experimental observations on linear liquid fronts, *i.e.* meniscus between a solid cylinder and the liquid or between a solid surface immersed in a pool of evaporating liquid, allowed the description of the deposition mechanism. Initially, the first particles arriving at the TL deposit themselves as close to the actual liquid front as their diameter and wedge area allow. With evaporation, more particles should arrive at the TL and self-assemble into the densest possible packing in the wedge constraints resulting in sequential hexagonal and square packed

regions. Eventually the deposit grows away from the wedge constraints and particles form mainly hexagonal structures [43, 47, 88-92]. These observations are important as they can explain the self-assembly behaviour of the particles in the region near the edge of the coffee-ring presented in Figure 2.10. Interestingly, an order to disorder transition can also be identified in the same figure further away from the periphery and toward the interior of the deposit (right side of Figure 2.10 (a)). This transition was attributed to the "rush hour" effect. Essentially, the flow, and hence particle velocity, increase over time. At a given critical time, t_c shown in Figure 2.11, the flow velocity increased rapidly, thus allowing little time for particles to self-assemble to their energetically favourable positions. Based on these experimental observations the authors then developed a hydrodynamic model describing the process [49].

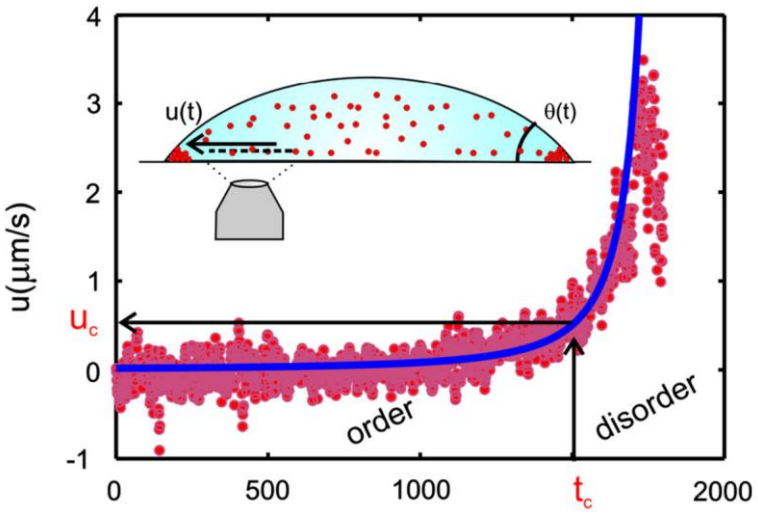

Figure 2.11: Origin of the order-to-disorder transition. Plot of measured (circle) and predicted (solid line) radial particle velocity versus time. Both model and experiment show the dramatic velocity increase at the end of the droplet's life (the rush hour). The inset shows the direction of the radial velocity in the droplet. The time t_c at which the order-to-disorder transition occurs is determined from experiments. Image adapted from [49].

Particle shape and size was found to be significant in the coffee-stain formation and in particle structuring. For example, polydisperse nanospheres led to irregular ring-stains [93]. Elongated particles, on the other hand, negated the coffee-stain mechanism and formed a uniform particulate layer [94-96]. In essence, ellipsoids tend to form loosely packed aggregates at the liquid-air interface which strongly attract the rest of the ellipsoids forming aggregates and distorting the interface. Thus, the coffee-stain phenomenon gets supressed. However, the addition of surfactant (SDS) restored the stain formation mechanism, by lowering the surface tension of the drop and hence making these interfacial distortion less energetically demanding and at the same time retarding the strong inter-particle interactions [94].

Particle shape dependent structures were also reported for evaporating nanofluids containing nanoparticles of various geometries [97]. Other irregular particles such as nanorods assembled into superlattices with clear particles arrays [98] and ribbon like structures [99]. Carbon nanotubes (CNTs), exhibited their own unique structuring behaviour within coffee-stains, presented in Figure 2.12 [100-104]. At a narrow area near the TL, CNTs align themselves parallel to the liquid front due to wedge constraints and the flow, in an attempt to achieve the densest possible packing. Moving toward the interior, the wedge constraints are felt weaker by the particles, thus allowing them to orient, to some degree, to the flow, leading to the formation of a transition region. In this region, particles exhibit a mixture of perpendicular and parallel to the TL assemblies. Further away from the periphery, where the wedge

constraints can no longer be felt, CNTs form assemblies mainly perpendicular to the TL as they align to the flow [100, 102].

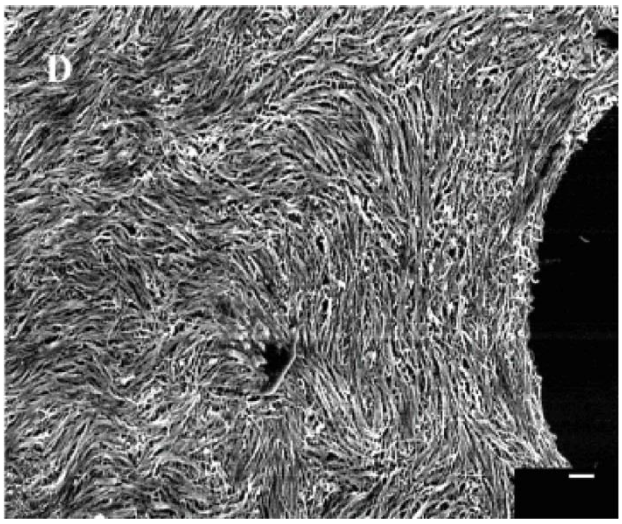

Figure 2.12: CNTs self-assembly behaviour at the edge of a dried droplet. Scale bar indicates 1 μm. Image taken from [100].

2.5.2. Soft object self-assembly

A series of molecules can be considered as soft objects. For example, polymers are rather flexible molecules with persistence length being the measure of their rigidity. Above this length polymers are considered flexible and below this length rigid and rod-like. Polymers can self-assemble into a variety of different structures. Poly-ethylene oxide (PEO) can form a series of crystalline structures. Due to diffusion-limited aggregation [105], PEO forms finger-like or dendrite structures [106]. Molecular weight and temperature were reported to lead to various other PEO nano-structures such as facets, dendrites and seaweed [107] or even labyrinths [108], presented in Figure 2.13. Elsewhere, isotactic polystyrene formed similar patterns [109, 110].

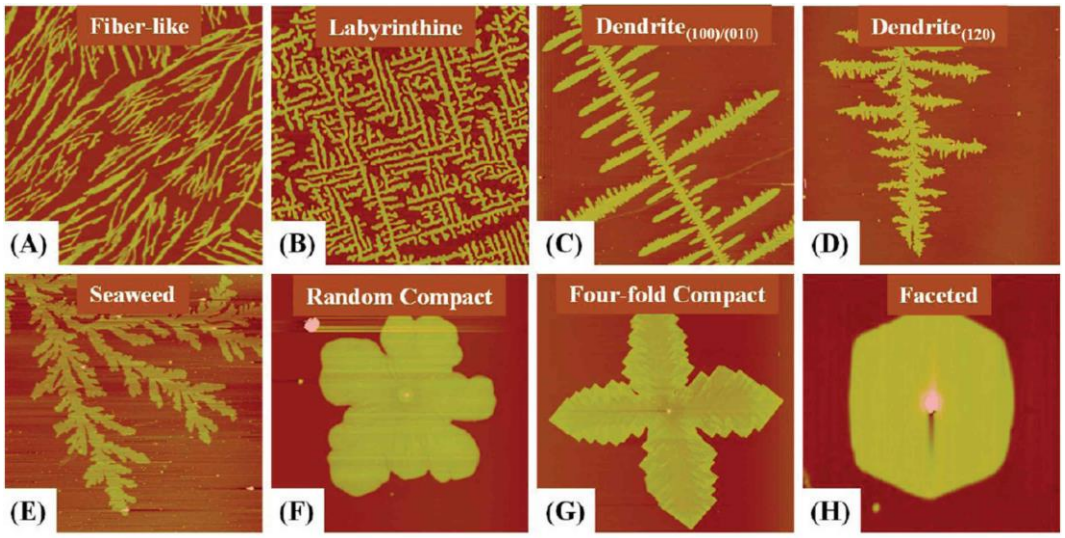

Figure 2.13: AFM topography images of various PEO nanostructures. Image obtained from [107].

Various bio-molecules with similar characteristics to polymers can also be considered as soft objects. DNA is a natural polymer, consisting of a number of monomer units, named base pairs (bp) of the four nucleotides Adenine, Thymine, Guanine, Cytosine [111]. It is a rod-like molecule with a diameter of approx. 2 nm and various lengths, depending on the number of bp and has a persistence length of approx. 50 nm [112-114]. The self-assembly of very short, in the order of 2 - 7 nm, and hence rigid DNA rods, led to the formation of nematic and columnar liquid crystals indicative of end-to-end stacked aggregates [114]. Increasing the concentration of these short DNA molecules led to the appearance of some dendritic structures [114]. On the other hand, very long and hence flexible DNA strands were reported to form zig-zag self-assembly patterns within coffee-rings [113]. Elsewhere, similar zig-zag patterns within concentric rings were produced by collagen which is similar in shape to DNA [115].

However, little information is known on the self-assembly process of DNA strands, with lengths between 20 bp and 1000 bp, at the TL of drying drops containing them.

Lastly, graphene is a novel, 2D, carbon honeycomb structure, and its shape can be described as an atomically thin platelet, giving graphene high flexibility. Novoselov and co-workers, were the first who successfully managed, in 2004, to mechanically exfoliate a graphene flake from graphite using scotch-tape. This new material was found to have astonishing electrical properties [116]. As its full potential is still unknown, graphene has attracted considerable attention for applications varying from biotechnology and medicine [117-121] to optoelectronics [116, 122-124]. The evaporation of droplets containing graphene platelets of different sizes, resulted in the formation of a coffee-stain for larger particles or a uniform disk for smaller ones. These two different behaviours were attributed to platelet surface activity. In essence, the larger the platelet, the highest the surface and hence particle charge density, resulting in higher hydrophilicity [125]. Patterns typical to "stick-slip" evaporation were also reported when drop drying was used as a means to separate the platelets [126], following the example of sorting spheres of various sizes in evaporating drops [127]. However, the evaporation dynamics and the self-assembly mechanism were not considered.

Chapter 3 Experimental methodology and techniques

3.1. Fluids and substrates preparation

3.1.1. Pure fluids

Deionised water and ethanol were used for the preparation of solutions for this study. Deionised water was obtained from a Barnstead NANOpure© Diamond^{TM} (Thermo Scientific, Waltam, MA) analytical ultrapure water dispensing system with a conductivity of 18.2×10^6 Ω/cm. Analytical grade ethanol was used as purchased from Sigma Aldrich (St. Luis, MI).

3.1.2. Nanofluids

Various nanofluids were used in this study. Spherical, non-porous SiO_2 nanospheres of *ca.* 80 nm diameter were acquired from Klebosol (AZ Electronic Materials France SAS, Trosly Breuil, France) in concentrated aqueous solutions and were diluted to 0.075, 0.1 and 0.125 % wt. concentration with the addition of deionised water. Pristine, monolayer graphene flakes were acquired from *graphene-supermarket.com* suspended in an ethanol solution with a concentration of 0.1 % wt. In all of the above solutions, no additives such as salts or surfactants were added. Prior to use, each solution was sonicated for about 30 minutes in order to fully disperse the solute. Two different in length plasmid DNA strands, No limits 100 base pairs (bp) and 1000, with length of 34 and 340 nm respectively, were acquired from Thermo Scientific (Waltam, MA) in powder form. Strands were diluted in pure deionised water and in a water solution containing 1mM Ethylenediaminetetraacetic acid (EDTA) to a final concentration of 0.01 % w/v. Prior to use, each solution was stirred with a vortex mixer until all of the solute was completely dissolved (identified by visual inspection).

3.1.3. Substrates

Table 3.1: Water and ethanol equilibrium contact angles, θ_0, and roughness, R_{rms}, of the two substrates used in this study.

Substrate	θ_0 with water	θ_0 with ethanol	Roughness, R_{rms} (nm)
Silicon	~55^o	<5^o	0.112
Teflon©	~115^o	~50^o	0.723

One of the main parameters of contact angle hysteresis is surface defects whether those may be chemical or topographical. For that reason, we used in this study smooth and flat substrates of two different degrees of hydrophobicity, one hydrophobic and one more hydrophilic. The more hydrophilic substrates were silicon wafers with a native oxide layer. The hydrophobic substrates were silicon wafers which were spin coated with a thin ~22 nm thin layer of Teflon©. Spin coating was conducted under nitrogen environment to limit contaminants and each wafer was afterwards annealed at 300^{o}C. Each wafer was cut into 1 × 1 cm^2 square tiles in order to be able to mount on the AFM. All wafers were prepared from our collaborators in the Scottish Microelectronics Centre. Prior to use, each tile was cleaned for a minimum of 10 minutes in an iso-propanol ultrasonic bath and then rinsed with deionised water and blow-dried using a jet of compressed air. The contaminants included in the compressed air supply had small impact on the cleanliness of the substrates, as only slight changes in contact angle were observed for more than 20 experiments in each case. Moreover,

AFM imaging did not reveal any contaminants, so it is safe to assume that the above mentioned cleaning process is sufficient. Typical AFM images of both substrates along with their corresponding height profiles are presented in Figure 3.1. Some striations can be readily identified in Figure 3.1 (b), which could be attributed to the small size of the features ($R_{rms} = 0.112nm$) being near the AFM resolution. However, these striations should have a negligible effect on particulate epitaxial deposition. Root mean square roughness, R_{rms}, and equilibrium contact angle, θ_0, for each substrate used, were determined by averaging data from more than 20 substrates measured using the AFM and DSA techniques, respectively, and are summarised in Table 3.1. R_{rms} was determined using a special function of the software Scanning Probe Image Processor (SPIP, Image Metrology, Hørsholm, Denmark).

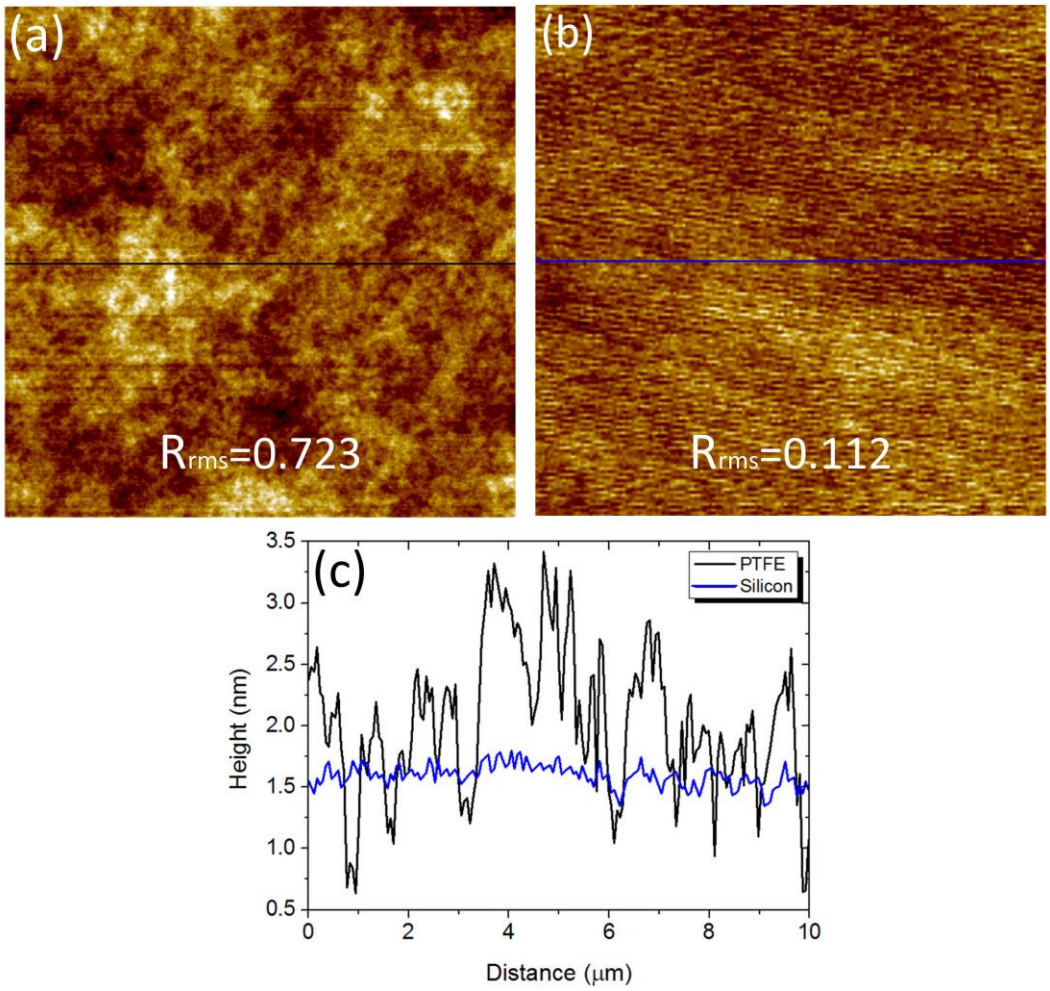

Figure 3.1: Typical 10 × 10 μm^2 topography image of (a) PTFE and (b) Silicon substrate and (c) their corresponding height profiles. Root mean square roughness (R_{rms}) is included in images.

3.2. Experimental techniques

The two main experimental techniques used in this study are Drop Shape Analysis and Atomic Force Microscopy. The first one was used in order to record and extract the evolution of the droplet profile over time and the second one in order to characterize the nano-structures within the resulting ring-stains. Other techniques such as pendant

drop and zeta potensiometry were also used, to a less extent, in order to establish various fluid parameters such surface tension and stability respectively.

3.2.1. Drop shape analysis

A Krüss DSA100 (Krüss GmbH, Hamburgh, Germany) drop shape analyser (DSA) was used to deposit droplets and record their evaporation evolution over time. The DSA was equipped with an automated, motorised dosage system that allowed precise control on the volume and deposition of droplets. The CCD camera of the DSA, in combination with a back light to provide better contrast, allowed the recording of the droplet profile during evaporation (in terms of volume, contact angle and contact radius). In addition, a custom-made low-pressure chamber (with a lower limit of 40 mbar) allowed experimentations under controlled environment (pressure, humidity). When the chamber was mounted on the DSA, windows on both sides of the chamber allowed the camera of the DSA to record the evolution of the drop profile over time. The DSA was connected to a PC and all controls, recording and analysis were conducted using the dedicated software DSA1 v1.9.

The deposition process is as follows: pre-cleaned substrates were placed directly below the electronically control dosage system of the DSA. Using this system, a 3 μL droplet was produced at the needle tip and then carefully lowered to the substrate until gentle touch, at which point the needle was removed. A sequence of frames was then captured varying in number according to the speed of evaporation. Typically, approximately

400 frames were recorded for droplets evaporating at ambient conditions and approximately 100 frames for droplets evaporating rapidly under 100 mbar pressure. Frame rate per second was adjusted in accordance with evaporation speed in each case. Ambient conditions should be considered 1000 mbar pressure, *ca.* 30 % relative humidity and 22^{o} C. Subsequently, the frame sequences were analysed using the DSA1 v1.9 software. Analysis allowed the determination of the droplet profile in terms of contact angle, θ, contact radius, R, and volume over time, t. Droplet profile determination was achieved by the circle fitting method as the substrates used in this study are rather hydrophobic, $\theta > 50^{o}$.

3.2.2. Pendant drop technique

The pendant drop technique is a way of determining the gas-liquid, γ_{GL}, surface tension of a fluid. During this process, a liquid droplet is formed at the tip of a syringe and its size is slowly increased until dropping off the syringe. In principle, this interplay between the interfacial forces keeping the droplet attached on a syringe and gravitational forces pulling it down allow the determination of γ_{GL}. The apparatus used for these measurements was a First Ten Angstroms FTA100 (Portsmouth, VA). An average value of 20 measurements was taken for each solution in question at approx. 15^{o} C. The results are presented in Table 3.2. As all the DNA suspensions showed similar γ_{GL}, we present here a characteristic one.

Table 3.2: Average gas-liquid surface tension and ζ-potential of silica-water and graphene-ethanol nanofluids.

nanofluid	average γ_{GL} (mN/m)	average ζ-potential (mV)
SiO_2 in water	73.11±0.6	-30.63 ± 1.64
Graphene in ethanol	22.34±0.8	-21.88 ± 1.72
DNA suspension	74.82±0.54	-

3.2.3. ζ-potentiometry

In order to further understand the evaporation kinetics and particle deposition patterns in freely evaporating nanofluid droplets, we measured their ζ-potential. ζ-potential is indicative of the stability of a colloidal suspension. In principle, it is a quantification of the interaction of charged particles when an external field is applied. These measurements were carried out using a ZetaPALS or Zeta Potential Analyser from Brookhaven Instrument Corporation (BIC, Holtsville, NY) and its accompanying software ZetaPALS.

The experimental procedure was as follows: approximately 1.5 mL of each nanofluid was placed in a cuvette, filling it almost full. Then the special lead with the attached electrodes was placed on top of the cuvette while carefully immersing the electrodes within the liquid. Subsequently, an electric field was applied which resulted in

oscillations of the charged particles. The motion of the particles was followed by the Phase Analysis Light Scattering (PALS). Once each measurement was completed, the dedicated ZetaPALS software calculated the ζ-potential. For each solution a minimum of 20 measurements were acquired and the average values were calculated. Results are presented in Table 3.2. Given the small volume of the DNA suspensions ~100 μL, ζ-potential measurements could not be carried out. Measurements were taken in collaboration with Ioannis Stamou from the School of Engineering, University of Edinburgh.

3.2.4. Atomic force microscopy

Atomic force microscopy (AFM) was the method of choice to characterize the surface homogeneity, whether that may be topographical or compositional, of each substrate used in this study. In addition, this same imaging technique was used as a means to visualise the fine particle structures forming at the TL upon full evaporation of the nanofluids. AFM was selected as it provides unprecedented sub-nanometre resolution both vertically and laterally without requiring any special sample pre-treatment. AFM can also simultaneously acquire topographical and adhesive properties of a sample and at the same resolution, hence giving an extra advantage over other techniques and allowing identification of different species on a sample surface or even grain orientation.

The AFM used in this study was a Bruker Multimode/ Nanoscope IIIa AFM (Bruker AXS, Santa Barbara, CA). In order to achieve the best possible resolution, two

different scanners were used. To quickly identify sample features in larger areas we used a J-scanner, which allows a maximum x-y scan range of *ca.* 140 microns. For smaller areas and better resolution, an E-scanner was used with a x-y scan range of *ca.* 10 microns. A series of different cantilevers were used with varying properties and were all supplied by Bruker. In more detail we used RTESP and RTESPA cantilevers with nominal spring constant of 40 N/m, resonance frequency 300 kHz and tip curvature of *ca.* 8 nm, as specified by the manufacturer. The difference between these two is an extra thin Al layer coating the back side of the second cantilever (RTESPA) allowing better tracking of the deflected laser beam and hence better resolution. To image the fine-structuring of the deposits we used the sharper TESP-SS Bruker cantilevers with nominal spring constant of 20 N/m, resonance frequency 230 kHz and tip curvature of *ca.* 2 nm, as specified by the manufacturer. The microscope was operated under tapping mode (tip at intermittent contact with the surface) and all measurements were conducted in air at room temperature. In the same mode of operation a second signal, that of phase, is also recorded for each image. Phase imaging is a complementary to topography and measures the shift in phase of tip oscillation. This shift originates in different tip-sample interactions due to topometric (slope) but mainly compositional variations of the sample. Acquired images were post-processed and analysed using the software Scanning Probe Image Processor (SPIP, Image Metrology, Hørsholm, Denmark).

3.2.5. Scanning electron microscopy

Scanning electron microscopy (SEM) complemented AFM measurements of graphene platelets self-assembly behaviour. Prior to measurement, samples were coated with a thin, conductive gold layer. Two different, in maximum resolution, SEM were used: a Philips XL30CP (Philips, Amsterdam, Netherlands) and a Hitachi 4700 II field-emission (Hitatchi, Tokyo, Japan). Experiments were conducted in collaboration with Dr. Nicola Cayzer and Mr. Steve Mitchell from the schools of Geoscience and Biology, respectively, in the University of Edinburgh.

Chapter 4 Particle crystallization at the three-phase contact line

In this chapter we attempt to shed light on the mechanism responsible for the deposition of particles at the TL of evaporating nanosuspension droplets in order to form crystalline ring-stain patterns. An aqueous suspension containing monodisperse nanospheres exhibited "stick – slip" evaporation and left behind a set of concentric rings with a preferential pinning to one side. Nanoscale investigation of the resulting rings yielded rather unexpected structuring results: a closely-packed crystalline structure with disordered regions at both sides. In order to understand the underlying mechanism leading to the formation of the disordered region at the exterior side of the ring, we investigated experimentally the significance of particle velocity on the particle structuring mechanism. To achieve this, environmental pressure was lowered leading to higher evaporation rates, which in combination with the pinned TL and the induced outward flow, led to faster particle velocities. As a result, increasing particle velocity was found to promote crystallinity. Consequently, particle velocity was quantified which coupled with the deposit shape measurements, allowed the proposition of a first, plausible description of the particle self-assembly behaviour at the TL of evaporating droplets. In more detail, particle self-assembly behaviour is controlled by an interplay between the fluid, and hence particle, flow velocity (main ordering parameter) and wedge constraints, and consequently disjoining pressure (main disordering parameter). The second observed disordered region at the interior side of the ring, was attributed to the rapid TL motion during each "slip" event. Moreover, the hysteretic energy barrier was calculated, providing insight on TL motion kinetics.

4.1. Evaporative behaviour and resulting ring-stains

In order to probe the self-assembly behaviour of nanospheres at the TL of freely evaporating droplets, we first conducted a series of free evaporation experiments with increasing particle concentrations. In more detail, a series of droplets of aqueous suspensions containing 0.075, 0.100 and 0.125% wt. monodisperse SiO_2 nanospheres were deposited on flat, smooth silicon substrates. Their free evaporation was recorded using a Krüss DSA100 (drop shape analysis, section 3.2) and analysed with the accompanying software. A typical example of the pattern left behind after the free evaporation of the above solutions and the corresponding evolution over time of both the contact radius and angle of each case are presented in Figure 4.1. More than 20 repetition of each experiment showed very good reproducibility.

The TL of the droplet containing 0.075 % wt. spheres exhibit an initial pinning period until approx. 300 sec., at which point it de-pins from one side and continues evaporation with a retracting TL (Figure 4.1(b)). In the resulting pattern presented in Figure 4.1(a), some pyramidal-like structures can be seen at the point where the initial TL lied. These structures were formed due to, perhaps, an initial weak pinning event inducing a liquid flow carrying some particles there. As particle concentration is low locally, pinning cannot be sustained for long, and the TL starts retracting, “freezing” particles in place and thus forming the pyramidal structures. Increasing particle concentration to 0.1 % wt. should increase the pinning of the droplet. Indeed, the

pinning of the TL appears to have been promoted and two "slip" events can be clearly identified in the evaporation evolution (Figure 4.1(d)). This promotion of pinning can also be identified in the resulting pattern (Figure 4.1(c)), where the afore-mentioned pyramidal structures appear to have been distributed more uniformly along the initial TL. Some periodicity of these structures could also be identified, possibly indicating an oscillating behaviour of the liquid front at the small surface defects (as presented in Chapter 3.1.3) and very small scales, beyond the capabilities of the CCD camera of our experimental setup. Nonetheless, a correlation with the oscillating behaviour for artificial defects could be drawn [78].

At 0.125 % wt. nanospheres concentration , a typical "stick-slip" evaporation behaviour and resulting pattern can be observed in Figure 4.1(d, f). In more detail, the TL remains anchored for a longer period (*ca.* 800 sec.) during which pinned TL and simultaneous evaporation leads to particle deposition (stick phase). This period is followed by the rapid TL motion (slip) to a subsequent state of quasi-equilibrium. At the same time, each "stick" period results in the formation of one of the well-defined rings seen in Figure 4.1(e). However, in the evolution graph (Figure 4.1 (f)) only two "jumps" of the TL are clearly identifiable mainly due to the orientation of the camera while recording the movement of the TL.

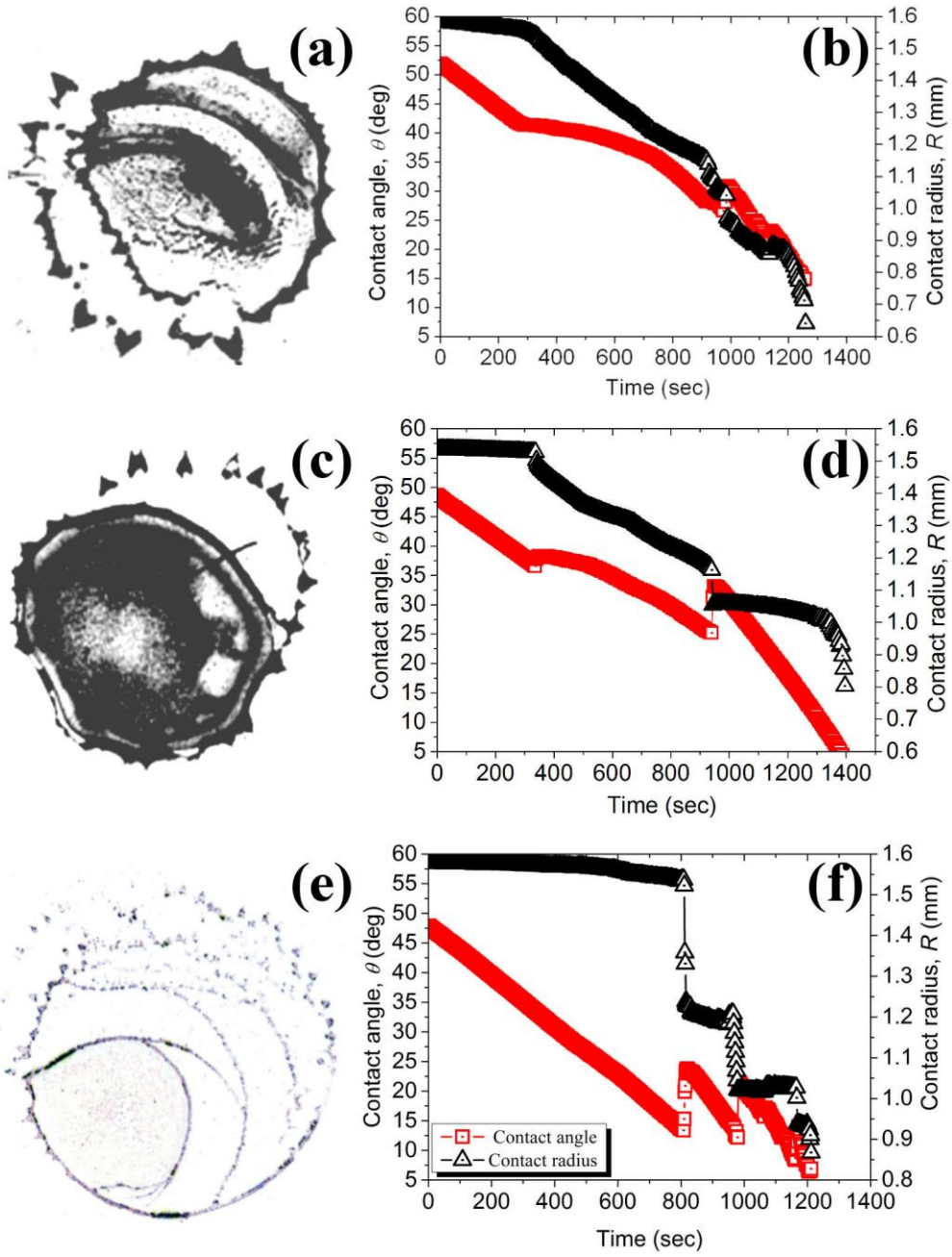

Figure 4.1: (a, c, e) Optical micrographs of the coffee-stains left behind after the evaporation of a freely evaporating aqueous suspension drops containing (a) 0.075, (c) 0.1 and (e) 0.125% wt. SiO_2 nanoparticles respectively. (b, d, f) Evolution over time of contact angle (squares) and contact radius (triangles) for same drops.

4.2. Triple line motion kinetics

Having established the optimal particle concentration for the ring-stain formation, let us, here, briefly address the TL motion kinetics of each case examined by quantifying the hysteretic energy barrier pinning the TL [73, 75]. To that end, we should first calculate the evolution of the excess free energy, δG, of the drop during evaporation, over the equilibrium value, $G(\theta_0)$, assuming that the contact radius, R, remains constant. Neglecting gravity effects since the drop is small, at a given instant, when contact angle is θ and free energy is $G(\theta)$, we have [73, 75]:

$$\delta G = G(\theta) - G(\theta_0) = \gamma\pi\left\{R^2\left[\frac{2}{(1+\cos\theta)} - \cos\theta_0\right] - R_0^2\left[\frac{2}{(1+\cos\theta_0)} - \cos\theta_0\right]\right\} \quad (4.1)$$

The term R_0 corresponds to the radius of a drop of equal volume to the actual drop, but at equilibrium ($R \geq R_0$). Clearly, R_0 decreases as evaporation continues, although θ_0 does not, since volume, V, decreases. At a given instant, for given V, we have:

$$V = \frac{\pi R^3}{3\sin^3\theta}(1-\cos\theta)^2(2+\cos\theta) = \frac{\pi R_0^3}{3\sin^3\theta_0}(1-\cos\theta_0)^2(2+\cos\theta_0) \quad (4.2)$$

Isolating R_0^2 in Equation (4.2) and inserting it in Equation (4.1) we obtain:

$$\delta G = \frac{\gamma\pi R^2}{(1+\cos\theta)}[2-\cos\theta_0(1+\cos\theta) -$$

$$-(1-\cos\theta)^{1/3}(2+\cos\theta)^{2/3}(2+\cos\theta_0)^{1/3}(1-\cos\theta_0)^{2/3}] \quad (4.3)$$

We can thus calculate the excess free energy, per unit length of TL, $\delta\bar{G}$, at any instant during evaporation from δG. With knowledge of R during a given phase of

evaporation, the value of θ at the moment in question, and the equilibrium angle, θ_0, the evolution of $\delta\bar{G}$ can be followed. When a jump of R to a smaller value occurs, it may be considered that $\delta\bar{G}$ has attained the value of the hysteresis jump barrier. Liquid surface tension, γ, was measured using the pendant drop technique to be that of pure water, *ca.* 0.073 N/m, as described in Table 3.2. The evolution of $\delta\bar{G}$ over time solution is presented in Figure 4.2.

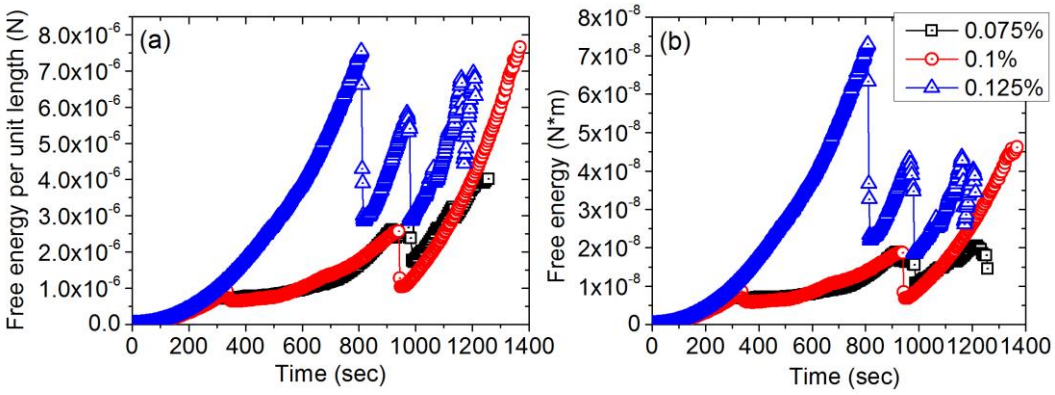

Figure 4.2: Evolution of $\delta\bar{G}$ (left) and δG (right) over time for freely evaporating aqueous suspension drops containing (squares) 0.075, (circles) 0.100 and (triangles) 0.125% wt. SiO_2 nanoparticles.

As it can be seen in Figure 4.2 (a), $\delta\bar{G}$ increases rapidly, initially, due to the pinned TL and decreasing contact angle for the cases of 0.075 and 0.1% wt. particle concentration (squares and circles in Figure 4.2). During this stage, particles arrive at the TL increasing the viscosity locally and hence strengthening the pinning [83]. However, the pinning due to particles is not strong enough and the TL starts receding

at approx. 300 sec. Due to the increased local viscosity the TL retraction is not fast enough which combined with the fact that one side of the droplet remains pinned throughout the evaporation, leads to a slower $\delta\bar{G}$ increase, until ~950 sec. It is during this phase that the pyramidal structures identified in Figure 4.1 (a, c) formed. At that point, ~950 sec, in both cases $\delta\bar{G}$ reaches the apparent threshold value of *ca.* 2.6×10^{-6} N, which should be equivalent to the hysteretic energy barrier, $\delta\bar{G} = U$, and a "slip" event (which is more obvious in the 0.1% case, Figure 4.1) occurs with a consequent consumption of $\delta\bar{G}$. After this point, $\delta\bar{G}$ continues to increase until full evaporation. This pinning barrier value is in line with the literature [36]. Figure 4.2 (b) depicts the evolution over time of the free energy of the droplet, δG, for comparison. δG can be readily identified to exhibit a slightly different behaviour than $\delta\bar{G}$, especially near the end of the 0.075% lifetime where it decreases. This observation allows us to determine that dividing the accumulating energy by droplet circumference, $\delta\bar{G} = \delta G/2\pi R$, demotes the importance of R in the equation. This observation, however, could be correlated with the physical concept of TL motion. Locally, at the TL the change in R is much smaller compared to the change in θ (especially when considering how more pronounced and sensitive the changes in angle appear to be compared to those in R curves in Figure 4.1).

Focusing our attention to the 0.125% case, we can identify the following trend: an initial $\delta\bar{G}$ increase, due to the pinned TL and the decreasing contact angle. Throughout the duration of this mode ("stick"), the particles accumulate at the TL and form the

ring-stain. At approx. 800 sec., $\delta\bar{G}$ reaches a maximum value of *ca.* 7.5×10^{-6} N, which is agreement with what has been reported previously [36] and roughly double the value calculated in this study for the lower concentration cases (0.075 and 0.1 %). At this point the TL jumps to a new smaller R with higher θ (as seen in Figure 4.1), leading to suspension of particle accumulation. Essentially, at this point the system "freezes", allowing no time for particles to self-assemble and hence leads to disordering. We should note here the fact that the first jump appears to demand a higher amount of energy compared to the rest. This could be attributed to the fact that the first jump corresponds to the case where the substrate outside the drop has not "seen" the liquid. For each subsequent "slip" event, the substrate has already been wetted by the nanofluid and hence it is plausible that an adsorbed liquid layers remains, resulting in the observed decrease of the energy barrier value. This cycle continues until full evaporation.

4.3. Particulate deposition and crystallisation

In order to assess the particle structuring at the TL of evaporating droplets, we utilised optical microscopy and AFM for macro- and nano-scale measurements. In this part, we focused our attention on the 0.125% case as it is the only one that produced well-defined ring-stain deposits. A typical optical microscopy image of a part of the ring-stain is presented in Figure 4.3 (a). In this image, a striped region can be readily identified, which is an optical interference pattern at the side toward the exterior of the droplet (left side of the image). This pattern is indicative of gradual deposit height

increase. Cracks can also be seen, which could be attributed to the uncontrolled character of the evaporation process. However, they are beyond the scope of this work and will be assessed in the future.

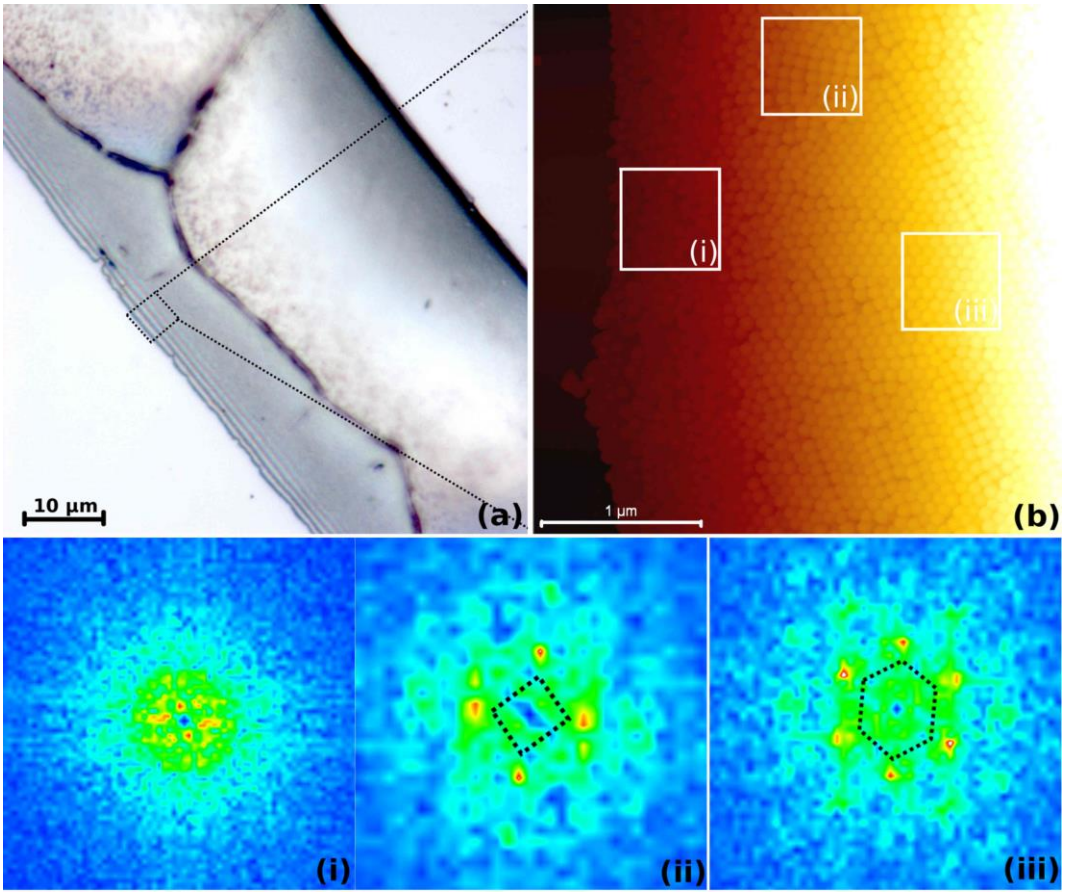

Figure 4.3(a) Optical micrograph depicting part of the ring stain. (b) 3.32 × 3.32 µm^2 topography image (dotted box in (a)) with three different areas of interest highlighted, *z*-scale ranges between 0 – 1.25 µm. In both images drop centre lies to the right. (i-iii) FFT analysis of the areas highlighted in the topography image (b), dotted lines are a guide to particle packing.

The self-assembly behaviour of the nanospheres at the edge of the ring-stain was extensively investigated with AFM. A typical topography image of the edge of the ring-stain is presented in Figure 4.3 (b). Analysis of the coffee-rings revealed a narrow disordered region forming at the very edge of the ring-stains (side toward the TL) and

seen in white box (i) in Figure 4.3 (a). Furthermore, sequential square and hexagonal packed structures formed toward the interior of the coffee-ring (boxed areas (ii) and (iii) in Figure 4.3 (b)). The Fast Fourier Transformation (FFT) of each of these areas is presented in Figure 4.3 FFT (i)-(iii), respectively, as a means of determining particle structuring. In more detail, the formation of the disordered region at the very edge of the droplet, which appears as the smeared FFT (i), could be attributed to a combination of a) small particle size, which allowed particles to reach very close to the actual triple-interface wedge area, where disjoining pressures are to stronger, b) higher evaporation at the drop periphery and c) strong laminar solute flux towards the TL, the last two being directly linked. The exact particle structuring mechanism at the TL is thoroughly discussed in section 4.4. As particles continue to arrive due to the outward flow from bulk to periphery [19], particles further away from the periphery should have more space and freedom to move due to weaker geometrical constrains/ disjoining pressure effects. Due to this fact, particles assemble into square and hexagonal packed regions, shown in Figure 4.3 (ii) and (iii) respectively.

The rest of the deposit was also probed with AFM. In order to unveil both the deposit height and the crystal structure, we present sequential $5 \times 5\ \mu m^2$ images scanned across the width of the ring in Figure 4.4. The height of each image was zeroed on the top of the previous one for better visualisation.

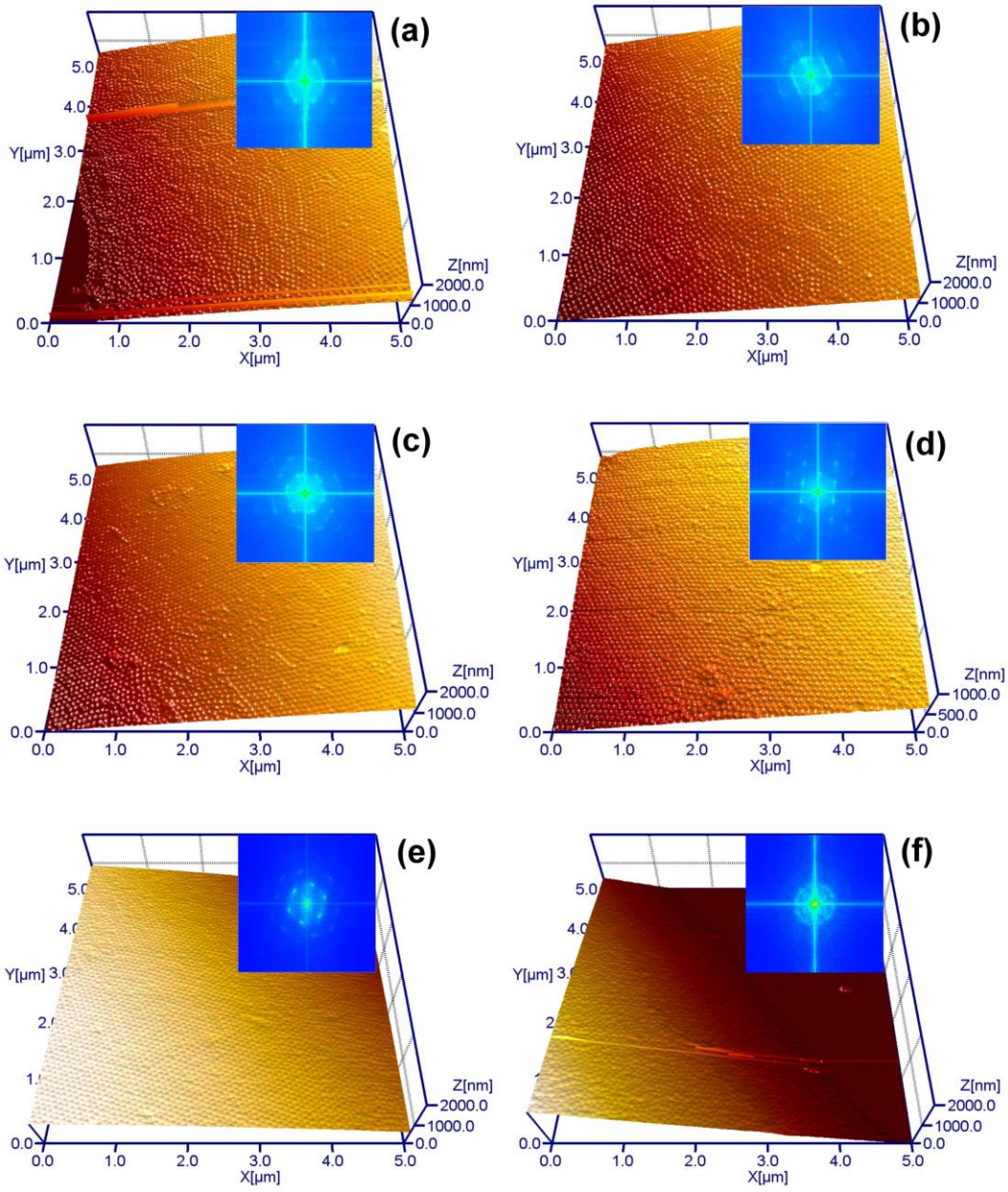

Figure 4.4: (a)-(f) Sequential 3-D representations of areas of the ring-stain scanned across its width. Corresponding FFT analyses are presented as insets in each image. Droplet centre lies to the right of each image.

An order to disorder transition can be readily identified at both the interior and the exterior edge of the deposits, Figure 4.4 (a) and (f) respectively. As discussed above,

at the exterior edge of the deposit, Figure 4.4 (a), the particles first randomly arranged themselves at a narrow area near the edge which was followed by close-packed structures. Particles, at the rest of the ring-stain, formed sequential square and hexagonal packed regions, Figure 4.4 (b)-(e). In more detail, with increasing deposit height (which should be indicative of the actual liquid/droplet height) and hence weakening wedge constraints, particle ordering was promoted to mainly hexagonal structures with some interstitial square packed regions. Similar sequential square and hexagonal packing was reported in a number of other cases with experimental setups different from ours (*i.e.* controlled evaporation, larger sized particles, different geometry) and was attributed to the same reasons [42-46]. The FFT insets further support the fact that the hexagonal cell gradually becomes clearer. At the apex of the deposit, Figure 4.4 (d), an almost perfect hexagonal packing was found, possibly due to the extra volume and hence more space for particle free motion and eventual deposition at the most favourable positions. Indeed hexagonal packing leads to a higher particle density, which is entropically more favourable [42]. To the best of our knowledge, this is the first time that particle terraces, although short, are reported for particles of this size (~80 nm).

Away from the deposit apex and toward its interior, Figure 4.4 (e), deposit height decreases sharply. This sharp decrease should make the wedge constraints more effective, which resulted in the formation of some square-packed regions (FFT blurred). Additionally, we should note the steepness of the slope at this side of the ring, due to the rapid “slip” of the TL. At the other edge of the deposit, interior Figure 4.4

(f), a second order to disorder transition was observed. Elsewhere, this transition was attributed to increasing particle velocity over time, termed "rush hour" effect [49]. We should note, here, that the droplet in Ref. [49] evaporates with a constantly pinned TL, leading to the deposition of particles at the same annular region. In our case, however, the droplet follows the "stick-slip" evaporation regime, which, as described in section 2.4, leads to an abrupt cut-off in the outwards fluid flow during each "slip" event. This abrupt cut-off essentially "freezes" particles and results in the observed disordering at the interior. A schematic representation of the self-assembly pattern at each part of the ring is presented in Figure 4.5.

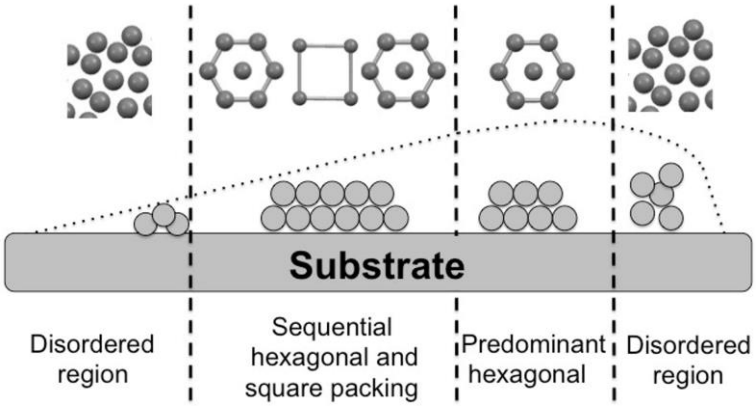

Figure 4.5: Schematic illustration of particle structuring across the width of the ring-stain.

4.4. Particle deposition and self-assembly mechanism

Let us, here, address the underlying particle structuring mechanism at the confinement of evaporating three-phase lines. Our results clearly show the formation of a narrow disorder region appearing at the exterior side of the deposit. Elsewhere, however,

particles were reported to have arranged themselves in hexagonal order, at the same exterior edge of a ring-stain deposit and form a disorganised region toward the interior [49]. There are mainly two differences between the two systems which should affect the structuring process: the evaporation behaviour and the particle size.

In our case, particle diameter, d, is *ca.* 10 times smaller than the one reported previously , D, ($d \sim 80$ nm compared to $D \sim 0.5 - 2$ μm). Considering the actual particle size, the particles in our case can get closer to the actual liquid front (Figure 4.6). Therefore, the wedge constraints and hence the disjoining pressure effects felt by the nano-spheres are much stronger compared to those affecting the micro- spheres. Due to height restrictions, particles are necessarily smaller than the droplet height, h_w, at the very edge of the contact line. The approach distance, l, is simply given by $l = d \cot\theta$(or $L = D \cot\theta$ for the microspheres in Ref. [49]). For small contact angle, θ, this difference in distance from the TL to the first particle will be considerable for the two cases and can be calculated as follows:

$$(L - l) = (D - d)\cot\theta \approx D \cot\theta \qquad (4.4).$$

From the above simple argument, we estimate for a contact angle of *ca.* 50^o that micrometric particles [49] may approach the TL only to within *ca.* 0.4 μm or more (varying with particle diameter). However, in our case nanoparticles may get within *ca.* 65 nm, the domain where stronger evaporative effects may be felt, leading to faster and less ordered particle precipitation. The above argument is schematically presented in Figure 4.6.

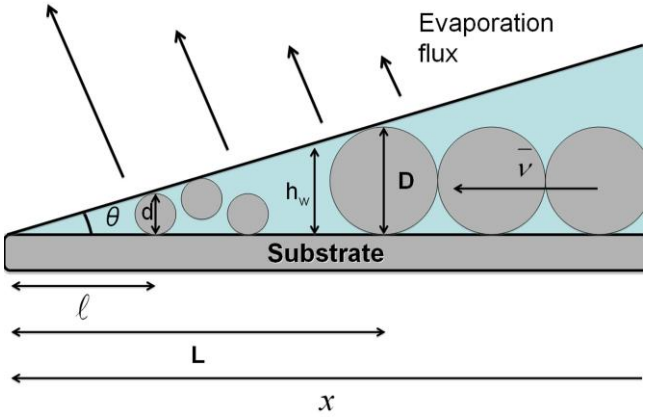

Figure 4.6: Schematic illustration of the distance from the TL where the first particle will be deposited for micro- (*D, L*) and nano- spheres (*d,l*).

From the above it is clear that the narrow disordered region at the exterior edge of the deposit formed due to the interplay between particle velocity and wedge constraints/ disjoining pressure. In what follows, we attempt to assess this possibility by combining theoretical and experimental arguments. To that end, we reduced the environmental pressure around the droplet to 750 and 500 mbar in order to increase the radial fluid velocity. Evaporation flux is known to be higher at the periphery of a pinned droplet [12, 19, 20]. The average evaporation rate increased from *ca.* 2.5 nL/sec to 3.8 and 7.5 nL/sec respectively for 1000, 750 and 500 mbar. Furthermore, increasing the evaporation rate should result in promotion of the pinning of the TL as more particulate is carried to the periphery with the enhance radial flow, thus increasing locally particle concentration and hence viscosity. Evaporation flux is dependent on vapour diffusivity, which in turn is connected with pressure via the formula: $D_{ua} \approx D_{ref}P_{ref}/P$, where $D_{ref} = 2.4 \times 10^{-5}$ m^2/sec is the value of D_{ua} at the reference

pressure $P_{ref} = 1000$ mbar [14]. This simple formula was introduced into the height-averaged radial velocity, $\bar{v}$, an equation proposed in Ref. [49, 128], leading to:

$$\bar{v}(r,t,P) = \frac{4\Delta c R(t)}{\pi\rho\theta(t)}\left[\frac{1}{\sqrt{R^2(t)-r^2}} - \frac{R^2(t)-r^2}{R^3(t)}\right]\frac{D_{ref}P_{ref}}{P} \quad (4.5),$$

where θ and R are contact angle and contact radius and, r is radial distance. Vapor concentration difference between drop surface and the surroundings, $\Delta c = 1.9 \times 10^{-2}$ kg/m^3 and liquid density, $\rho = 1000$ kg/m^3. This equation is based on a Newtonian fluid, however, in the present work the fluid could be considered non-Netwoning very near the edge (TL). At this point, particle accumulation should make the fluid too viscous, making this equation to fail. Nonetheless, this equation provides an approximation of fluid and hence particle velocity, which is useful in order to understand the underlying physics governing the self-assembly mechanism of particles at the TL.

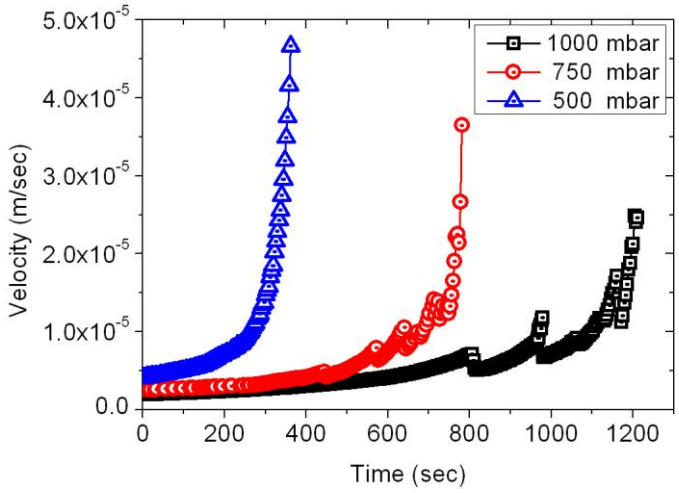

Figure 4.7: Particle velocity evolution over time at the deposit edge ($r = 0.99$) for evaporation under 1000, 750 and 500 mbar pressure.

As we are interested for the wedge area at the actual edge of the droplet, Equation (3.5) was solved for $r = 0.99$ for each of the pressures. The evolution of $\bar{v}$ over time for each case is depicted in Figure 4.7. Under ambient conditions (1000 mbar) $\bar{v}$ was found to reach a maximum value of *ca.* 2.5×10^{-5} m/sec. Reducing the pressure led to max. $\bar{v}$ values of 3.6×10^{-5} m/sec and 4.7×10^{-5} m/sec for 750 and 500 mbar, respectively. Some small discrepancies in the 1000 and 750 mbar curves should be attributed to "stick-slip" evaporation and the dependency of Eq. (3) on θ and R. These results are in agreement with the velocity calculated in the case of a constantly pinned drop [49] but have not been reported before for stick-slip evaporation.

Subsequently, AFM was used to determine the effect of this increasing velocity on particle structuring at the exterior edges of the ring-stains. We found that increasing the particle velocity promotes crystallinity at the very edge of ring-stain deposits. We present the topography image of each case in Figure 4.8 with lowering pressure from 1000 - 500 mbar in Figure 4.8 (a) - (c) respectively. As the particles are not easily discernible in these images, we also included a magnification of a random area of interest near the deposit edge as an inset at the bottom of each image (similar to Figure 4.3(i)). The corresponding FFT analysis of each case is also included in the top insets. It is readily apparent, in these images that the slope/size of the deposit decreases with increasing evaporation rate, which in turn increases the wedge constraints. To quantify this observation, we present a comparison in Figure 4.8 (d) of the average coloured height profiles corresponding to the typical coloured line scans in Figure 4.8 (a), (b) and (c). To further highlight the available space for particle motion and deposition at

the edge of the deposit, we provide a magnification of the first 0.5 microns of each of the three height profiles and shows the first pinning site (*i.e.* where first particles arrive in each case to pin the TL) in Figure 4.8 (e). It is within this narrow region that the disorganized structure was found in the 1000 mbar case and therefore the reason why we focus our attention there. Interestingly, these AFM measurements are also indicative of the dimensions of the droplet precursor film [3], which is of paramount importance in the prediction/simulation of droplet evaporation [129]. This is the first, to the best of our knowledge, that the dimensions of this film have been determined experimentally.

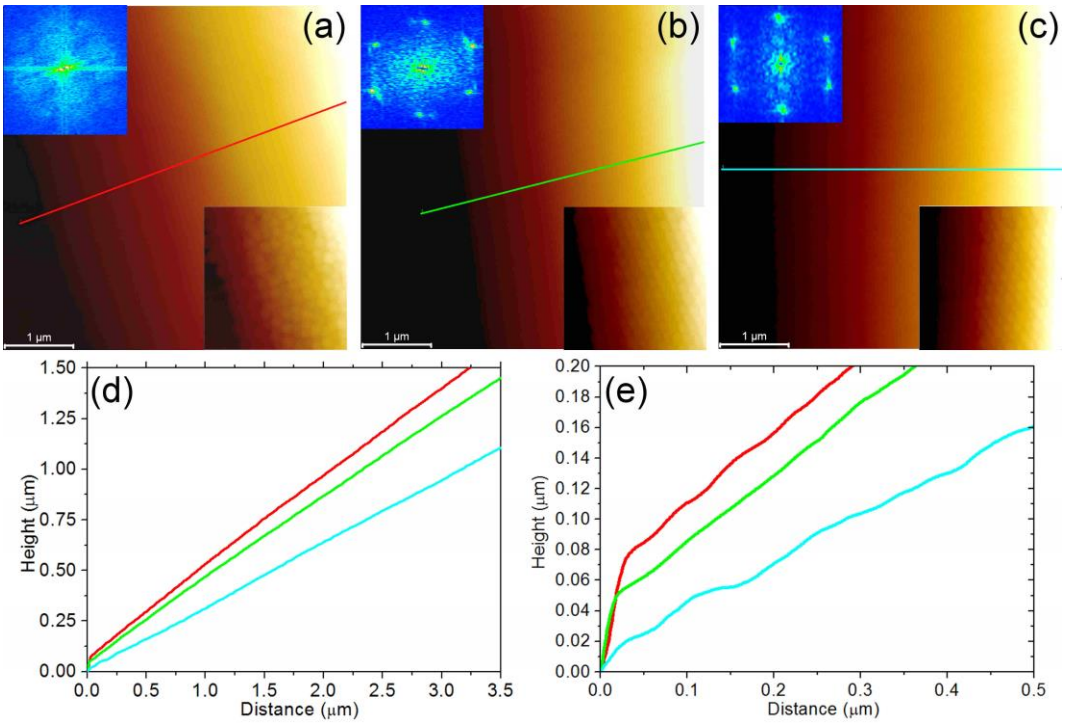

Figure 4.8: 5.0 × 5.0 µm^2 topography images of (a) 1000, (b) 750, (c) 500 mbar. Insets show magnifications (top) and FFT analyses (bottom) of random areas of interest at deposit edge. (d) Average height profiles corresponding to coloured lines in (a)-(c) respectively, (e) close-up of the first 0.5 microns of the height

profiles in (d). Insets were chosen in such a way as to better exhibit the promotion of crystallinity due to increasing velocity.

Combining the information presented in Figure 4.7 and Figure 4.8 for particle velocity and wedge constraints/disjoining pressure respectively, we can postulate that wedge constraint is acting as the main disordering parameter and particle velocity as the main ordering parameter. To better explain this, we plotted in Figure 4.9 the deposit height against $\bar{v}$, extracted from Figure 4.7, for all three cases and at certain distances from the periphery of the droplet (300, 500, 700 and 900 nm corresponding to black, red, blue and pink lines respectively) and toward the interior. The actual value of the velocities presented here are an order of magnitude smaller than the maximum attained presented in Figure 4.7. This could be attributed to the fact that $\bar{v}$ increases rapidly toward the end of the evaporation cycle (Figure 4.7), as a result of mass conservation and is in accordance with the literature [49]. The relation between deposit height and $\bar{v}$ was found to linear, in the form of $y = ax + b$, with a slope $-0.04 < a < -0.09$. We could presume at this point that decreasing deposit height, which is inversely proportional to disjoining pressures, hinders particle motion. On the other hand, the effect of disjoining pressure is possibly overcome by the increasing $\bar{v}$ (Figure 4.9, middle and right side points corresponding to 750 and 500 mbar respectively); hence leading to the crystalline structures observed in Figure 4.8 (b, c).

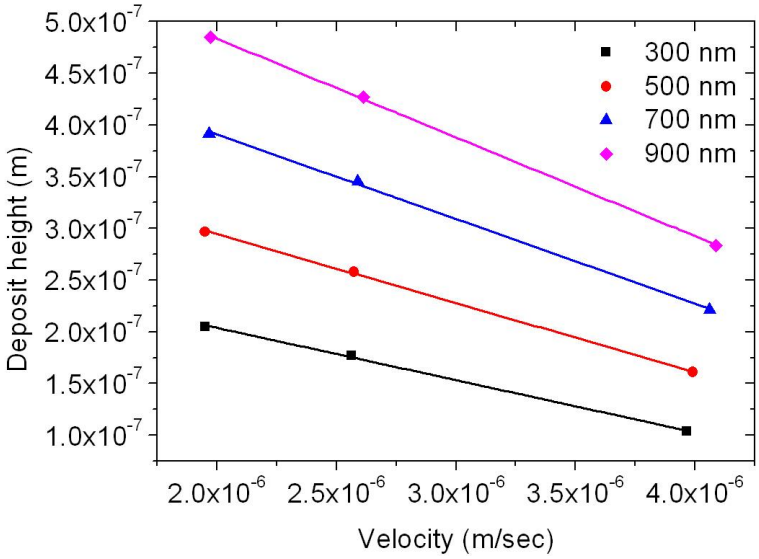

Figure 4.9: Deposit height at 300, 500, 700, 900 nm (black, red, blue and pink lines/symbols respectively) away from drop's periphery plotted against predicted particle velocity at same distance for 1000 mbar (points on the left), 750 mbar (points on centre) and 500 mbar (points on the right).

The above argument, provides a plausible description of the particle self-assembly mechanism very close to the actual contact line of an evaporating nanosuspension drop.

4.5. Conclusions

Freely evaporating sessile droplets containing monodisperse nano-particles were found to lead to the formation of particulate crystalline structures within the resulting ring-stains. This observation is valid for droplets evaporating both with permanently pinned TL and under the "stick-slip" regime, controlled by varying environmental pressure. We report on the unexpected formation of a disordered region at the exterior of a ring-stain deposit. Lowering environmental pressure as a means to increase

evaporate rate, led to promotion of crystallinity. Particle velocity was quantified and compared with experimental results, which led to the preposition of a tentative structuring mechanism. Essentially, during evaporation particle velocity acts as the main ordering parameter and disjoining pressure as the main disordering parameter. At the interior side of the ring, a similar disordered region was found and was attributed to the sudden cut-off of particle flow during the rapid TL motion.

The particles at the rest of the deposit formed mainly hexagonal structures with occasional square packed regions as each new particle layer formed. This behaviour was the result of particles trying to achieve the highest possible volume fraction within the limited wedge space. Deposit height was also found to promote crystallinity, due to kinetics.

Lastly, we attempted to determine the magnitude of the hysteretic/pinning barriers acting on the TL. To that end, we calculated the excess free energy, per unit length, of the system, which showed a peak just before each "slip" event occurs. This peak should be equivalent to the pinning barrier.

Chapter 5 On pressure and evaporation process and particle crystallisation

In the previous chapter we briefly described the effect of evaporation rate controlled by lowering environmental pressure on the ring-stain formation and particle deposition at the TL mechanisms. In this chapter, we probe this relationship further. Evaporation under lower ambient pressures was found to promote TL pinning and distinct patterns consisting of sets of rings, concentric rings and irregularly distributed stains were left behind. Each different pattern formed due to "stick-slip", CCR and very rapid evaporation respectively. At the nanoscale, lowering the pressure was found to promote crystallinity at the exterior edge of the deposits, observed as closely-packed, hexagonal conformations, due to the increased evaporation rate and hence particle velocity. However, lowering the pressure beyond the optimal, 500 mbar, a disordered region formed at the exterior edge of the ring. This formation was attributed to a combination of even higher particle velocity and very limited wedge space, for particles to self-assemble. Inside the rings, random groups of particle aggregates resembling branches were found which possibly formed during the "slip" of the TL. Further reduction of pressure resulted in the formation of particulate structures resembling ripples, forming on top of a particle monolayer with increasing, with lowering pressure, surface coverage. These structures are indicative of fluid flow being too weak to reach the TL but strong enough to carry particles over smaller distances during each "slip" event.

5.1. Evaporative behaviour and resulting ring-stains

Reducing the pressure at the environment around an evaporating colloidal droplet should increase the evaporation rate. In order to probe the effect of the increasing evaporation pressure on TL motion kinetics and the resulting ring-stains we reduced the pressure to 750, 500, 250 and 100 mbar. These values offer a wide pressure range below atmospheric, 1000 mbar, and down to the limit of the apparatus/ chamber, 40 mbar. Decreasing pressure should increase the evaporation rate due to increasing the effective diffusion coefficient of water, the base solvent, vapour in the atmosphere [14]. Indeed, we observed that in every case, decreasing pressure led to faster evaporation cycles and hence to different ring-stain deposits.

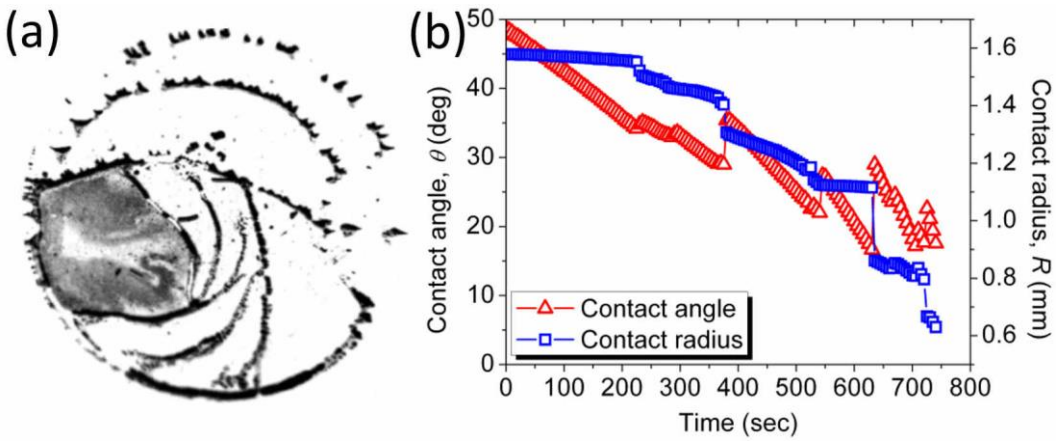

Figure 5.1: (a) Optical micrograph of the deposit resulting after a droplet containing 0.125% wt. SiO_2 nanoparticles evaporated under 750 mbar pressure. (b) Corresponding contact radius (squares) and angle (triangles) evolution over time.

At 750 mbar pressure, the evaporation of the droplet followed the "stick-slip" regime [73], producing a set of rings with a preferential pinning to one side (Figure 5.1(a)).

Upon closer inspection of Figure 5.1 (a), a number of discontinuous pyramidal particle deposits can also be identified. These structures appear to be oriented always with an angle to the liquid front and a side toward the interior. Essentially, during the first moments of the evaporation, particles arrive at the TL and pin it locally (exterior angle of the pyramid). Consequently, these pinning points lead to further particulate accumulation and in turn to the formation of the pyramids when the TL "slips". When these pinning points are dense enough, then a ring-stain is formed. Each ring seen in Figure 5.1 (a) can be related to a step in the evolution graph in Figure 5.1(b). These results are typical of "stick-slip" behaviour and are in line with the literature [36, 48, 73, 82, 83, 93, 130].

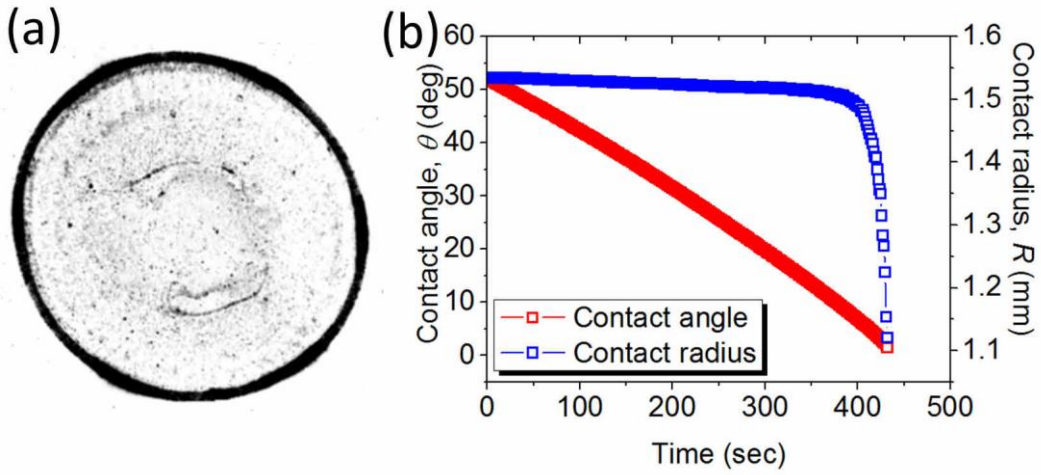

Figure 5.2: (a) Optical micrograph of the deposit resulting after a droplet containing 0.125% wt. SiO_2 nanoparticles evaporated under 500 mbar pressure. (b) Corresponding contact radius (squares) and angle (triangles) evolution over time.

Further reduction of environmental pressure resulted in promotion of TL pinning and hence in different evaporation behaviour. Essentially, evaporation followed the CCR regime in all the rest of lower pressure cases, with some differences in resulting patterns. At 500 mbar, a single ring formed, as seen in Figure 5.2 (a). This pattern is typical to CCR, with an example of the evolution over time of contact angle and radius in this evaporation regime presented in Figure 5.2 (b).

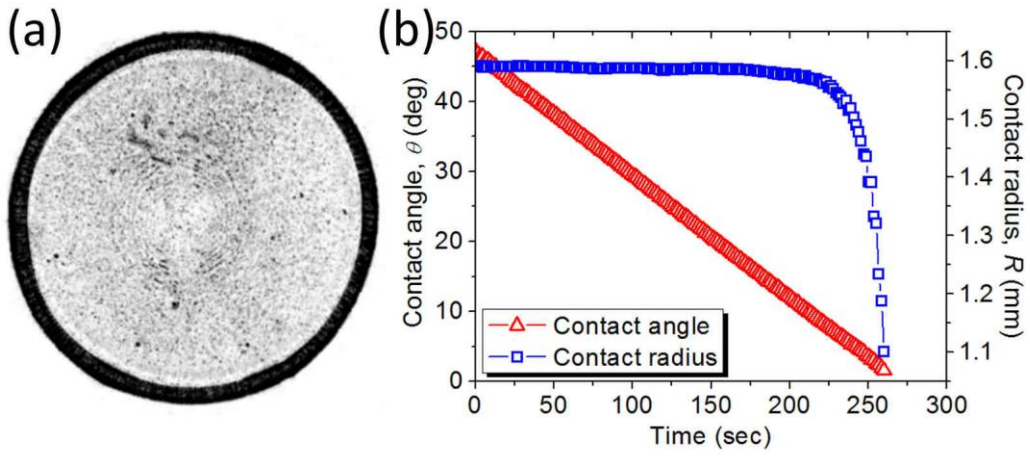

Figure 5.3: (a) Optical micrograph of the deposit resulting after a droplet containing 0.125% wt. SiO_2 nanoparticles evaporated under 250 mbar pressure. (b) Corresponding contact radius (squares) and angle (triangles) evolution over time.

Evaporation under 250 mbar pressure, resulted in a similar pattern, Figure 5.3 (a), and evaporative behaviour, Figure 5.3 (b). Both patterns for 500 and 250 mbar are in line with what has been reported previously for droplets evaporating under the CCR regime [19, 20]. Essentially, the outward fluid flow is enhanced by the reduction in pressure, leading to more particle accumulation at the TL [14]. This accumulation, in turn, pins the TL stronger leading to constant pinning and to the single ring observed. Increasing

particle accumulation results in wider rings which is crudely measured from the optical micrographs and is plotted against pressure in Figure 5.4 for the three pressure presented this far. Focusing our attention to the areas inside the rings, we can identify some particulate coverage resembling ripples, for the 500 and 250 mbar cases. For the 750 mbar case, no such coverage can be identified, possibly due to the rapid TL motion during each "slip" event allowing insufficient time for particle deposition into such features.

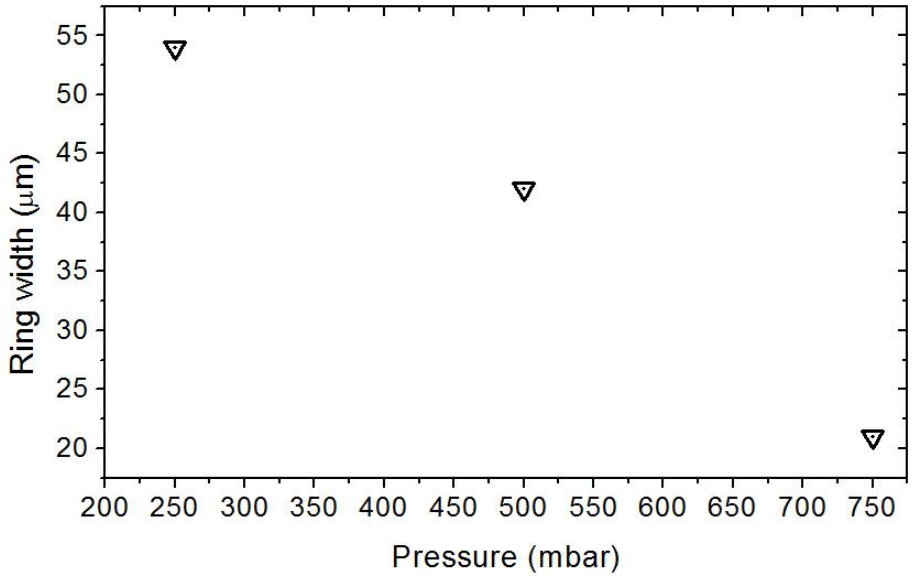

Figure 5.4: Effect of pressure on ring-stain width.

When the pressure was further reduced to 100 mbar, a rather unexpected, comparing to previous results, pattern was found, as presented in Figure 5.5. Although, the evaporation evolution (Figure 5.5 (b)) shows a constantly pinned behaviour, the resulting pattern appears to be irregularly shaped (Figure 5.5 (a)). More particulate

appears to have accumulated at the TL. At the interior, a different, thinner structure, "crust", has formed and perhaps a second ring at the centre. The irregularity of this pattern could be related with the extremely high (highest in this study) evaporation rate and hence limited time (~90 sec.). This evaporation rate induces a very high outward fluid flow which in turn forms a denser (seen as the darker region near the TL in Figure 5.5(a)) deposit of particles in areas near the TL. However, the evaporation is so rapid that particles have little time to be carried by the flow and essentially "freeze" in place, resulting to the interior features.

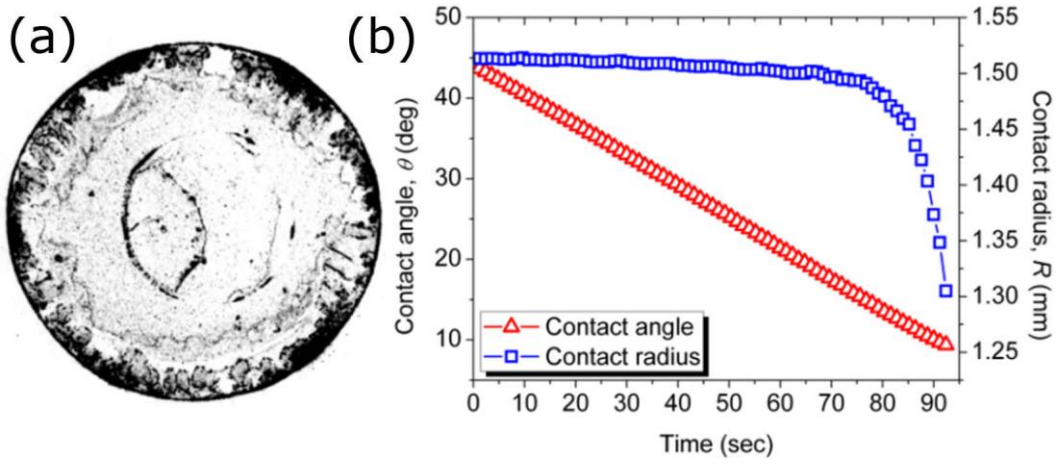

Figure 5.5: (a) Optical micrograph of the deposit resulting after a droplet containing 0.125% wt. SiO_2 nanoparticles evaporated under 100 mbar pressure. (b) Corresponding contact radius (squares) and angle (triangles) evolution over time.

5.2. Triple line motion and evaporation kinetics

Let us, here, attempt to elucidate the effect of pressure on the evaporation process. To achieve this, we extracted the average evaporation rate, $-dV/dt$, for each pressure from our experimental data and compared them with calculated ones based on

theoretical arguments. To calculate $-dV/dt$, we modified slightly the following empirical approximation [12]:

$$-\frac{dV}{dt} = \pi RDC_{sat}(1 - RH)(0.27\theta^2 + 1.30) \quad (4.1)$$

, where R and θ are the contact radius and angle respectively, D is the water vapour diffusivity, C_{sat} is the saturated water vapour concentration and RH is the relative humidity. As can be seen, this equation is not a function of pressure. However, $D$is dependent on the nature of the gas and inversely proportional to its pressure: $D \approx D_{ref}P_{ref}/P$, where D_{ref} is the value of D at the reference pressure P_{ref} 1000 mbar [14]. Hence, substituting this formula into Equation (4.1), yields the desirable equation as a function of P (note that all parameters are constant):

$$\frac{dV}{dt} \approx \left(\frac{dV}{dt}\right]_{ref}\frac{P_{ref}}{P} \quad (5.2)$$

where, the average experimental evaporation rate at ambient condition (1000 mbar) was measured to be: $\frac{dV}{dt}\Big]_{ref} \approx -2.8$ nL/sec. In Figure 5.6, we plotted the average experimental (t) and theoretical (circles) evaporation rate values, $-dV/dt$, against pressure on $\log_2$ scale. Additionally, in the inset we plotted the same data on a linear scale. A simple fit of the data presented in Figure 5.6, in the form of $-dV/dt = aP^{\beta}$, yielded a fitting parameter of $\beta \approx -1.01$ and $\beta \approx -1.00$ for experimental and calculated values respectively. The two trends are in good agreement with each other. Therefore, we can deduce that evaporation rate is (approximately) inversely proportional to pressure. A similar trend has been reported previously for "pinned" pure water droplets evaporating in a range of reduced pressure environments [14].

However, it is the first time to the best of our knowledge that such a result is reported for a nanosuspension droplet evaporating under low pressures.

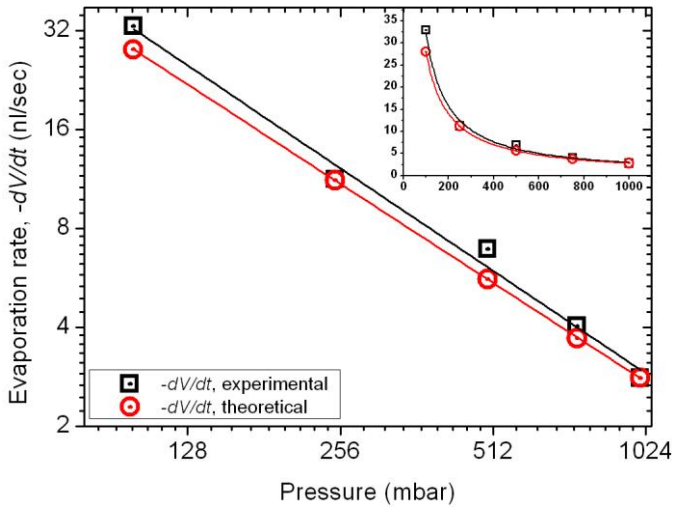

Figure 5.6: Effect of reducing pressure on evaporation rate: experimental (squares) and calculated (circles) values. Both axes are in $\log_2$ scale. Lines correspond to fittings of the calculated and experimental values respectively. Inset shows same data plotted on a linear scale.

Let us, here, attempt a quantification of the effect of pressure on the hysteretic energy barrier, U, pinning the droplets. As the droplets remain pinned, excess free energy, δG, accumulates in the system, due to contact angle not being at the equilibrium value, θ_0, following CCR evaporation. Therefore, we only have to calculate δG normalised per unit length of TL, $\delta \bar{G}$, for each system in question. To that end, we use the simple $\delta \bar{G}$ expression (Equation 1.4), proposed previously [36, 73, 131], as a function of contact angle change, $\delta\theta$. The evolution over time of $\delta \bar{G}$ for the four different environmental pressures are plotted in Figure 5.7. The value of the surface tension of our nanofluid

drop was measured using the pendant drop technique (described in 3.2.2) and was found to be that of pure water, *ca.* 0.073 N/m.

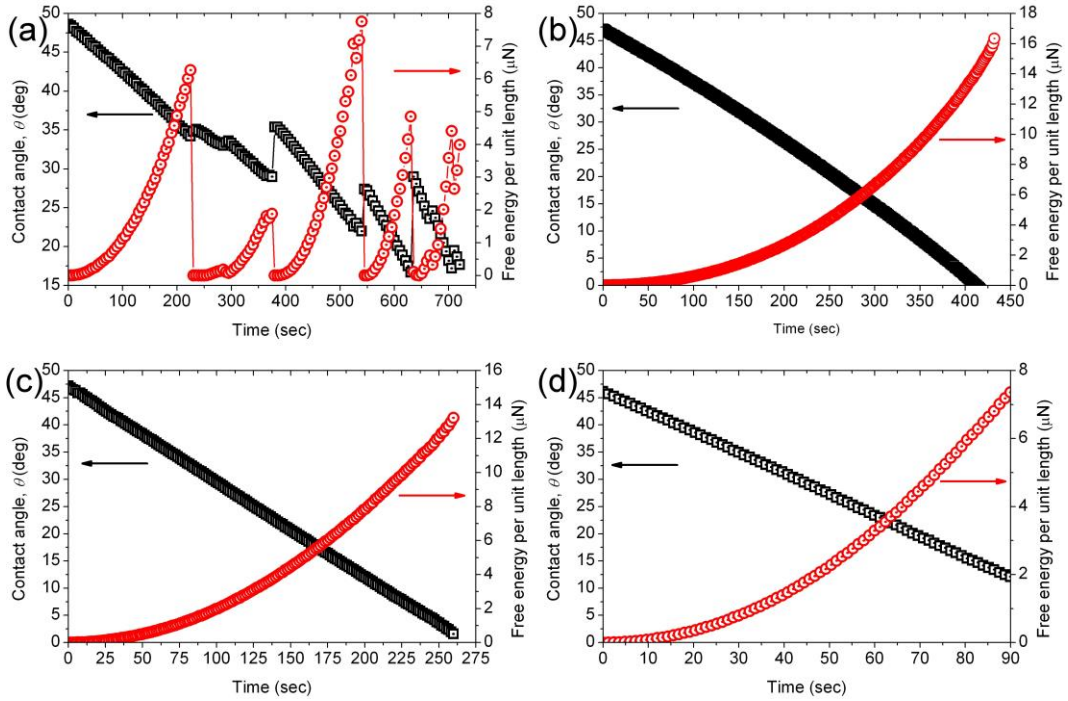

Figure 5.7: $\delta\bar{G}$ (circles) and contact angle (squares) evolution over time with reducing environmental pressure to 750, 500, 250, 100 mbar from (a) to (d) respectively. Arrows point to corresponding axis for each curve.

In the "stick-slip" case (Figure 5.7 (a)), $\delta\bar{G}$ increases rapidly before each "slip" event and then sharply drops to virtually zero. Before each "slip" event, the droplet is out of equilibrium hence $\delta\bar{G}$ builds up. Once its value reaches and/or exceeds the hysteretic energy barrier, the TL should "slip" to the next energetically favourable position, consuming the excess energy in the process. In Figure 5.7 (a), it can be seen that for a "slip" to occur, $\delta\bar{G}$ needs to attain a minimum of $4-8$ μN (*i.e.* this is an estimate for the energy barrier, for evaporation under 750 mbar pressure). These results are in

agreement with what has been previously reported for the energy barrier in similar "stick-slip" cases. In particular, the hysteretic energy barrier for a pure liquid drop was found to be in the order of magnitude of 10^{-7} N [131]. However, the addition of nanoparticles to a similar system, was found to increase the energy barrier to a maximum order of magnitude of 10^{-6} N, for the concentrations studied. This could be attributed to a number of reasons, such as increased effective local roughness due to the deposit forming or a possible modification of the energy balance. Mathematically, the change in the contact angle, $\delta\theta$, and the distance travelled by the TL, δR, in every "slip" should increase with concentration and hence the barrier should also increase [36].

Focusing our attention to the constantly pinned cases, $\delta\bar{G}$ was found to increase exponentially over time, with a maximum attained value of *ca.* 16 μN as shown in Figure 5.7 (b)-(d). The small discrepancy in the maximum value seen in Figure 5.6 could be the result of the range of $\delta\theta$. In this case, it only reaches a value of *ca.* 45º, attributed to drop shape near the end of the evaporation process becoming too irregular to be followed and analysed by DSA. As a result, and considering that Equation 4.3 is a function of $\delta\theta$, a smaller, yet consistent, $\delta\bar{G}$ value is acquired. The value calculated in this case is *ca.* 8 μN, similar to the "stick-slip" case. However, as the evaporation in this particular case is very rapid (~90 sec.), we could stipulate that there is insufficient time for TL recession, since the droplet dries out before that. Comparing the $\delta\bar{G}$ between the "stick-slip" case (Figure 5.7 (a)) and the rest of the cases (Figure 5.7 (b, c)) we can see $\delta\bar{G}$ in the latter cases increasing beyond the barrier value $4-8$

μN in the former cases. This could be attributed to increasing particle accumulation, locally, at the wedge area, which was crudely presented in section 5.1 and will be discussed in depth later. Additionally, $\delta\bar{G}$ was reported to be proportional to particle concentration [36] which resulted in the conclusion that $\delta\bar{G}$ should attain higher values, as pressure is lowered, although, never reaching the hysteretic energy barrier.

5.3. Particle deposition and self-assembly mechanism

In this section, we attempt to assess the relation between deposit shape and nanostructuring mechanism and pressure. To achieve this, the resulting coffee-rings were scanned with AFM at various locations and across the width of each ring in consecutive images of the same scan size. We present, here, characteristic images of each sample, in a way that allows the observation of both the deposit shape and the crystal structure at the same time. In every consecutive image, the *z*-scale is zeroed to the top of the previous one for better visualisation and the droplet centre is everywhere on the right. Furthermore, the corresponding FFT analyses of each area are included as insets, in order to identify any potential crystalline structures.

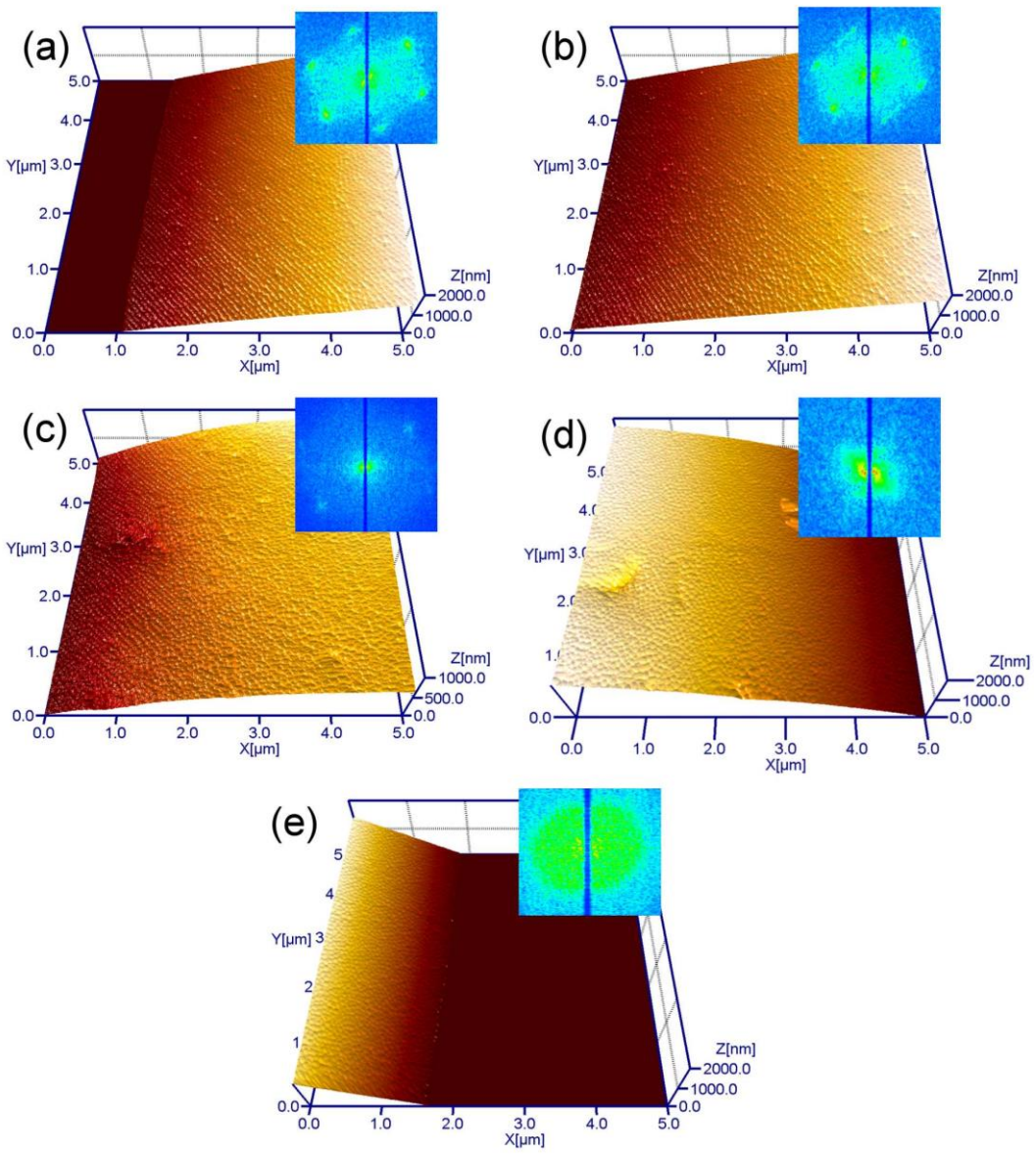

Figure 5.8: (a)-(e) Sequential 3-D representations of areas of the ring-stain scanned across the 750 mbar ring-stain width. Corresponding FFT analyses are presented as insets in each image. Droplet centre lies to the right of each image.

The shape of the ring left behind after evaporation of the fluid under 750 mbar pressure, which followed the "stick-slip" regime, is presented in the images in Figure 5.8. In more detail, a gentle slope gradually builds up (from the drop exterior), as seen

in Figure 5.8(a)-(b), until reaching a plateau in Figure 5.8(c). This deposition could be the result of the pinned TL and the resulting outwards flow, during a "stick" phase, carrying particles to the droplet's periphery [19, 20]. The plateau is followed by a steeper slope, with decreasing height, as seen in Figure 5.8(d)-(e). This slope could be attributed to the abrupt motion of the TL during "slip" and is in agreement with the literature [47, 93]. Furthermore, the deposit could act as an artificial defecting which interferes with fluid flow and hence leads to a "slip" event [78, 93]. Essentially, as the deposit grows, it should eventually interrupt the outward liquid flow replenishing the evaporated liquid, leading to a depinning and hence to particles "freezing" in place in the disordered region.

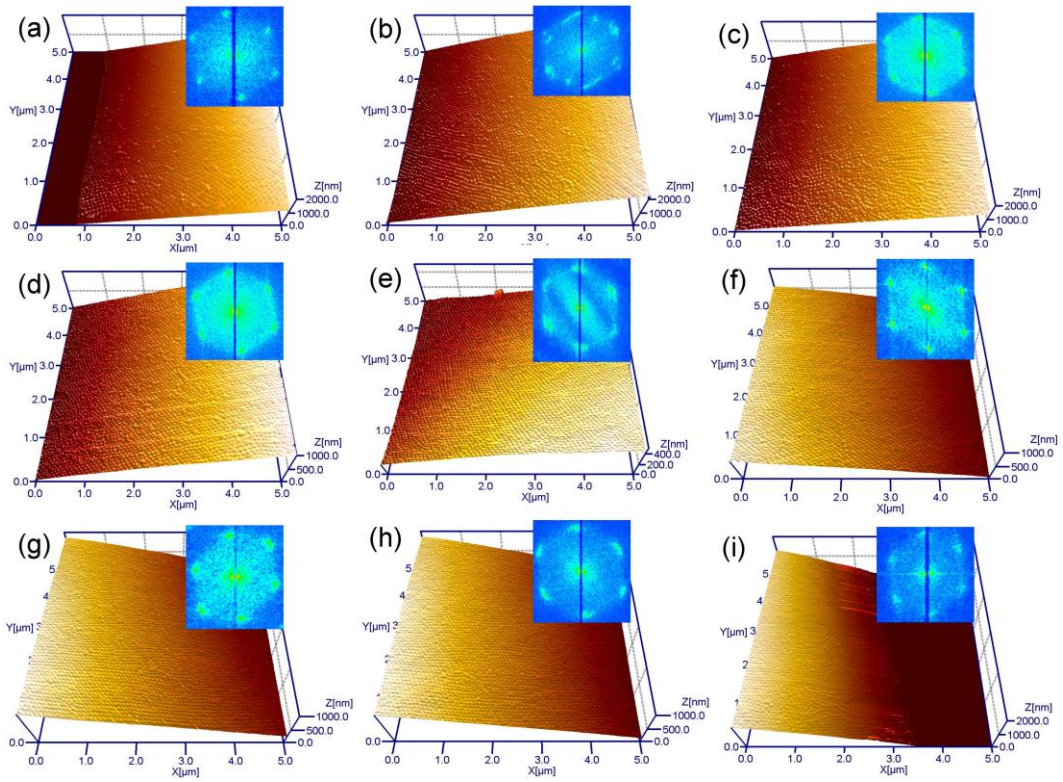

Figure 5.9: (a)-(i) Sequential 3-D representations of areas of the ring-stain scanned across the 500 mbar ring-stain width. Corresponding FFT analyses are presented as insets in each image. Droplet centre lies to the right of each image.

The evaporation under 500 mbar pressure, evolved with a constantly pinned TL. This resulted in a single, uniform ring-stain, which is presented in Figure 5.9. During the pinned stage of the evaporation cycle (<400 sec., Figure 5.2 (b)), the deposit builds up, as seen in Figure 5.8 (a) – (e). Eventually, a transitory point is reached (~ 400 sec., Figure 5.2 (b)) when the TL starts retracting. At this moment, fluid and hence particulate flow becomes insufficiently strong to support any further deposition and height increase. Therefore, the deposit peak is formed (Figure 5.9 (e)) and subsequently, the height starts decreasing due to the weakening flow (Figure 5.9 (f)-(i)). Additionally, direct comparison of the interior slope in the "stick-slip" case

(Figure 5.8) and this case (Figure 5.9 (f)-(i)), reveals that the deposit is more symmetrical in the latter case. Furthermore, we should note that the crystal structure, shown in the insets, at this case is almost everywhere hexagonal, however, the exact effect of pressure on the particle self-assembly mechanism will be discussed in detail later.

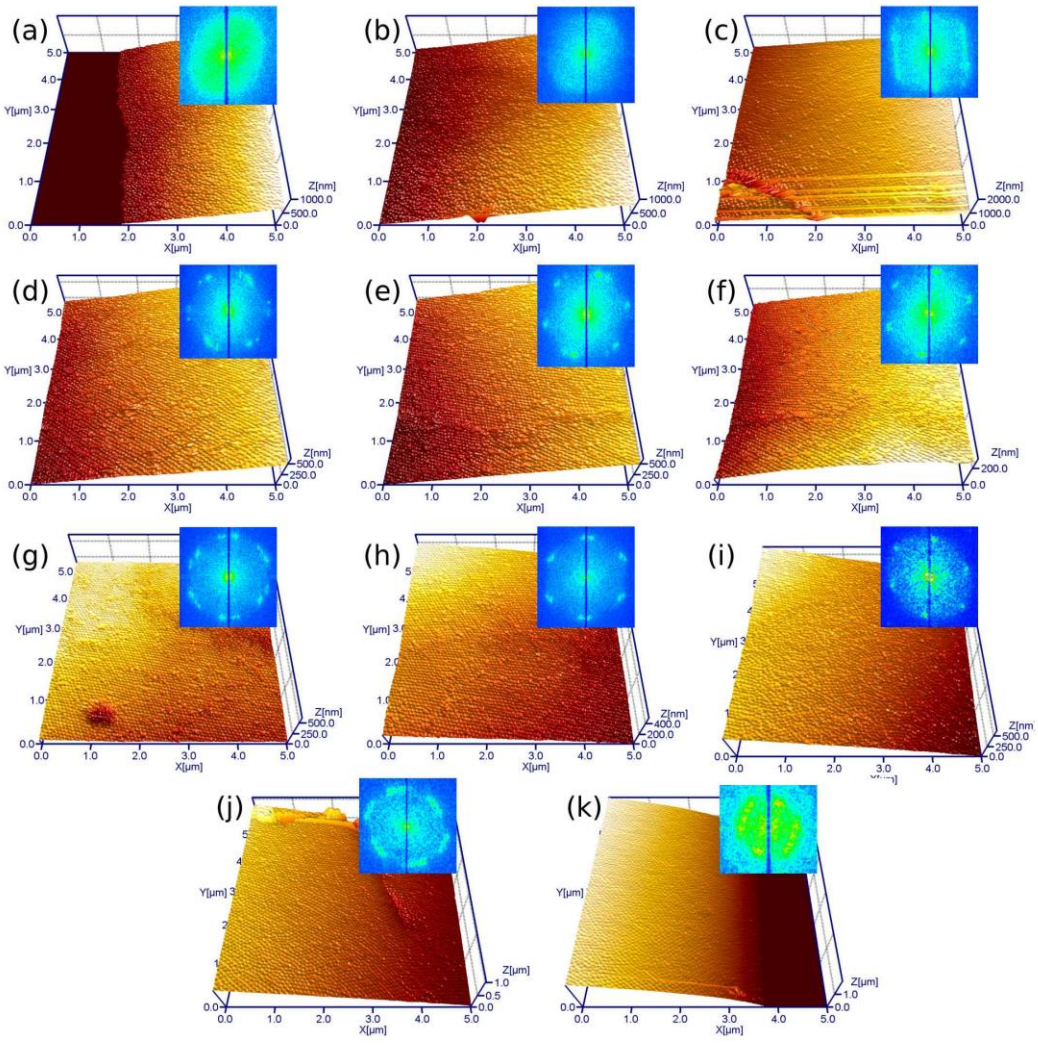

Figure 5.10: (a)-(k) Sequential 3-D representations of areas of the ring-stain scanned across the 250 mbar ring-stain width. Corresponding FFT analyses are presented as insets in each image. Droplet centre lies to the right of each image.

When the evaporation evolved under 500 mbar, the resulting deposit appears to be similar in shape, yet wider, as seen in Figure 5.10. The plateau in this case is larger and with a higher number of defects, possibly as a result of the increased evaporation rate. Furthermore, a number of irregularities were discovered (*e.g.* FFT insets in Figure 5.10(d),(j)), attributable possibly to the orientation of different crystal grains, still hexagonally close-packed. The formation of these grains could have formed due to a defect (as the "holes" and "cracks" shown in Figure 5.9 (c) and (g)), affecting the orientation of the crystal during its growth.

Considering these nanoscale findings, we can at this point postulate how pressure affects particle self-assembly. Figure 5.11 depicts an oversimplified schematic representation of the observed structures presented above. This schematic is a result of the FFT analysis of each case, similar to the ones presented above, and the symbols d and o correspond to disordered and ordered regions respectively. In addition, the self-assembly behaviour of nanoparticles in a droplet that was left to evaporate at ambient conditions (1000 mbar, presented in Chapter 4) is included in order to help us determine the effect of pressure in a wider range, 1000 – 250 mbar.

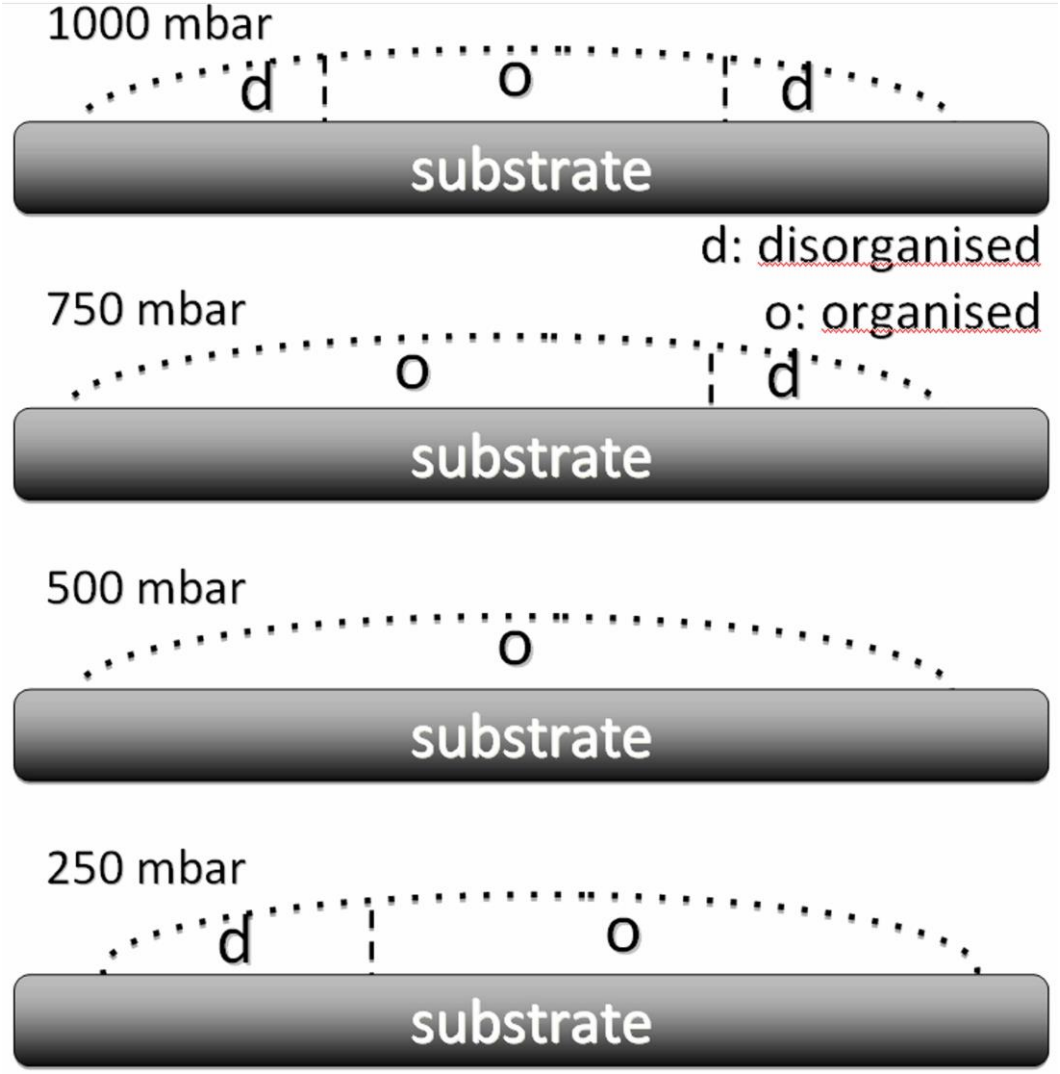

Figure 5.11: Schematic representation of particle structure of TL deposit formed at different ambient pressures. First two drawings correspond to "stick-slip" evaporation, latter two to constantly pinned drops; d = disorganised (amorphous), o = organised (crystalline). Droplet centre lies to the right of each presented deposit.

At first glance, the results summarized in Figure 5.11 show no obvious order, however we shall attempt to propose a plausible interpretation of structuring mechanism. The particles in this study are smaller, compared to the work reported elsewhere [49], and therefore they can reach closer to the actual liquid wedge at the TL, as discussed in

section 4.4. Essentially, at the wedge structural but mainly conventional disjoining pressure effects may be felt by the particles resulting to disordering. As conventional disjoining pressure is known to increase with decreasing film thickness [132]. In our case, the wedge is so thin as to be considered a thin film. As this thin film is located at the very edge of the drop periphery it could be correlated with the precursor film of evaporating droplets [129]. These results further support our findings in 4.4, of the dimensions of the paramount precursor film. Therefore, we could assume that disjoining pressure is the main disordering reason, hindering particle Brownian motion. On the contrary, the laminar, outward liquid flow should be our main ordering parameter, by providing particles with enough kinetic energy to overcome the "conventional" disjoining pressure effect and promoting crystallinity, as seen in Figure 5.11 in the cases of 1000, 750 and 500 mbar. Further away from the wedge area, the disjoining pressures weaken and hence crystallinity can be achieved. The disordering at the interior side of the ring for both 1000 and 750 mbar pressures is attributable to the rapid "slip" of the TL, allowing little time for ordering. Notably a disordered region formed at the exterior edge of the ring seen in the 250 mbar case. To understand how this region formed, deposit dimensions were extrapolated from AFM data and are presented in Figure 5.12. It is obvious from this image, that in the 250 mbar case, the available space at the TL is the most limited that the particles cannot overcome the disjoining pressure effect. These ideas clearly merit further investigation in the future.

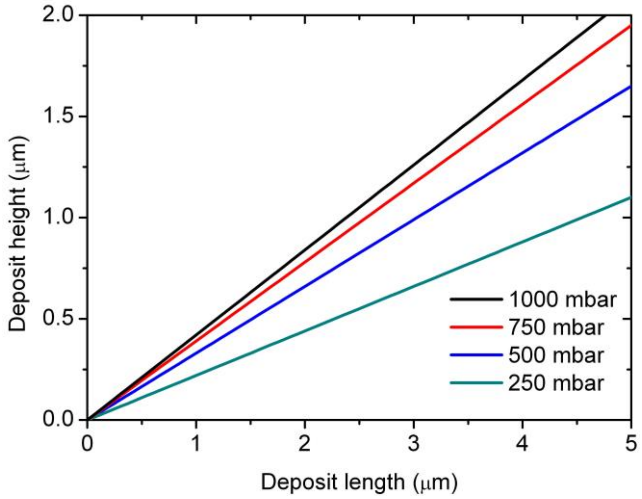

Figure 5.12: Deposit height plotted as a function of deposit length (linear approximation from AFM data) for 1000, 750, 500 and 250 mbar pressure corresponding to black, red, blue and green line respectively. This figure, essentially, depicts the wedge constraint and/or available space in each case.

We have not managed to acquire good AFM images of the samples formed under 100 mbar pressure, probably due to its highly irregular structure and sudden height differences.

5.4. Particle self-assembly at the interior of the rings

The effect of reducing pressure on particle self-assembly at the interior of the rings (area covered by liquid during evaporation) was also probed. Two distinct types of behaviour were found and are presented here.

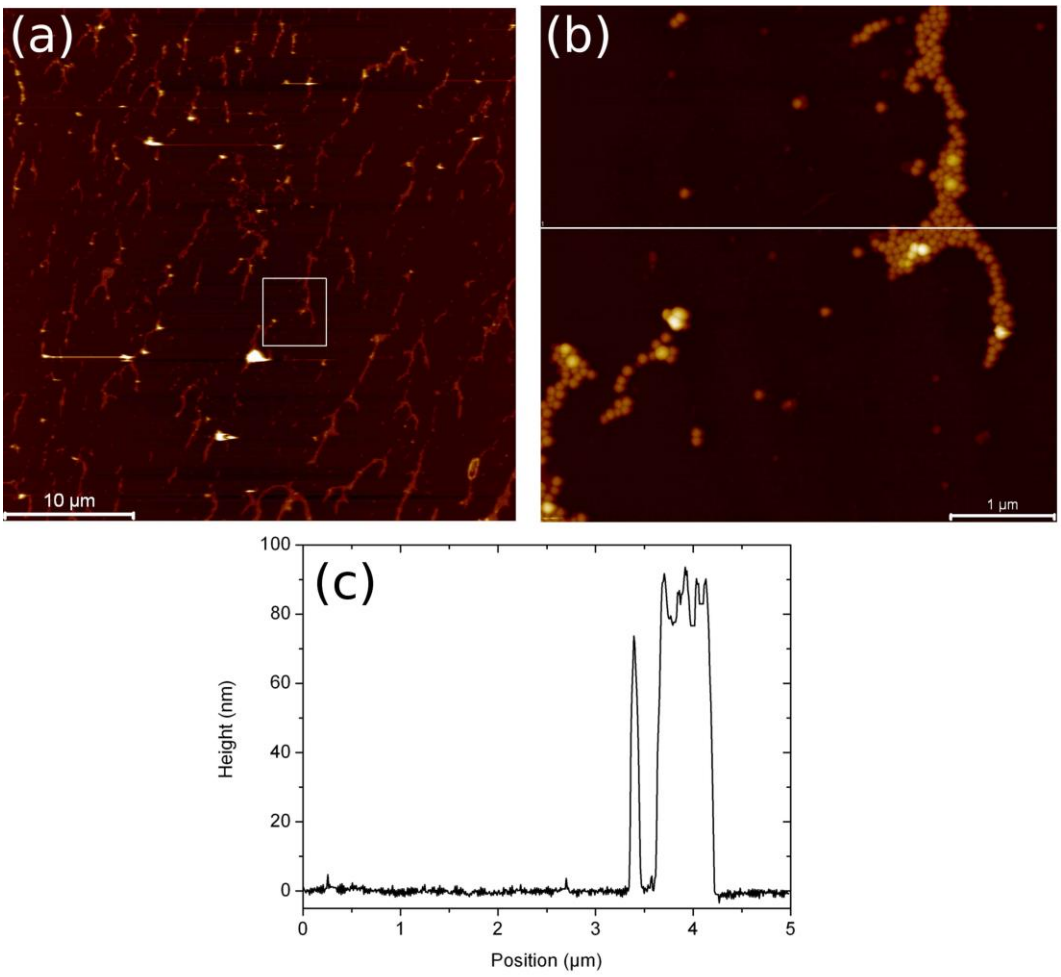

Figure 5.13: (a) 40 x 40 µm^2 topography image of the 750 mbar sample. (b) Magnification of boxed area in (a). (c) Height profile corresponding to line scan in (b).

The topography images in Figure 5.13, unveiled particles depositing themselves in random groups resembling branches in the area between two rings, which occurred after "stick-slip" evaporation (750 mbar, see Figure 5.1). Magnifying one of these random branches, Figure 5.13 (b), provides further insight into their self-assembly behaviour. These structures are relatively narrow (~ 10 particles wide) and usually one particle high (~ 80 nm), as exhibited in the height profile in Figure 5.13 (c). Essentially,

when the TL "slips" (bottom right part of the image), particles arriving at the TL lead to small, weak "anchoring" events and hence to the formation of the observed groups of aggregates.

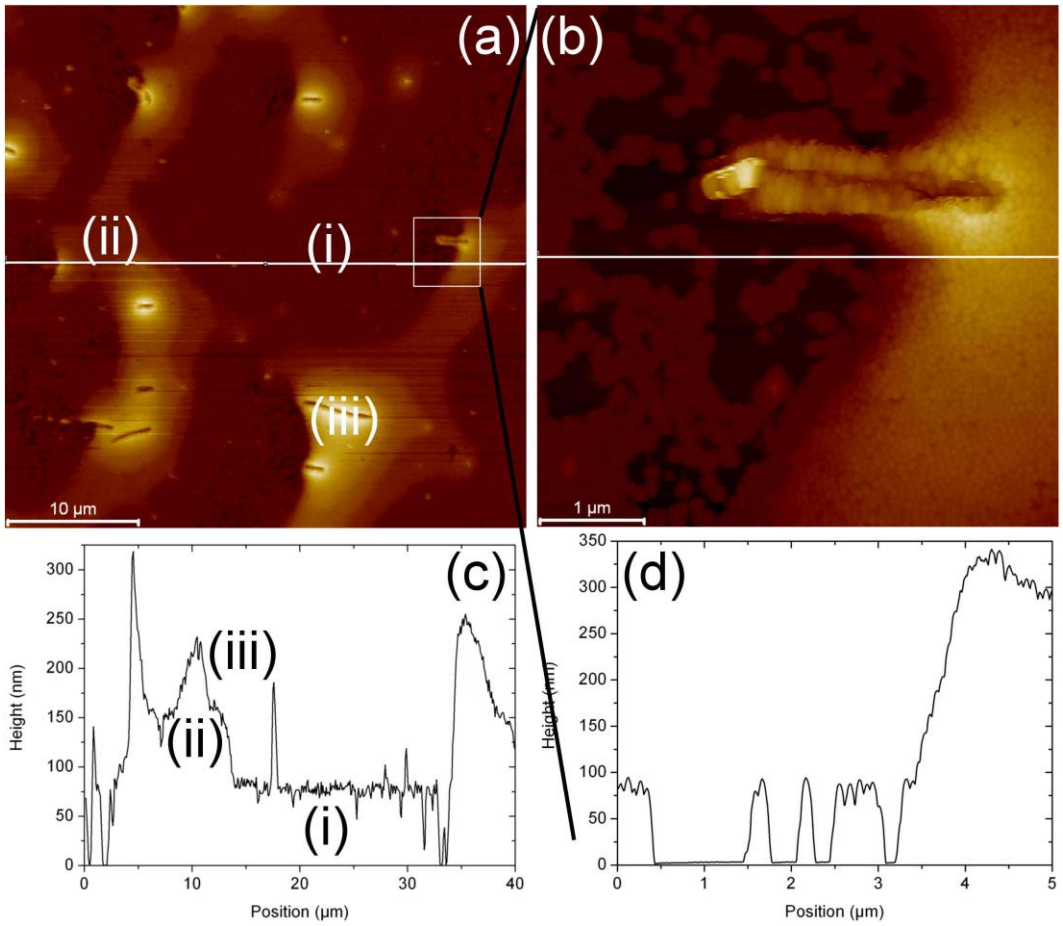

Figure 5.14: (a) 40 x 40 µm^2 topography image of the 500 mbar sample. (b) Magnification of the boxed area in (a). (c), (d) Height profiles corresponding to lines in (a) and (b) respectively. (i), (ii), and (iii) mark respectively a monolayer, a bi-layer and a multi-layer (3-4).

Lowering the ambient pressure further to 500 mbar and 250 mbar resulted in the formation of a second type of structuring. Focusing our attention on the 500 mbar case,

particulate can be clearly identified to cover the majority of the surface (Figure 5.14 (a)). In more detail, the particulate formed a continuous monolayer (darker coloured regions, (i)), with occasional bi-layers (ii) and multi-layers (iii) building on top of it. The corresponding height profile, shown in Figure 5.14 (c), presents the exact height of the layers. The taller structures (iii) have a maximum height of approximately four particle diameters (~ 320 nm). In addition, their shape resembles ripples originating from the centre of the droplet (as seen in the optical micrograph in Figure 5.2 (a) and towards the bottom right of Figure 5.14 (a)). A further interesting feature to note is that of less surface coverage, seen as the darkest spots, next to the peaks of the ripples, to be discussed later. This feature is highlighted in the magnification of such an area and its corresponding height profile in Figure 5.14 (b) and Figure 5.14 (d), respectively.

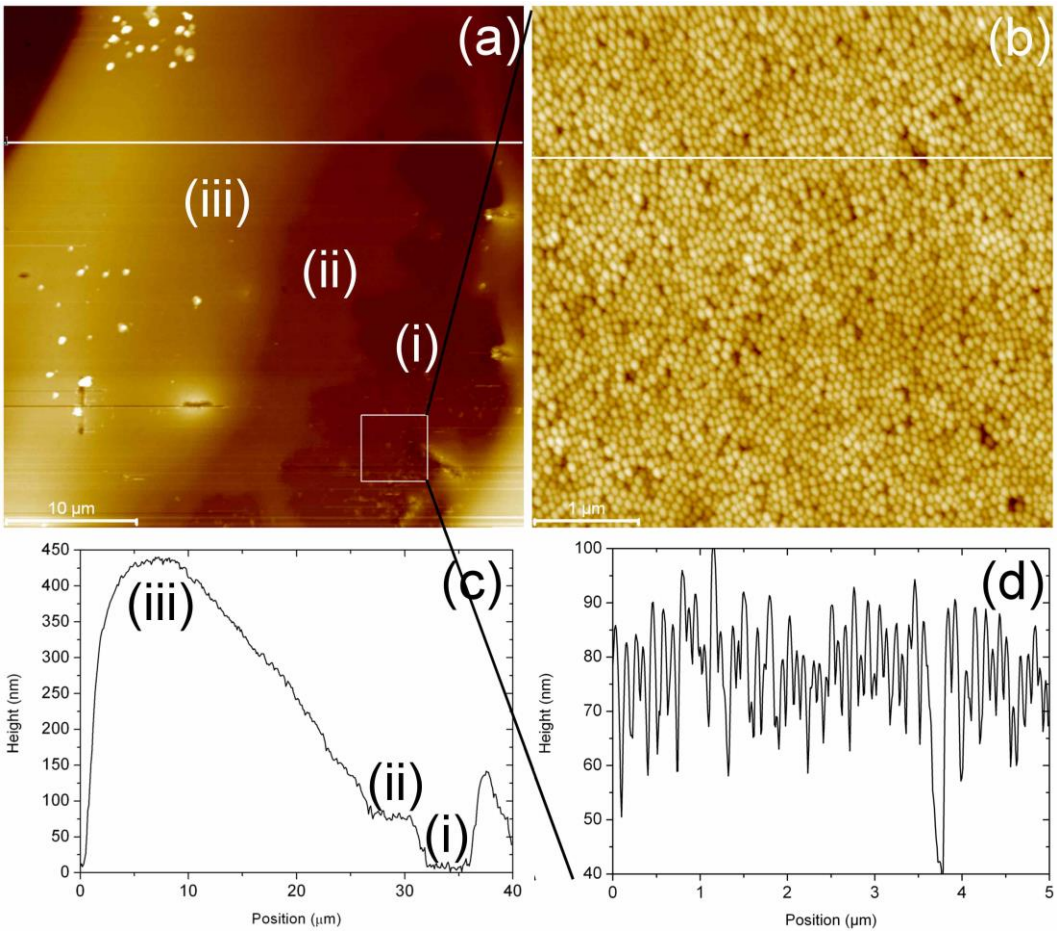

Figure 5.15: (a) 40 x 40 µm^2 topography image of the sample which evaporated under 250 mbar pressure. (b) Magnification of area highlighted within white box in (a). (c),(d) Height profiles corresponding to lines in (a) and (b) respectively. (i), (ii), and (iii) mark respectively a monolayer, a bi-layer and a multi-layer (4-5).

Moving on to the last sample, 250 mbar, we can readily identify similar structures. These structures are presented in Figure 5.15 (a) along with their corresponding height profile in Figure 5.15 (b). The ripples are clearly distinguishable to be taller and wider, due to increased outward liquid and hence particle flow, as discussed earlier. Additionally, the increased flow leads to better surface coverage, as seen in Figure 5.15 (b) and (d), at the areas next to the peaks. The white spots in Figure 5.15 (a) have

not been explained, but are probably tip artefacts or randomly deposited particles on top of the structure.

Let us, here, attempt to describe the formation of these complex structures in the lower pressure cases (500 and 250 mbar). In both cases the droplet evaporates following the CCR regime for the better part of the process (<400 and <200 sec, as shown in Figure 5.2 (b) and (d) respectively). This induces an outwards fluid flow to the TL in order to replenish the liquid lost to evaporation. Eventually, depinning occurs and the TL retracts. During TL retraction, lower pressures enhance the evaporation rate and hence the drying at the TL. Consequently, TL retracts quicker leading to "spreading of the deposit". At the same time, the TL recession is so rapid (compared to the pinned period) that no further pinning occurs and therefore no structures are formed, as those seen in section 5.3. Some occasional, weak pinning events should occur locally giving rise to the multi-layered structures observed in each case. Moreover, the fluid flow is suppressed by these structures leading to lower surface coverage immediately adjacent to the peaks of the ripples (*e.g.* Figure 5.14 (c)). Reducing the ambient pressure and hence enhancing the fluid flow leads to better surface coverage (*e.g.* Figure 5.15(c)).

5.5. Conclusions

The effect of lowering the environmental pressure around a nanofluid droplet containing monodisperse spherical particles was thoroughly investigated. Reducing pressure promoted the pinning of the TL and led to two different evaporation

behaviours, “stick-slip” and CCR. Additionally, three distinct patterns were found: a) a set of concentric rings with a “preference” to one side (evidence of “stick-slip” regime), b) uniform, unique rings (constantly pinned TL) and c) an irregularly-shaped deposit with higher particle accumulation near the periphery (very rapid evaporation). Furthermore, this is the first time, to the best of our knowledge, that the inversely proportional relationship of pressure and evaporation rate have been reported for droplet containing particles of this range (~80 nm). Moreover, we quantified the hysteretic energy barrier pinning each droplet.

Reducing pressure was also found to promote crystallinity within the ring-stains. Reducing pressure to 500 mbar led to CCR evaporation which, in turn, resulted in the formation of hexagonal, close packed structures throughout the ring-stain, making this the “optimal” pressure. Further pressure reduction to 250 mbar had the opposite effect, leading to a disordered region at the exterior deposit edge, due to the more limited space at the wedge for particles to orient.

Particle self-assembly at the area inside the rings (bulk of initial drop) was also probed and found to follow two distinct behaviours. In the “stick-slip” case, 750 mbar, groups of particle aggregates, resembling branches, formed due to weak “anchoring” events. When the pressure was further reduced, particulate monolayers were found in the same areas with increasing surface coverage. On top of these layers, particulate ripples formed and their height increased with reducing pressure. This phenomenon was attributed to quicker drying and therefore rapid recession of the TL due to reducing

pressure. During this TL travel, weak local pinning events probably gave rise to the afore mentioned particle structures.

These findings allow further insight into the coffee-stain mechanism and in particular they offer a means of controlling and promoting the crystallinity of the resulting ring-stains. In turn, these well-defined, hexagonally packed crystalline rings could find potential use in various nanotechnological applications requiring specific patterned surfaces with nanoscale detail.

Chapter 6 On particle shape and evaporation process and crystallisation

In this chapter, the effect of particle shape on TL motion kinetics, ring-stain formation and nano-structuring within the resulting rings is probed. A wide range of shapes were investigated from symmetrical nano-spheres to highly irregular shaped carbon nanotubes (CNTs) and grapheme platelets, which were categorised according to aspect ratio. Initially, the effect of particle geometry on the evaporative behaviour (promotion of "stick-slip" or CCR) is presented. Additionally, the hysteretic energy barrier pinning the droplet in each case was calculated and was found to be proportional to particle aspect ratio. Subsequently, the nanostucturing mechanism of the particles at the TL was investigated. Coupling macroscale results (evaporation behaviour) with the nano-structuring information led to the proposition of a particle self-assembly mechanism at the TL for all cases here. Essentially, wedge constraints and flow velocity were found to be the two main parameters affecting the self-assembly process and each particle shape was found to adapt differently to them. We hope these findings to act as the basis for future development within the field of surface patterning and consequent tailoring of this simple and inexpensive technique, coffee-stain phenomenon, to potential nanotechnological applications.

6.1. Evaporative behaviour

The effect of particle shape on the evaporation behaviour of nanosuspension drops was assessed first. To that end, the evolution over time of contact angle, θ, and radius, R, for solutions containing particles of various geometries, namely graphene platelets, nano-spheres [36, 83] and carbon nanotubes (CNTs) [101] are compared in Figure 6.1. These particles were categorised according to aspect ratio using the formula [133, 134]: $a \equiv z_m/r_m$, where z_m and r_m are the two semi-axes of length. The axis of revolution is what really defines these particles with CNTs revolving around their larger axis ($a \approx 100$) and graphene platelets around their smaller axis ($a \approx 0.01$). The third shape, spheres, are symmetrical and hence their aspect ratio is $a \approx 1$. The details of each particle in this comparison are summarised in Table 6.1.

Table 6.1: Dimensions, aspect ratio, α, and bibliographic reference of the particles included in this comparison.

Shape	Length semi-axis, r_m (nm)	Length semi-axis, z_m (nm)	Aspect ratio, α	Ref.
Spherical	~25	~25	1	[36, 83, 93]
Rod-like (CNTs)	~1	~100	100	[101]
Platelets (graphene)	~200	~2	0.01	This work

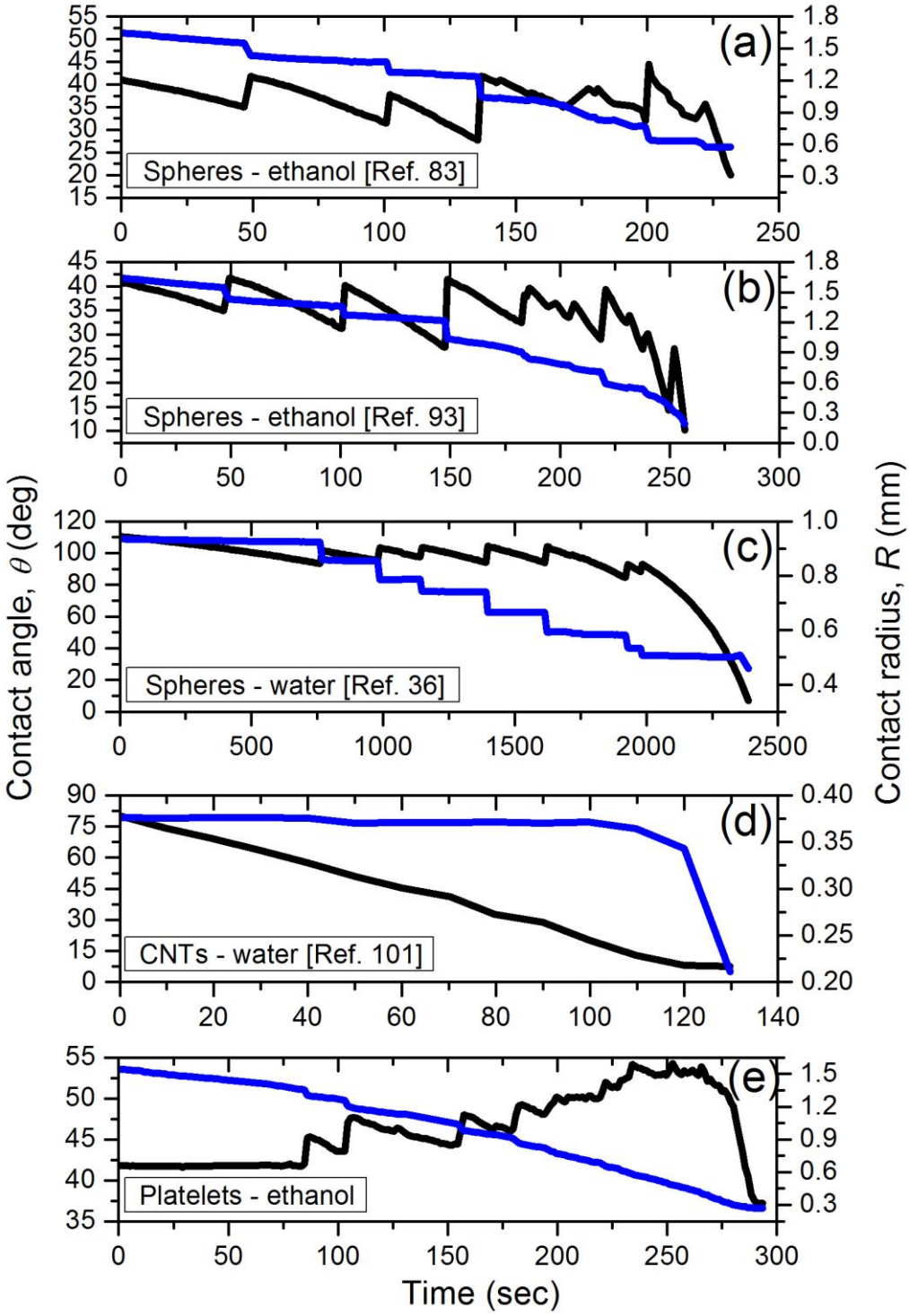

Figure 6.1: Evolution over time of contact angle, θ, (black) and contact radius, R, (blue) for free drying nano-suspension droplets of (a, b) 0.1% w/v nano-

spheres in ethanol [83, 93] and (c) 0.1 % w/v nano-spheres in water [36] on PTFE, (d) 0.25 % w/v CNTs in water on OTS-treated silicon [101], and (e) 0.1 % w/v platelets in ethanol on PTFE.

Figure 6.1 depicts the evaporation cycle for droplets containing (a-c) nano-spheres, (d) CNTs and (e) graphene platelets. Typical "stick-slip" evaporation can be readily identified in Figure 6.1 (a-c) corresponding to the drops containing nano-spheres. One interesting feature is readily apparent in these cases. During each "stick" event, the TL can be distinguished to slowly drift, in the first two cases corresponding to ethanol suspensions, Figure 6.1 (a-b), while it remains pinned in the water case Figure 6.1 (c). Since in all these cases similar in composition, hydrophobicity and roughness PTFE substrates were used, then we can deduce that the interactions between the liquid molecules, the substrate and the particles is the underlying reason for this difference.

On the contrary, CNTs (Figure 6.1 (d)) appear to promote TL pinning, resulting in CCR evaporation. More specifically, R, remains pinned and θ decreases linearly for most of the evaporation cycle (*ca.* 110 sec.). At this point TL depins and retracts until full evaporation (~130 sec.). Lastly, graphene platelets exhibited a unique evaporation behaviour resembling that of "stick-slip", to be discussed next. Evaporation under different regimes, "stick-slip" and CCR, should be a first indication of the impact of the particle geometry on TL pinning.

In the last "stick-slip" case, Figure 6.1(e), the evaporation of a droplet containing graphene platelets exhibited a unique behaviour bearing some "stick-slip"

characteristics. In more detail, during the first moments (~ 80 sec.), the droplet evaporates with constant θ and a receding R, typical of C*CA*. As evaporation continues, the local viscosity at the TL should increase due to increasing particle concentration [83]. At approx. 80 sec., perhaps due to a surface defect and local fluid viscosity becoming sufficiently high, the TL pins with a preference to one side, while the other side of the TL "slips" to the next energetically favourable position. Notably, at this point, R retracts sharply and θ jumps to a value higher than the initial one, $\theta_0 \approx 42^o$; the main difference between this case and the rest of the "stick-slip" ones. Furthermore, at this point the system enters its first "stick" event during which the TL slowly drifts, inducing an outward fluid flow. In turn, this flow carries and deposits more particles at the TL where they enhance the pinning, typical of ethanol nanofluids [83, 93], until another "slip" event occurs. The rest of evaporation follows this unique "stick-slip" behaviour which results in the formation of concentric rings, to be presented later. This is the first, to the best of our knowledge, mention of this unique to graphene ethanol nanofluids evaporative behaviour.

6.2. Triple line motion and evaporation kinetics

Let us now focus our attention on the TL motion kinetics of each case. In this regard, we compare in Figure 6.2 the change in contact angle, $\delta\theta$, and in contact radius, δR, for the five first TL jumps in each "stick-slip" case (Figure 6.1 (a-c), (e)). We also present the average value, dashed lines, for each case. Both δR and $\delta\theta$ were found to be almost double for the nano-sphere cases (triangles and circle) than for the platelets

(diamonds) for each "slip" event. CNTs case is not presented here as it exhibits no TL jump due to CCR evaporation.

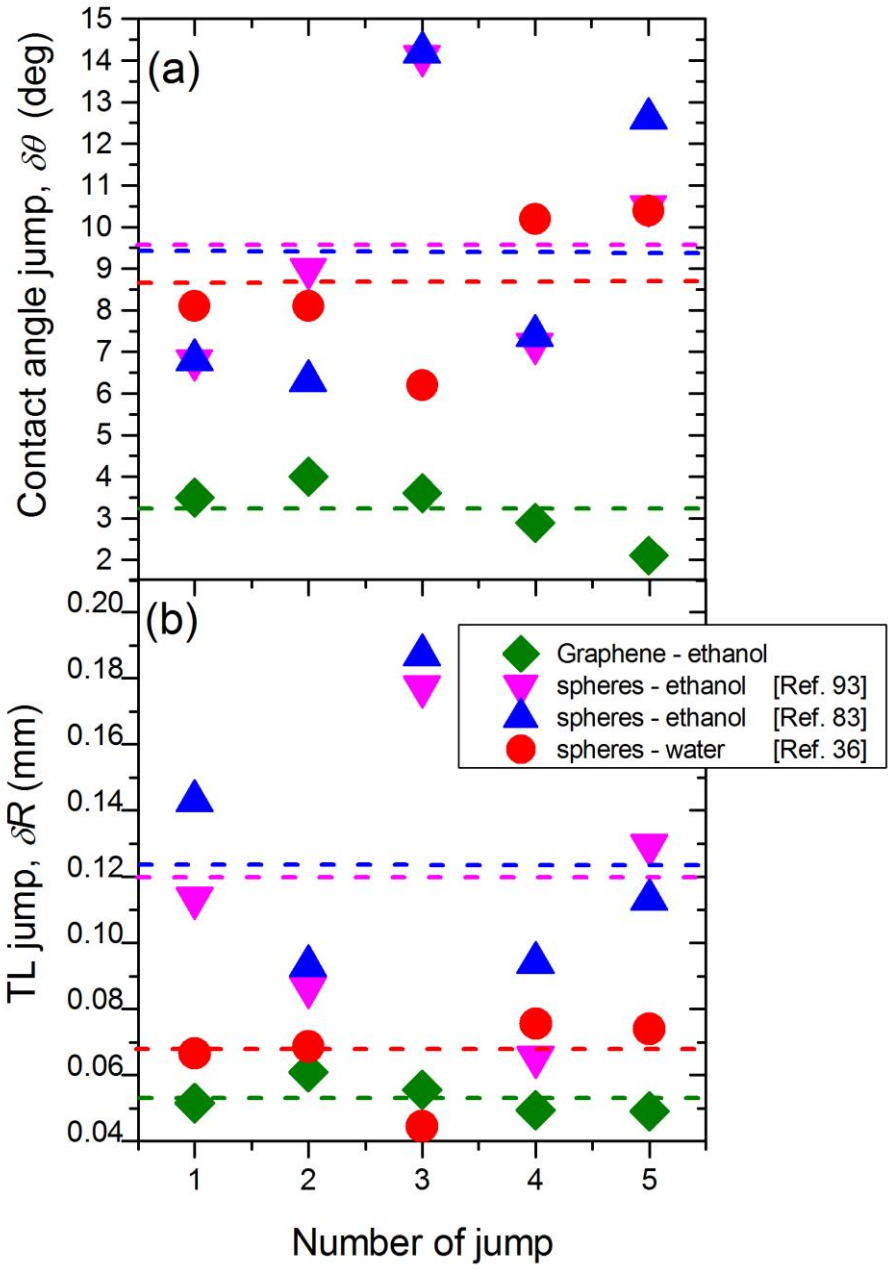

Figure 6.2: Change in (a) contact angle, $\delta\theta$, and (b) contact radius, δR, for the five first jumps in each "stick-slip" case presented in Figure 6.1. The average value for each case is shown with dashed lines.

In order to highlight the effect of particle geometry on TL motion kinetics, we plot in Figure 6.3 the change in contact angle, $\delta\theta$, versus drop size (normalised contact radius, R/R_0). No distinct pattern can be identified in the nano-sphere cases (all data sets except diamonds). $\delta\theta$ is (apparently) random, with values varying up to ~5^0, and jumps occuring for approximately 45 % of R_0 (or evaporation cycle). On the other hand, the behaviour of platelets appears to be more consistent with jumps occurring for ~ 35 % of R_0. $\delta\theta$ value fluctuates for ~2^o, roughly half that for nano-spheres. Additionally, as the droplet shrinks due to evaporation, the platelet droplet jumps (diamonds) appear to become smaller, contrary to any of the spherical cases. The smaller jumps should be indicative of both particle concentration at the TL and the hysteretic energy barrier, these two being directly linked [36]. Addition, the pinning barrier is directly related to the size of the ring [48]. Consequently, the graphene rings and hence the pinning barrier are expected to be the smallest in this comparison, to be shown later. We should also note here that the behaviour of the water-nanospheres suspension (circles) is slightly more consistent than the other two ethanol-nanospheres cases (triangles), possibly due to the different interactions between the solvent molecules and the substrate, leading to the relatively different evaporation kinetics [36].

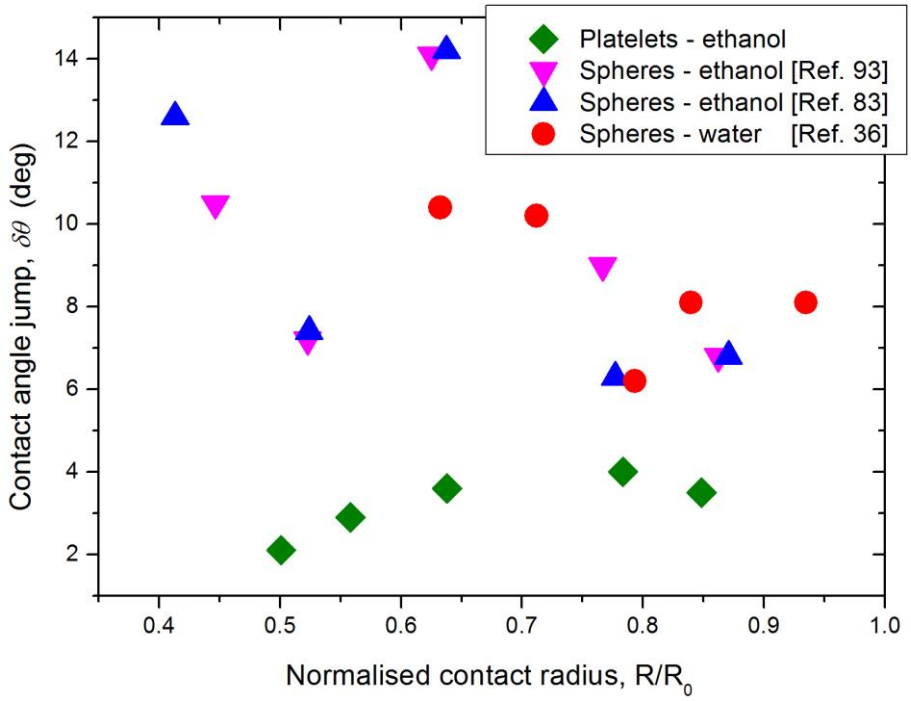

Figure 6.3: Change of contact angle, $\delta\theta$, plotted against droplet size (normalised contact radius, R/R_0), for droplets containing platelets (diamonds) and nanospheres (all rest data points) from Figure 6.2.

From the above, it is obvious that particle geometry has a significant impact on the droplet evaporation behaviour and δR and $\delta\theta$, especially when taking into consideration the CCR behaviour of the CNTs. As a result, it is only reasonable to assume that the magnitude of the hysteretic energy barrier, U, pinning the TL of each droplet is related to particle shape. As described in section 2.3, a pinned drying drop is out of thermodynamic equilibrium, with constant R and decreasing θ. Therefore, excess free energy per unit length, $\delta\bar{G}$, should accumulate. Upon θ reaching a critical value, $\delta\bar{G}$ should attain the value of the barrier, $\delta\bar{G} = U$, and hence TL should "slip". Since the values of both R and θ are available from the data in Figure 6.1, we can estimate the average $\delta\bar{G}$ required for de-pinning in each case, using equation 4.3. The

surface tension, γ, was measured using the pendant drop technique to be that of pure ethanol, *ca.* 0.024 N/m for the ethanol nanofluids and that of pure water, *ca.* 0.073 N/m for the aqueous suspensions.

From Equation (3.3), the excess free energy, per unit length of TL, $\delta\bar{G}$, can be calculated simply from $\delta\bar{G} = \delta G/2\pi R$. The resulting $\delta\bar{G}$ values were normalised with surface tension and plotted versus α in order to directly compare the effect of particle shape on the pinning of the TL for every system presented in Figure 6.1

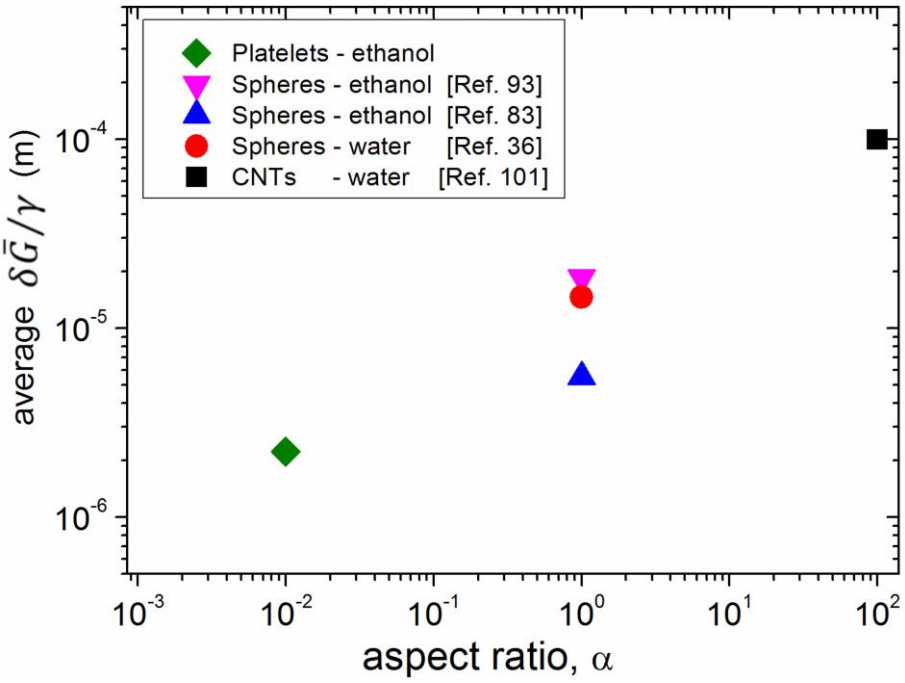

Figure 6.4: Effect of particle geometry on the excess free energy per unit length, $\delta\bar{G}$, accumulated in each system at the moment of the first jump. $\delta\bar{G}$ was calculated using the data in Figure 6.1 and normalised by surface tension of water, 0.073 N/m, for the aqueous solutions (square and circle points) and that of ethanol, 0.024 N/m, for the rest.

Figure 6.4 depicts $\delta\bar{G}/\gamma$ as a function of particle aspect ratio, *i.e.* geometry, and shows a proportional relationship between the two quantities. $\delta\bar{G}/\gamma$ ranges between $8.5 \times 10^{-7}\, m < \delta\bar{G}/\gamma < 1.0 \times 10^{-4}\, m$. In more detail, platelets, $\alpha \approx 0.01$, exhibit a de-pinning energy of $\delta\bar{G}/\gamma \approx 2.2 \times 10^{-6}\, m$. Nano-spheres, $\alpha \approx 1$, require an intermediate amount of energy, viz. $5.5 \times 10^{-6}\ m < \delta\bar{G}/\gamma < 1.8 \times 10^{-5}\, m$, depending on the solvent and hence the contact angle. In this comparison, the nanosphere solutions act as the intermidiate link between the ethanol based platelet fluids and the water based CNTs one. Since the CNTs ($\alpha \approx 100$) drops exhibit CCR evaporation, then they are expected to require the highest, in this comparison, amount of energy for de-pinning to occur. Indeed, as it can be seen in Figure 6.4, CNTs (squares) attain much higher energy $\delta\bar{G}/\gamma \approx 1.0 \times 10^{-4}\, m$. Although this energy is the highest in the system, however, it does not correspond to the first TL jump but to the highest attainable energy in the pinned system, just before drying, without the occurrence of any jump. We should note, that it is indicative of the high impact of the CNTs shape on TL pinning and also of the fact that the hysteretic energy barrier in this case should be higher and not attainable by the system in question (CCR).

6.3. Ring stain patterns

Optical micrographs of the resulting coffee-stain deposits left behind the evaporation of various nanofluids are shown in Figure 6.5, further highlighting the impact of particle shape on ring-stain formation. Since there were no ring-stain micrographs in Ref. [36], we include in the comparison in Figure 6.5 a typical ring-stain resulting from

the evaporation of a water based nano-sphere drop, which we have presented previously in chapter 4.1. A series of concentric rings with a preferential pinning to one side, typical of "stick-slip" evaporation, can be identified to have formed from droplets containing platelets (Figure 6.5 (a)) and nano-spheres (Figure 6.5 (b, c, d)), with the platelets rings being the least uniform and defined. Furthermore, the water based nanosuspension, (Figure 6.5 (d)) exhibits a relatively different pattern in which the rings are not uniform and some triangular structures have formed at the liquid front, extensively discussed in section 4.1. The single rings seen in Figure 6.5 (e) and (f, g) resulted after the complete drying of nL and μL droplets containing CNTs, typical of CCR evaporation. We should note here that the deposit in Figure 6.5 (f) is wider, attributable to the multi-walled nano-tubes, MWNTs being less flexible than single-walled nano-tubes, SWNTs (Figure 6.5 (g)) [100]. In another contribution, the addition of slightly irregular ellipsoids, $\alpha = 2.5, 3.5$, to an evaporating drop was reported to result in suppression of the coffee-stain effect due to particle assembly at the air-liquid interface which, in turn, acted as nucleation sites, thus effectively hindering the outward fluid flow and at the same time distorting the line shape. However, when surfactant (sodium dodecyl sulfate, SDS) was added to the system, it restored the coffee-stain formation mechanism [94]. Consequently, we can assume that the CNTs in Figure 6.5 (e-g) can pin the TL as either surfactant was added to their solutions or they have been functionalised in order to stabilise them [100-104, 135]. On the contrary, the other highly irregular case in this comparison, platelets, were pristine and no surfactant was used, yet "stick-slip" occurred. At this point we could surmise the following tentative description for the ring-stain formation in this case: The graphene

platelets within the flow tend to “tumble”, similar to what has been reported for other kind of platelets in flows in a series of cases [136-139]. “Tumbling” should be capable of retarding the inter-particle attraction forces reported in Ref. [94], leading to TL pinning; the most important component in the coffee-stain formation mechanism. Nonetheless, random particle aggregates can be identified to have deposited in the areas between the rings, attributable to the “tumbling” retarding the inter-particle attraction forces only to some extent. A similar pattern has been reported when a droplet evaporated in the confined geometry of a sphere on flat system [140].

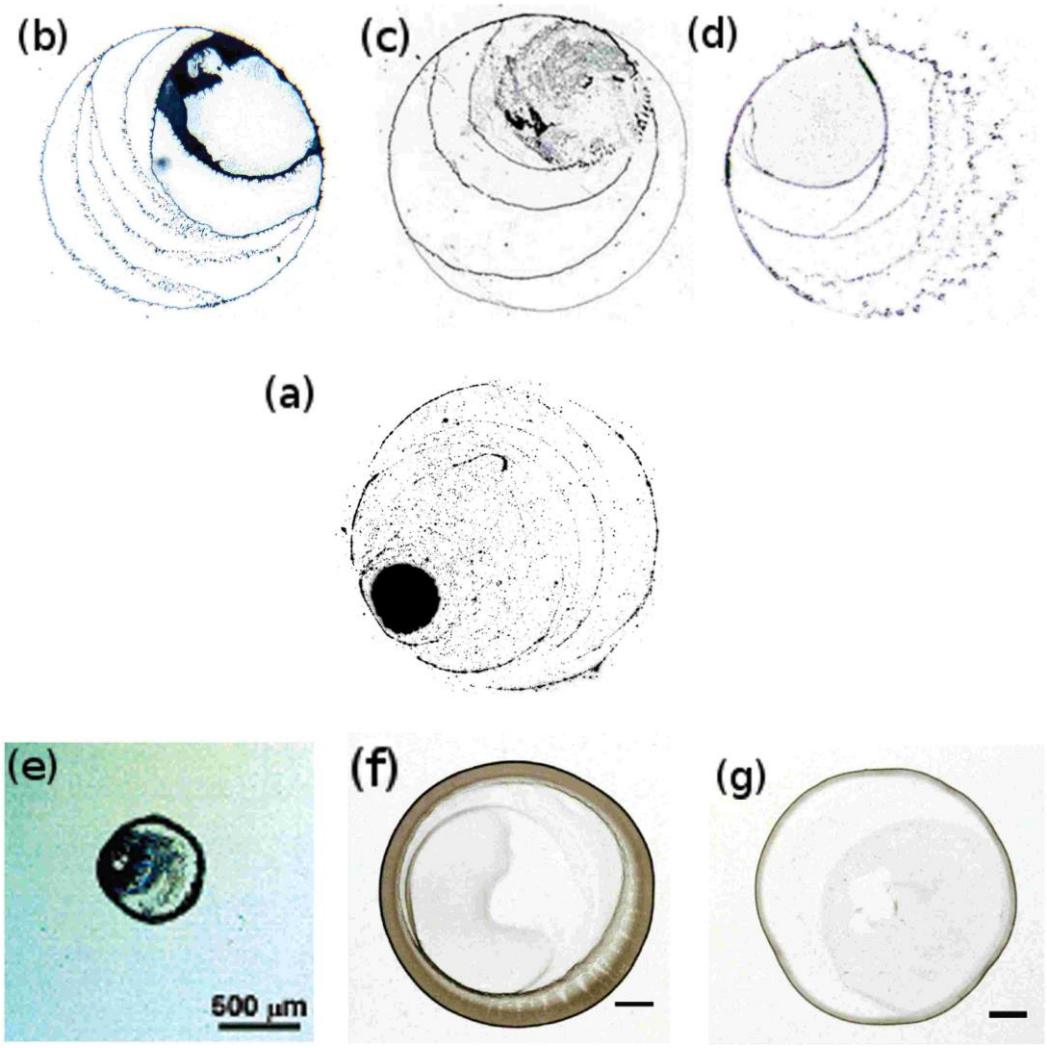

Figure 6.5: Optical micrographs of the resulting ring-stains after the complete evaporation of a droplet of (a) ethanol containing 0.1% w/v graphene platelets on a PTFE substrate, (b, c) ethanol containing 0.1 % w/v TiO_2 nano-spheres on a PTFE substrate [83, 93], (d) water containing 0.125 % w/v SiO_2 nano-spheres on a silicon substrate [47], (e) water containing 0.25% w/v SWNTs on an OTS-treated silicon substrate [101], (f, g) water on glass substrates containing 0.04 and 0.02 % w/v MWNTs and SWNTs respectively [100]. Deposits in (a) – (d) are of same diameter ~3 mm and the bars in (f, g) indicate 1 mm.

6.4. Particle deposition and self-assembly mechanism

In this section, we focus our attention on the structuring behaviour of each particle shape. Spheres show the tendency to form sequential close-packed, hexagonal and square regions in their attempt to achieve the most efficient packing in the limiting space of a meniscus [43-46], (discussed in detail in section 4.3). However, disordered regions at either side of the ring-stains have been reported in a number of systems [47-49]. From the above, the two main ordering factors during the particle self-assembly process in coffee-stains become readily apparent: wedge constraints and fluid flow velocity, the two being directly linked each other.

As described in section 2.5, the highly irregular CNTs have the tendency to orient themselves parallel to the drop periphery, due to wedge constraints. Moving towards the interior, the wedge constraints become weaker which in combination with the enhanced, due to pinning, outward capillary flow, result in a transition region. In this region some particles oriented themselves to the flow and some parallel to the TL. Further away from the TL, the wedge constraints become very weak or even negligible, thus the CNTs can orient themselves to the outward flow [100-102]. These different particle orientations further corroborate the impact of wedge constraints and fluid velocity on the particle self-assembly behaviour at a three-phase line.

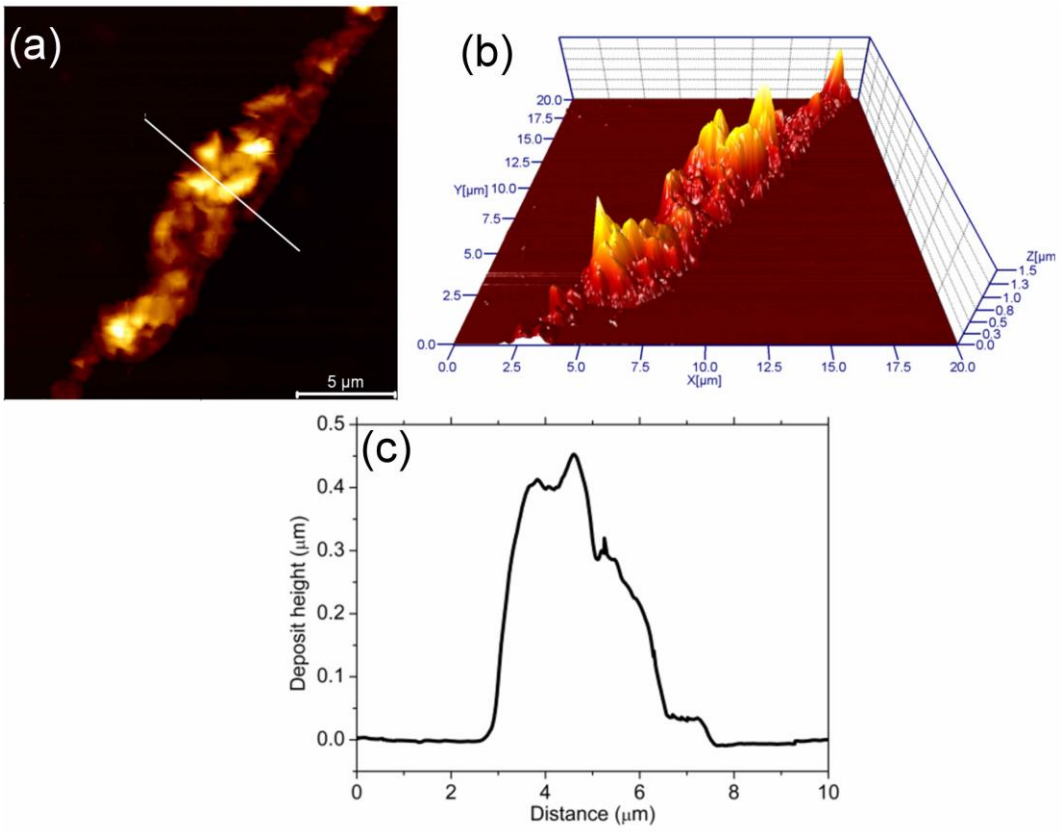

Figure 6.6: (a) Characteristic AFM topography image and (b) corresponding 3-D representation of the resulting coffee-stain after free evaporation of 0.1 % wt. graphene-ethanol drop. (c) Average height profile obtained from a series of profiles taken perpendicular to the TL, an example one is shown in (a). Drop centre lies to bottom-right corner in all images.

In order to assess whether fluid velocity and wedge constraints are significant for the self-assembly behaviour of graphene platelets, we experimentally probed graphene rings with AFM and SEM. Figure 6.6 depicts a typical topography image (a) and the corresponding 3D representation (b) of an area of the graphene ring. In this image a continuous but rather irregular, in shape, deposit with a slightly gentler slope to the exterior can be seen. The average height profile, Figure 6.6 (c), depicts the exact shape and size of the deposit, along with the rest of the features such as the gentle exterior

slope and the sharper interior. This height profile was calculated from a series of profiles perpendicular to the ring-stain, an exemplary one is presented with a white line in Figure 6.6 (a). These deposits are the smallest in this comparison. Since TL deposits generally act as "artificial" defects pinning the contact line [78, 93], we can further explain the variety of $\delta\overline{G}$ values presented in Figure 6.4.

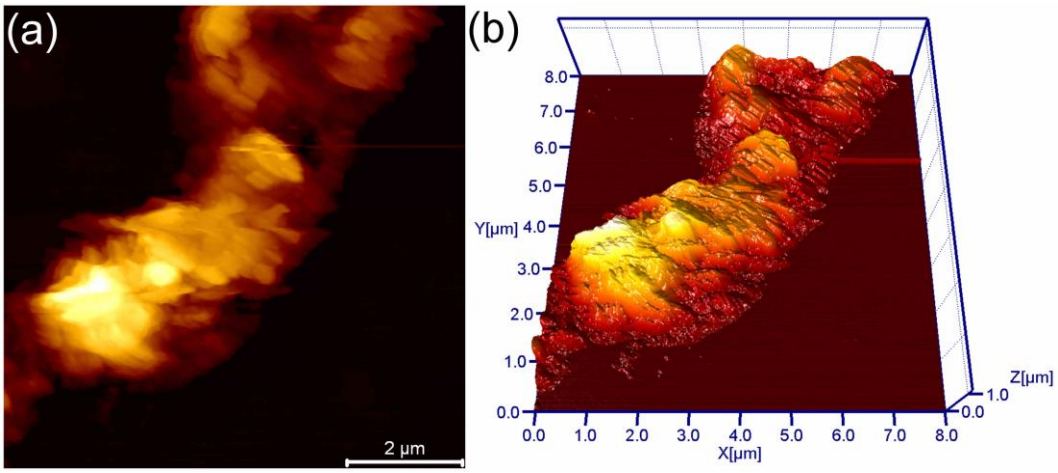

Figure 6.7: (a) Nano-structuring of graphene deposit (0.1% wt.) presented in Figure 6.7. (b) 3-D representation of the same area.

A magnification of the graphene ring, Figure 6.7, shows further information about the self-assembly behaviour of the platelets at the TL. Although, the deposit remains irregular in shape, some valleys and humps can be distinguished on the ring. Additionally, some striations (especially clear in Figure 6.7 (b)) can be identified in some of parts of the ring, which are perpendicular both to the TL and the substrate. These striations do not appear to follow the scanning direction of the AFM probe, therefore the possibility of their being tip artefacts can be excluded.

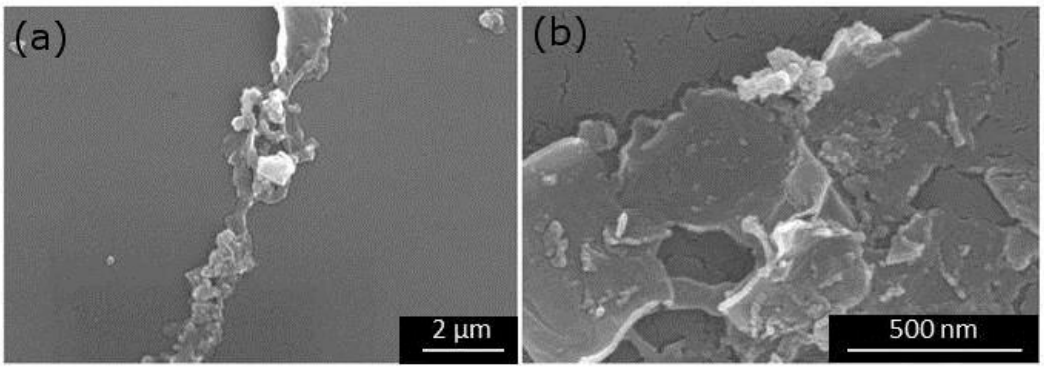

Figure 6.8: (a) SEM micrograph of 0.1 % wt. ring-stain and (b) close-up showing nano-structuring of the same ring.

The effect of fluid velocity and wedge constraints on the self-assembly behaviour of graphene platelets was further examined with SEM. In Figure 6.8 (a), it is readily apparent that graphene platelets can bend which results in random folding which in turn results into irregularly-shaped deposits. In Figure 6.8 (b), some platelets can be seen to have deposited themselves perpendicular to the substrate, as explained above. This image further supports our nano-structuring findings, shown in Figure 6.7 and should allow us to draw some useful conclusions about the self-assembly behaviour of graphene platelets.

Combining these nano-scale findings with the macro-scale ones presented above, we could determine how platelets self-assemble at the TL. During each "stick" event the platelets are carried to the TL due to the induced outward fluid flow [19]. As fluid flow velocity increases greatly near the TL [47, 49, 128, 141], the platelets should attain enough kinetic energy in order to overcome the wedge constraints, *i.e.* disjoining

pressure. Furthermore, the platelets should "tumble" within the flow due to their highly irregular shape and flexibility [138, 139]. Therefore, they should feel weaker inter-particle attractions, as the ones reported in Ref. [94]. The "tumbling" should also result in platelets depositing at the TL under random angles, which, considering their high bending, should lead to some of the platelets orienting perpendicular to the substrate. As the space at the TL is rather limited, the platelets arriving next should orient themselves in a similar fashion hence giving rise to the observed striations. As the ring continues to grow, some of the humps or valleys seen in Figure 6.7 were formed, possibly due to graphene folding. Eventually, the TL will jump to a new position essentially "freezing" the structures and making the interior slope sharper.

6.5. Conclusions

Particle shape was found to be an important parameter affecting the TL motion kinetics of evaporating sessile, nanofluid droplets. A wide variety of particle shapes categorised according to aspect ratio, $0.01 < \alpha < 100$, were examined. Graphene platelets, which was the system that was investigated experimentally in this chapter, corresponds to the smallest α. Nano-spheres were the intermediate case, $\alpha \approx 1$ and the other extreme case was that of CNTs, $\alpha \approx 100$. Nano-spheres exhibited typical "stick-slip" evaporation behaviour, whereas platelets presented a unique behaviour resembling "stick-slip" and CNTs droplets evaporated under the CCR regime. TL motion kinetics of the "stick-slip" cases were assessed in terms of change in contact angle, $\delta\theta$, and radius, δR. Furthermore, $\delta\theta$ was plotted versus normalised contact

radius, R/R_0, and showed erratic behaviour for the nano-spheres and rather consistent for the platelets. The hysteretic energy barrier at the time of the first jump of each case, including CNTs, was calculated and plotted against the particle aspect ratio. This unveiled a proportional relationship between the two quantities. Nano-scale information further supported this finding. Extensive comparison of nanoscale information for each case allowed us to establish a particle deposition and self-assembly mechanism consisting of mainly two factors: fluid flow velocity and wedge constraints. Each extreme particle shape adapted differently to these two factors, with platelets "tumbling" and folding and CNTs forced to align to them.

Chapter 7 On particle flexibility and evaporation process and crystallinity

In this chapter, we attempt to illustrate the relationship between particle flexibility and the underlying mechanisms of coffee-stain formation and particle deposition in the resulting patterns. As a model for particle rigidity, we chose DNA molecules as its size resemble those of nanoparticles. Two different DNA strands were used, a rigid and a flexible, rigid being shorter than the persistence length of the molecule and flexible being longer. Additionally, EDTA was added in some of the suspensions, as it is typically used in DNA solutions to collate any cation traces in the solution, thus hindering damages to the DNA chains. The effect of particle flexibility on the evaporation process was first probed. Rigid particles, in the presence of EDTA, were found to promote CCR, whereas all the other cases (short in the presence of EDTA and long both with and without EDTA) led to a three stage process. Resulting patterns varied widely, from thin ring-stains with different particle deposition patterns mainly at their interiors to predominantly single thick ring deposits, owing to particle flexibility. This behaviour was attributed to a combination of increased DNA rigidity due to EDTA anions and a preference of EDTA to deposit at the centre of the drop, hence interfering with DNA mobility. Consequently, we quantified the hysteretic energy barrier which was found to be inversely proportional to particle length. Lastly, AFM was employed as a means to determine any nanoscopic feature within the resulting ring-stains. Notably, the pure DNA stains revealed different crystallisation process depending on particle flexibility.

7.1. Evaporative behaviour and resulting ring-stains

In order to investigate the effect of particle length and hence flexibility on droplet evaporation behaviour, deposit build-up and solute self-assembly within it, a series of free evaporation experiments were conducted using DNA suspensions. DNA was chosen for this study due to its dimensions being comparable to the nanoparticles discussed in previous chapters, diameters of relevant order of magnitude of a few nm. Additionally, a DNA molecule is considered to be cylindrical in shape with a diameter of approx. 2 nm and varying in length [111, 142]. In this work, a short and a long DNA strand were selected, with chain lengths of approx. 100 and 1000 base pairs (bp) or 34 and 340 nm respectively. Base pairs are essentially nucleotide pairs; the building blocks of DNA, with typical size approx. 3.4 Å [111, 142]. Moreover, the length of the DNA molecule should indicate its flexibility. Effectively a DNA molecule can also be regarded as a polymer with bp acting as the monomer units. Therefore, borrowing from polymer principles, the length below which DNA can be considered rigid is called persistence length and is approx. 150 bp or 50 nm [112-114]. Therefore, the two chosen strands can be classified as stiff/rigid, 100 bp, and soft/flexible, 1000 bp.

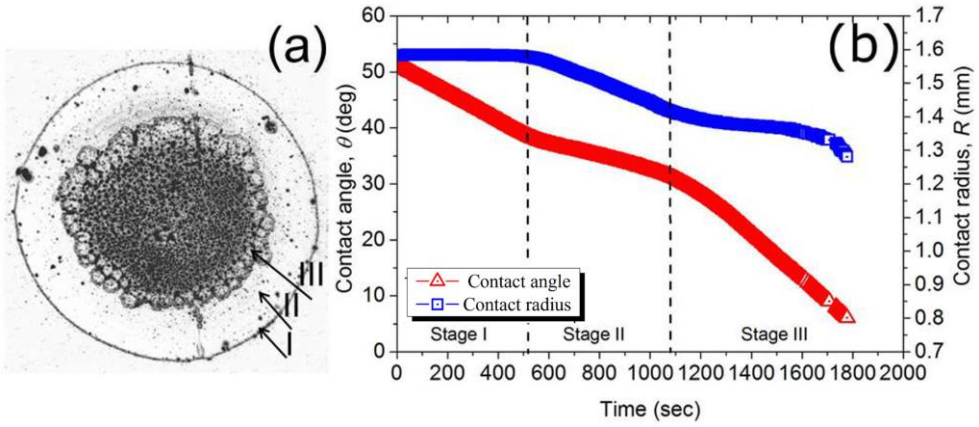

Figure 7.1 (a) Optical micrograph of the ring-stain deposit left behind the free evaporation of a 3μl, 1mM EDTA, aqueous droplet (b) Contact angle (triangles) and radius (squares) evolution over time of the droplet. Arrows correlate each pattern feature with their corresponding evaporation stage.

Prior to examining the effect of the two different DNA strands on the coffee-stain formation mechanism, we investigated the behaviour of the base fluid, deionised water containing 1mM EDTA. EDTA is a substance commonly added to DNA solutions in order to protect them from degrading [143]. EDTA contains four separate carboxyl (–COOH) side-groups, allowing it to collate metal cations, a process called chelation. Deionised water may contain traces of such metal cations, typically Mg^{2+} and Ca^{2+}, which could potentially damage the DNA molecules [143].

The evaporation behaviour and the resulting pattern of the base fluid are presented in Figure 7.1. These results should act as the basis to understand and interpret the more complex system of droplets containing EDTA and DNA molecules. Initially, in stage I, the droplet evaporates under the CCR mode. Possibly the thin ring-stain formed during this stage due to the induced outward flow [19]. Once the contact angle reaches

a sufficiently small value, $\theta = \theta_r$ (see sections 2.3 and 2.4), the evaporation enters stage II. During this stage, both θ and R diminish simultaneously, resulting in the area with sparse solute accumulation (arrow II in Figure 7.1 (a)). Diminishing volume leads to increasing viscosity, locally, which, in turn, should result in a second and final CCR regime observed in stage III. During this stage, the majority of the solute, which is still suspended in the solution, is deposited on the surface in the pattern denoted by arrow III in Figure 7.1 (a).

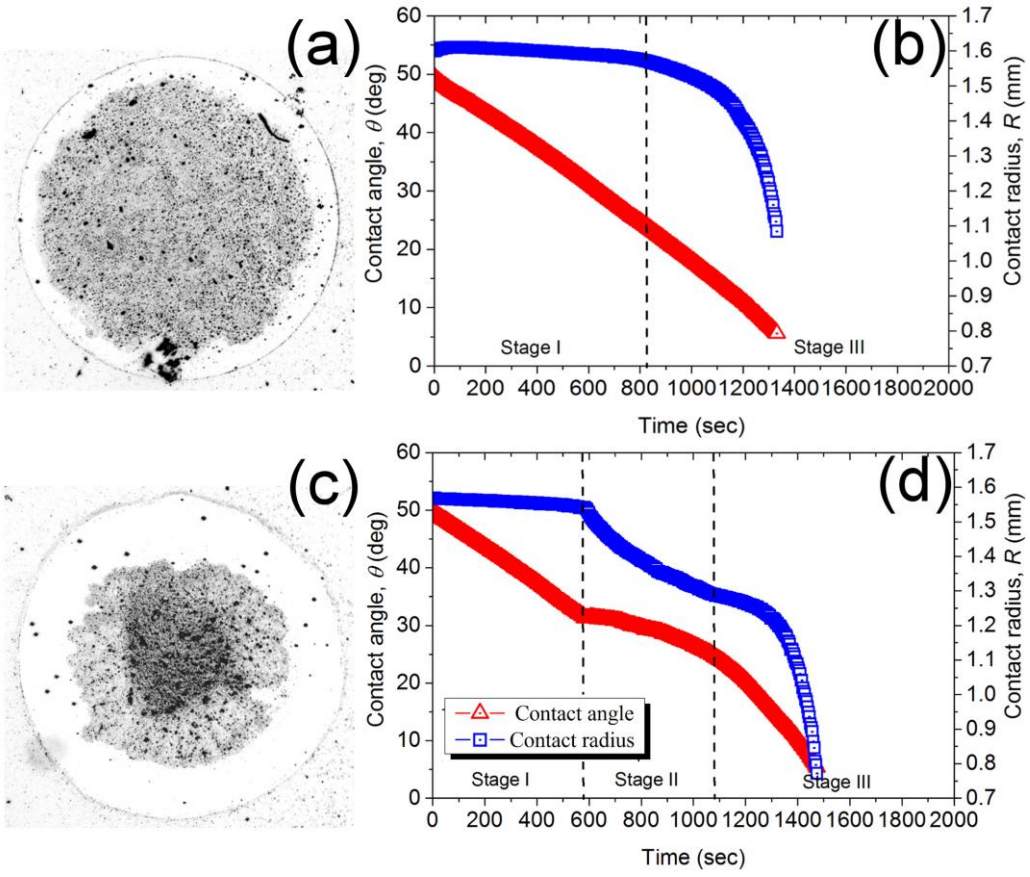

Figure 7.2 (a) Optical micrographs of the ring-stain deposits left behind the free evaporation of a 3μl, 1mM EDTA, aqueous droplet containing 0.01 % w/v (a) 100 bp and (c) 1000 bp DNA molecules. Corresponding contact angle (triangles) and

radius (squares) evolution over time of droplet containing (b) 100 bp and (d) 1000 bp DNA strands.

Figure 7.2 depicts the resulting pattern and the evaporation profile of droplets containing DNA strands of 100 bp (top row) and 1000 bp (bottom row). Short and rigid DNA molecules led to CCR evaporation Figure 7.2 (b). In the resulting pattern (Figure 7.2(a)), a thin ring-stain is readily apparent, attributable to the initial TL pinning (stage I). The resulting coffee-ring is too small to support the CCR evaporation profile. However, as it has been described in Chapter 6, rod-like particles are capable of pinning the TL of droplets strongly. In this case, perhaps, the rod-like DNA strands at the periphery of the droplet pinned the TL directly after deposition. In turn, this pinning induced an outward flow depositing the adjacent DNA particles to the TL. Nonetheless, as it was shown in Figure 7.1, EDTA tends to deposit at the centre of initial droplet, therefore it is hindering, to some extent, the outward mobility of DNA strands in the bulk. Hence, most of the particulate is deposited in the uniform area at the centre of the pattern (Figure 7.2(a)).

On the other hand, Figure 7.2(d) shows that longer and hence flexible DNA molecules, 1000 bp, followed the evaporation behaviour of the base fluid (water with EDTA, presented above). The resulting pattern (Figure 7.2(c)) also resembles that of the base fluid (Figure 7.1(a)). Compared to the base fluid, the transition from stage I to II is more distinct and sharp and TL retraction in stage III is more rapid. This rapid motion of the TL should result in the higher solute accumulation at the centre of the pattern, darker area. Furthermore, θ and R diminish in a concave and a convex fashion

respectively. From these results, we can surmise that EDTA is interfering with the coffee-stain formation mechanism, as it hinders DNA convection to the periphery. The above evaporative behaviours are consistent with what has been reported in the literature for much longer DNA chains, length of 48.5 kbp or ~ 16.500 μm [144] or when drop drying technique was employed in order to produce DNA microarrays [145].

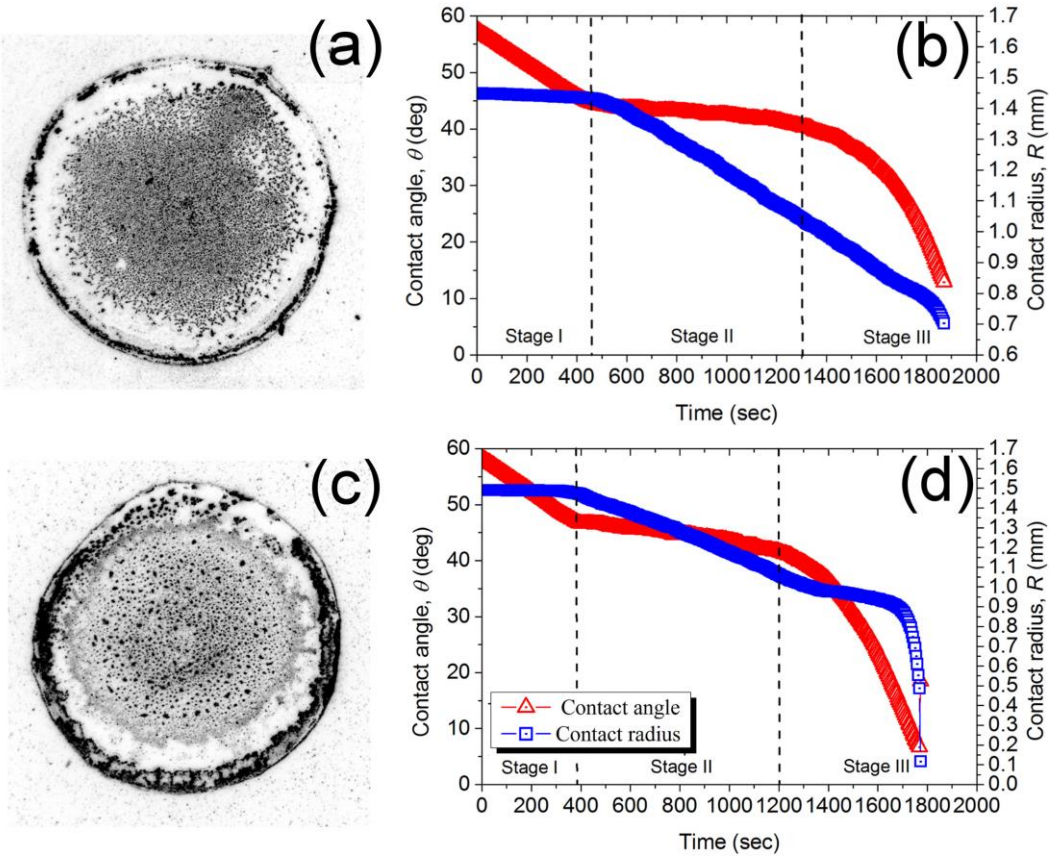

Figure 7.3 (a) Optical micrographs of the ring-stain deposits left behind the free evaporation of a 3μl, without EDTA, aqueous droplet containing 0.01 % w/v (a) 100 bp and (c) 1000 bp DNA molecules. Corresponding contact angle (triangles) and radius (squares) evolution over time of droplet containing (b) 100 bp and (d) 1000 bp DNA strands.

As it became evident, using EDTA in the base fluid does not allow us to determine the exact evaporative behaviour of DNA strands with varying length/flexibility. Therefore, in the second part of this study, droplet evaporation experiments were repeated in the absence of EDTA. Results for the evaporation behaviour and resulting deposit patterns of the 100 and 1000 bp cases are presented in Figure 7.3 top and bottom row respectively. In both cases, an initial pinning occurred which then transitioned into a simultaneously decreasing $\boldsymbol{\theta}$ and $\boldsymbol{R}$ mode. However, some differences can be readily discerned in stage III. In the 100 bp case (Figure 7.3 (b)), when the evaporation enters stage III, the TL retracts continuously until full evaporation, whereas for the longer 1000 bp DNA molecules (Figure 7.3 (d)), evaporation enters a second CCR mode leading to full evaporation. In both of the resulting patterns a distinct, uniform ring deposit can be identified (Figure 7.3 (a) and (c) for 100 and 1000 bp respectively). Notably, in the 100 bp case some particulate has also deposited uniformly within the droplet, following the behaviour of 100 bp with EDTA case (Figure 7.2 (a)). In the flexible strands case, 1000 bp, a wider ring-stain formed with a second inner ring and some solute coverage within. In both cases, the ring-stain should have formed during the initial CCR event in stage I. Similar DNA coffee-rings have also been reported in the past [113].

Considering the results for the samples with and without EDTA (Figure 1.2 and Figure 1.3 respectively) we could surmise the following explanation for the observed evaporative behaviour: Generally, DNA strands tend to form coffee-stains as exhibited

in both pure DNA cases in Figure 7.3 (a) and (c) and as reported elsewhere for much longer strands [113]. In the presence of EDTA, the stiff character of the 100 bp strands is enhanced by the presence of the dissolved EDTA anions. This surplus of anions increases the repulsion between the already negatively charged DNA chains, due to the phosphate backbone [146, 147], which in turn promotes their rigid rod-like behaviour. This leads to CCR evaporation, similar to CNTs [148]. On the other hand, the 1000 bp chains are, apparently, sufficiently long in order to overcome this limitation and possibly adopt a different conformation within the bulk (random walk model), hinting on a length-flexibility limit. However, none of these two cases exhibits a clear coffee-ring as EDTA is interfering with DNA mobility. This argument merits to be further probed by experimenting with a wider variety of DNA molecule lengths.

7.2. Triple line motion kinetics

In an attempt to elucidate the effect of particle flexibility on the coffee-ring formation mechanism, we quantify the excess free energy per unit length accumulated in each DNA system during the evaporation process using Equation 4.2.

Results are plotted in Figure 7.4 for DNA systems in the presence (left) and absence of EDTA (right). The presence of EDTA leads to higher $\boldsymbol{\delta\overline{G}}$ accumulation. This further supports our argument that in the presence of surplus EDTA anions, DNA strands become more rigid, and hence pin the drop stronger. In the rigid case, 100 bp,

depinning never occurs and $\boldsymbol{\delta\bar{G}}$ increases until full evaporation attaining a maximum value of $\boldsymbol{\delta\bar{G}} \approx \mathbf{9.83} \times \mathbf{10^{-6}}$ N. On the other hand, in the flexible case, 1000 bp, a jump occurs when $\boldsymbol{\delta\bar{G}} \approx \mathbf{1.83} \times \mathbf{10^{-6}}$ N. After the jump, $\boldsymbol{\delta\bar{G}}$ exhibits a small plateau and then increases exponentially again. The sharp decrease of $\boldsymbol{\delta\bar{G}}$ at the end of the evaporation cycle could be attributed to uncertainties in measuring $\boldsymbol{\theta}$ and $\boldsymbol{R}$.

Focusing our attention to the pure DNA systems, Figure 7.4 (right), we see that $\boldsymbol{\delta\bar{G}}$ follows a similar trend. The energy requirement for the initial depinning to occur decreases from $\boldsymbol{\delta\bar{G}} \approx \mathbf{9.56} \times \mathbf{10^{-7}}\ \boldsymbol{N}$ to $\boldsymbol{\delta\bar{G}} \approx \mathbf{7.32} \times \mathbf{10^{-7}}\ \boldsymbol{N}$ with increasing length/flexibility from 100 to 1000 bp respectively. Presumably, the effect of particle flexibility on the coffee-stain formation mechanism can be related to aspect ratio. As shown in Chapter 6, the smaller the aspect ratio the lower the energy demand for a jump, if any (CCR), to occur. Similarly, increasing particle stiffness leads to higher hysteric energy barrier pinning the TL. Noteworthy, flexible DNA require a smaller amount of energy for depinning to occur than the graphene requirement, $\boldsymbol{\delta\bar{G}} \approx \mathbf{2.0} \times \mathbf{10^{-6}}\ \boldsymbol{N}$.

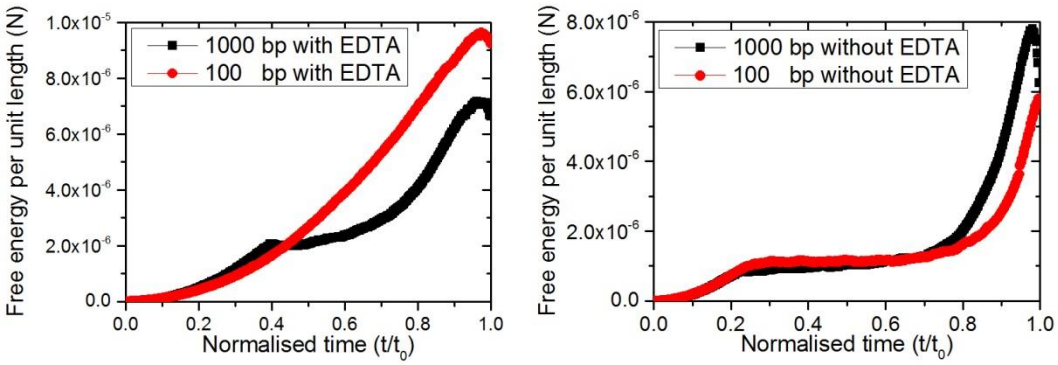

Figure 7.4: Comparison of free energy per unit length, $\delta\overline{G}$, evolution for DNA cases in the presence (left) and absence of EDTA (right).

7.3. Self-assembly mechanism

In this section, we present our findings on particle nanostructuring for solutions of pure EDTA, pure DNA and mixtures of the two. As described in Chapter 4 and Chapter 5, particles exhibit interesting nanostructuring features at the TL, therefore it is the first

point of focus for each case. Additionally, we present the structuring behaviour of particles in the interior of the droplets.

7.3.1. Self-assembly of EDTA solutions

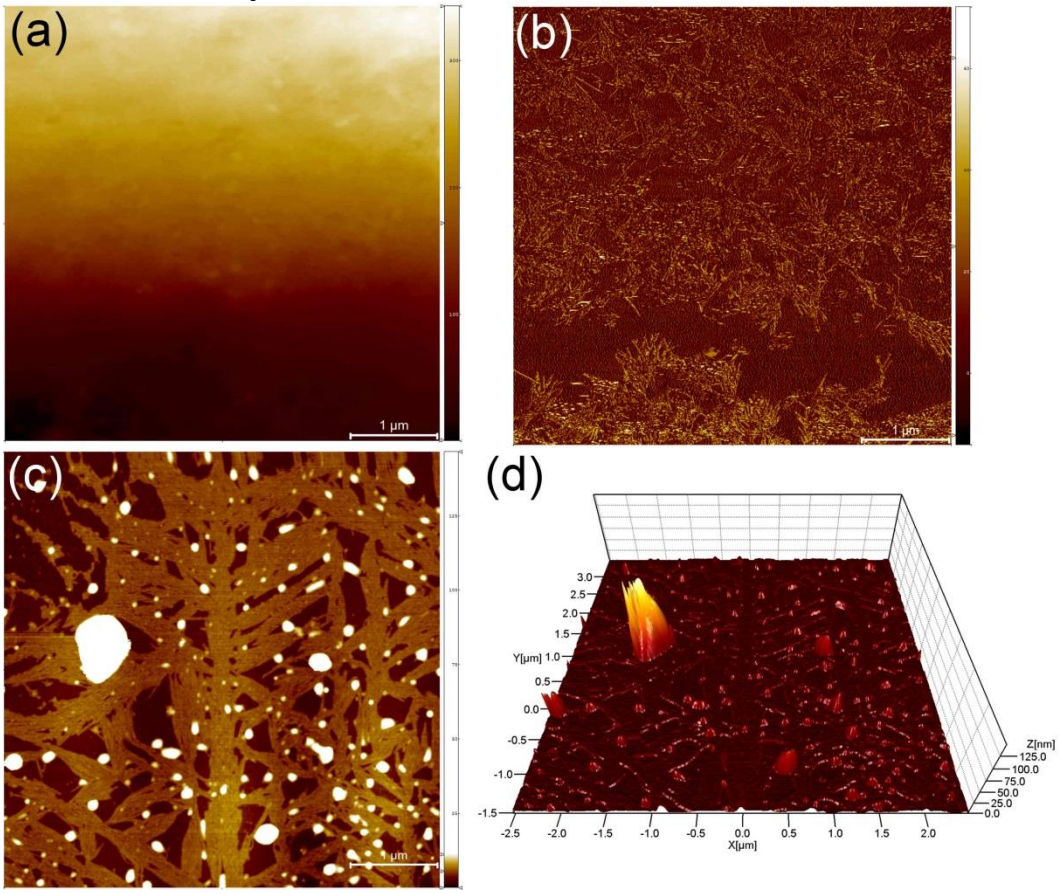

Figure 7.5: (a) 10 × 10 µm^2 topography image of the edge of the deposit (TL) left behind the evaporation of a 1mM EDTA aqueous droplet (b) Phase image of same area, scale bar is in degrees. (c) 5 × 5 µm^2 topography image of the central area of the resulting pattern of same samples. (d) 3-D representation of same area.

As the base suspension used in this study was 1mM EDTA in water, we first probed with AFM the self-assembly behaviour of EDTA within the resulting deposit. In more detail, at the edge of the deposit EDTA formed a small ring without any significant topographical features, seen in Figure 7.5 (a). However, some fibril structures are

readily apparent in the phase image (Figure 7.5 (b)), which is basically measuring topometric and compositional variations on the sample surface [149]. This type of imaging is commonly used in DNA measurements [24, 150, 151]. Notably, fibrils can be seen at the exterior of the ring-stain (bottom part of Figure 7.5 (b)). The deposition of these structures on the exterior side of the deposit is indicative of dewetting or TL retraction occurring directly after droplet deposition. As there is no direct evidence of radius retraction in the evaporation evolution, presented in Figure 7.1 (b), we can stipulate that this dewetting event is below the resolution of the camera of the instrument. More specifically, dewetting probably occurs almost instantaneously and, at the same time, the TL travels very small distances (in the order of a few microns). In Figure 7.5 (c) and (d), the topography and the corresponding three dimensional representation of an area at the interior of the deposit show a thin fibril network covering most of the sample surface. On top of this network some solute islands, possibly EDTA aggregates, can also be identified as bright spots.

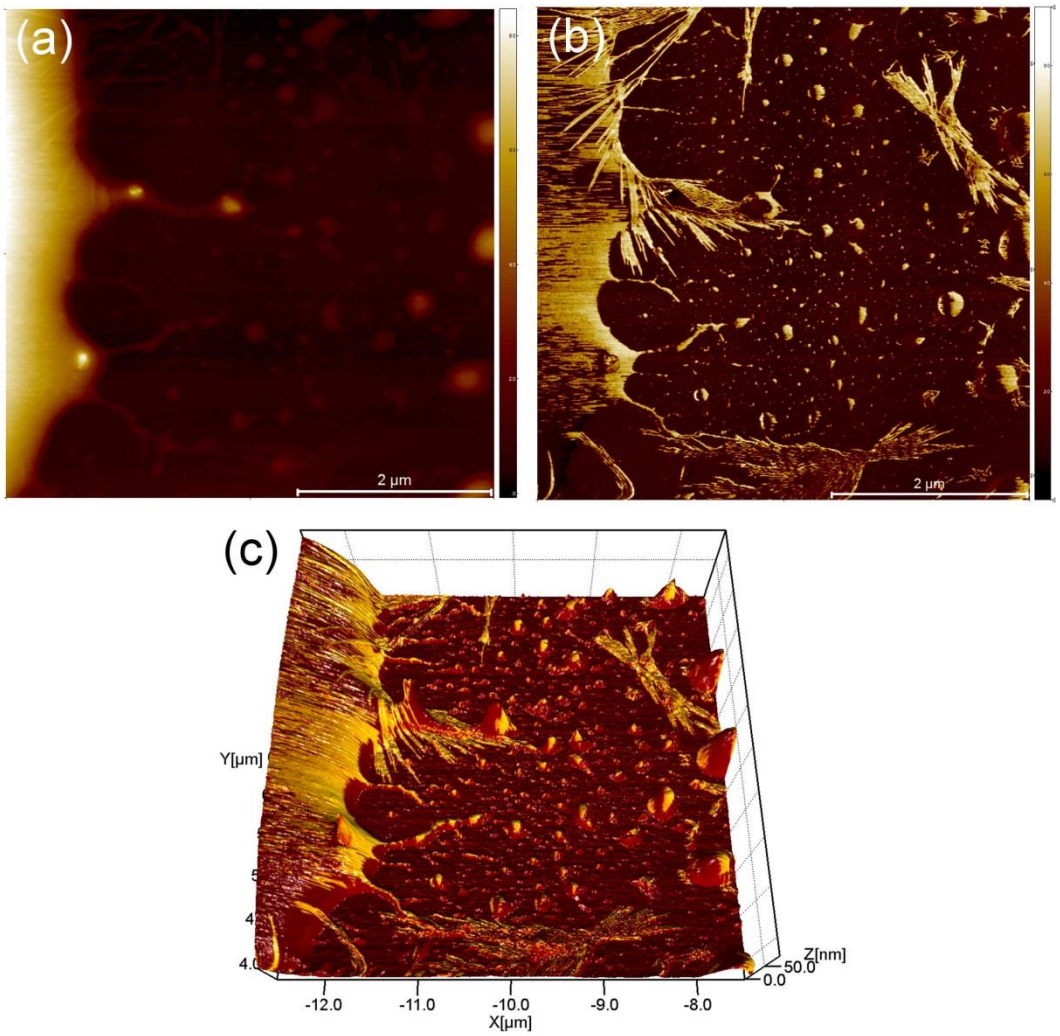

Figure 7.6: (a) 5 × 5 µm^2 topography image of the edge of the deposit (TL) left behind the evaporation of an aqueous droplet containing 0.01 % w/v of 1000 bp DNA strands with EDTA. (b) 3-D representation of same area. (c) 3-D representation combining information from both (a) and (b). Droplet interior lies to the left of each image.

Having established the nanostructuring of EDTA, we then focused our attention on the self-assembly behaviour of the two DNA strands within the same base solution. In Figure 7.6, we present the 1000 bp with EDTA behaviour at the TL of the droplet. More specifically, in the topography image in Figure 7.6 (a), the beginning of the

coffee-stain can be readily identified as the brighter area at the left side of the image. At the exterior, some particulate islands forming away from the droplet can also been seen. Some fibrils can be identified in the phase image in Figure 7.6 (b) and some horizontal striations attributed to tip artefacts. Both topographic and phase features have been combined in Figure 7.6 (c), which allows better observation of the results. Similar structures were found in the 100 bp with EDTA case without any remarkable differences and were therefore omitted. Considering the fact that EDTA exhibit a self-assembly behaviour of fibrils, we cannot differentiate between the DNA and EDTA in these images. Therefore, it is evident that we need to focus our attention on the pure DNA samples in order to understand how DNA strands self-assemble within the resulting patterns.

7.3.2. Self-assembly of pure DNA solutions

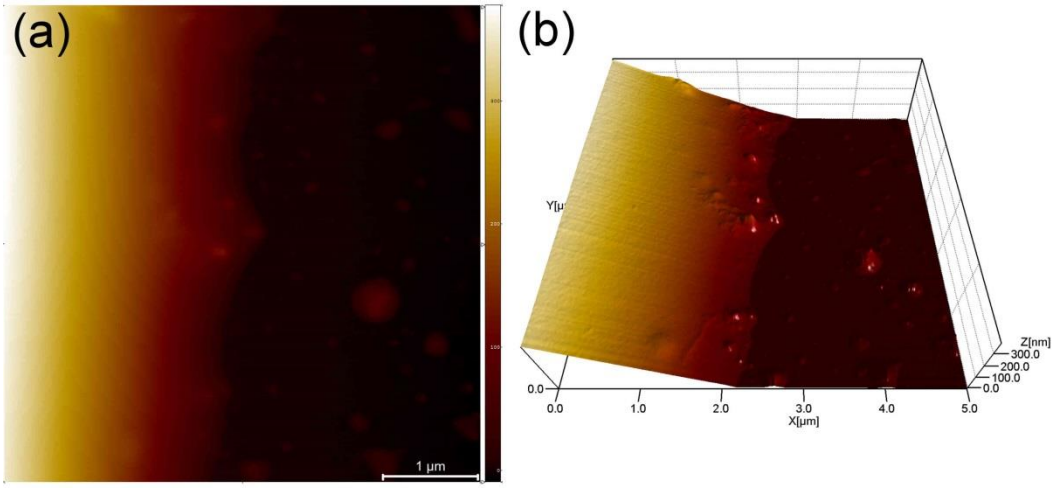

Figure 7.7: (a) 5 × 5 µm^2 topography image of the edge of the deposit (TL) left behind the evaporation of an aqueous droplet containing 0.01 % w/v 100 bp DNA strands *without* EDTA. (b) 3-D representation of same area. Droplet centre lies to the left of each image.

Figure 7.7 (a) depicts the topography of the exterior edge of the coffee-ring left behind the free evaporation of droplets containing 100 bp DNA strands without EDTA. In the 3-D representation of the same area (Figure 7.7 (b)) the actual shape of the ring deposit and various other features can be distinguished more clearly. The ring does not exhibit any particular structuring characteristics. Additionally, the slope increases rather sharply and some larger particle aggregates can be seen at the edge of the ring-stain, acting possibly as TL anchoring points. Outside the ring (right side of both images), a series of spherical particle islands can be identified, attributable to an initial dewetting (as discussed above). The phase image of this area did not reveal any particular particle features and was therefore omitted.

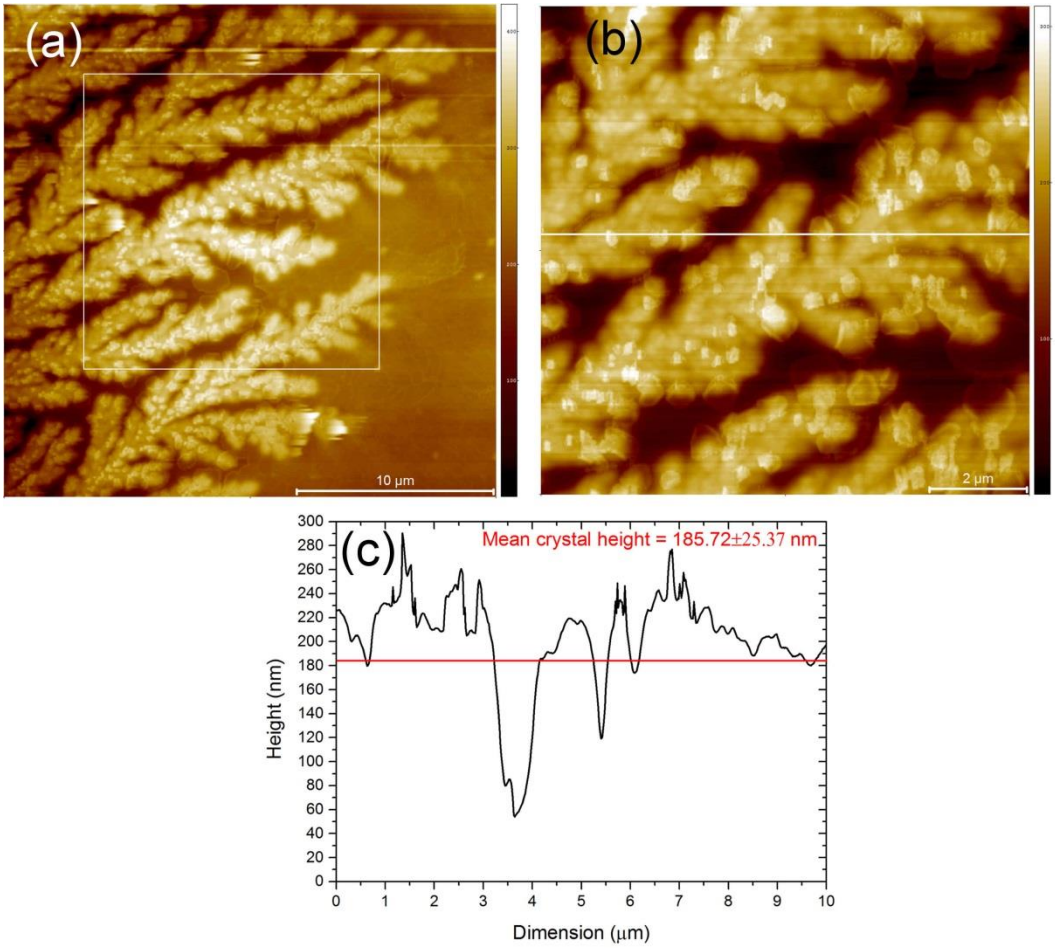

Figure 7.8: (a) 10.0 × 10.0 µm^2 topography image of the central area of the resulting pattern of the 0.01 % w/v of 100 bp *without* EDTA sample. (b) 5 × 5 µm^2 magnification of the area in the box in (a). (c) Mean height profile corresponding to line in (b). Droplet centre lies to the left of the images.

Notably, Figure 7.8 (a) depicts a crystalline, dendrite-like structure which formed on top of possibly a particulate layer (brown regions), at an area near centre of the deposit pattern seen in Figure 7.3 (a). The resulting structure appears to have propagated from the centre of the deposit (left side of Figure 7.8 (a)) towards the exterior, due to the fact that dendrite formation is a diffusion-limited [105, 106]. The crystallisation mechanism of DNA could be explained as follows: Initially, some DNA strands near

the centre of the drop are adsorbed on the droplet-substrate interface due to the higher population of DNA there and hence probability. These adsorbed strands should then attract and attach other DNA molecules which follow the random walk concept (*i.e.* diffusion), eventually giving rise to the dendrite in the same manner. This could be the reason for the formation of the rather uniform pattern at the centre of the deposit in both 100 bp cases examined, presented in previous section. However, the AFM measurements were conducted after full evaporation of the droplet, therefore it is not possible to determine during which stage of the evaporation process these structures formed [105, 106]. A similar dendrite structure was reported for much smaller DNA strands (8 bp) [114]. Magnification of these crystalline structures (Figure 7.8 (b)) allowed the estimation of their dimensions. An average height profile of the dendrite structure is presented in Figure 7.8 (c) and its thickness was found to be 185.72 ± 25.37 nm.

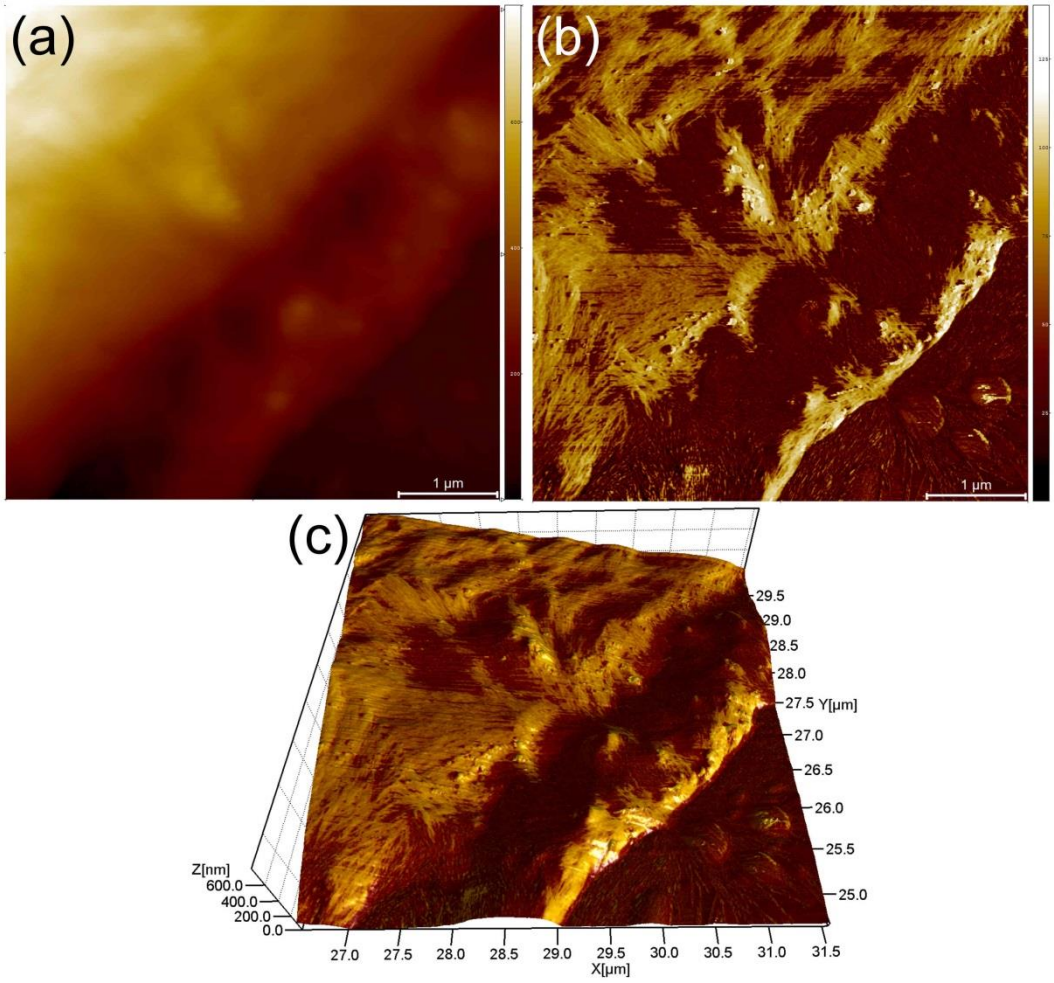

Figure 7.9: (a) 5 × 5 µm^2 topography image of the edge of the coffee-ring (TL) left behind the evaporation of an aqueous droplet containing 0.01 % w/v of 1000 bp DNA strands. (b) Phase image of the same area. (c) 3-D representation combining information from both (a) and (b).

In Figure 7.9 (a) the topography of the edge of the deposit is presented. An initial, rapid dewetting, as discussed above, occurs directly after the deposition as particulate can be seen outside the deposit, bottom right part of Figure 7.9 (a). The corresponding phase image, Figure 7.9 (b), unveils some interesting features on the self-assembly of DNA strands, which can be identified as bright fibrils. For better clarity, in Figure 7.9 (c) the three dimensional representation of the topography of the same area is presented

with an overlay of the phase image. During the initial, rapid dewetting, DNA appears to have self-assembled at the exterior with an orientation perpendicular to the TL, attributable possibly to the rapid motion of the TL stretching the molecules [24, 144, 152]. Evidently, flexible DNA strands follow the previously proposed particle self-assembly mechanism. Within the coffee-ring, the DNA strands appear to have orientated themselves mainly parallel to the edge of the ring, in an attempt to achieve the densest possible packing in the wedge constraints (see section 6.4). Some particles have oriented themselves perpendicular to the deposit edge, possibly due to the retraction of the TL, forcing the strands to align to its motion. Similar undulations of DNA strands oriented parallel to the TL were reported to have formed during the retraction of the TL of droplets containing larger DNA strands, observed with confocal microscopy [113]. Furthermore, a second region with mainly parallel to the TL particle orientations can be identified at a distance of approx. 1.40 microns, indicative of the fact that possibly the depinning of the TL does not happen “instantaneous”, thus allowing some degree of particle orientation. Away from the TL, near the top left corner of Figure 7.9 (a), DNA strands exhibit a mixture of orientations parallel and perpendicular to the TL as the wedge constraints become weaker and some particles can align to the flow (see section 6.4).

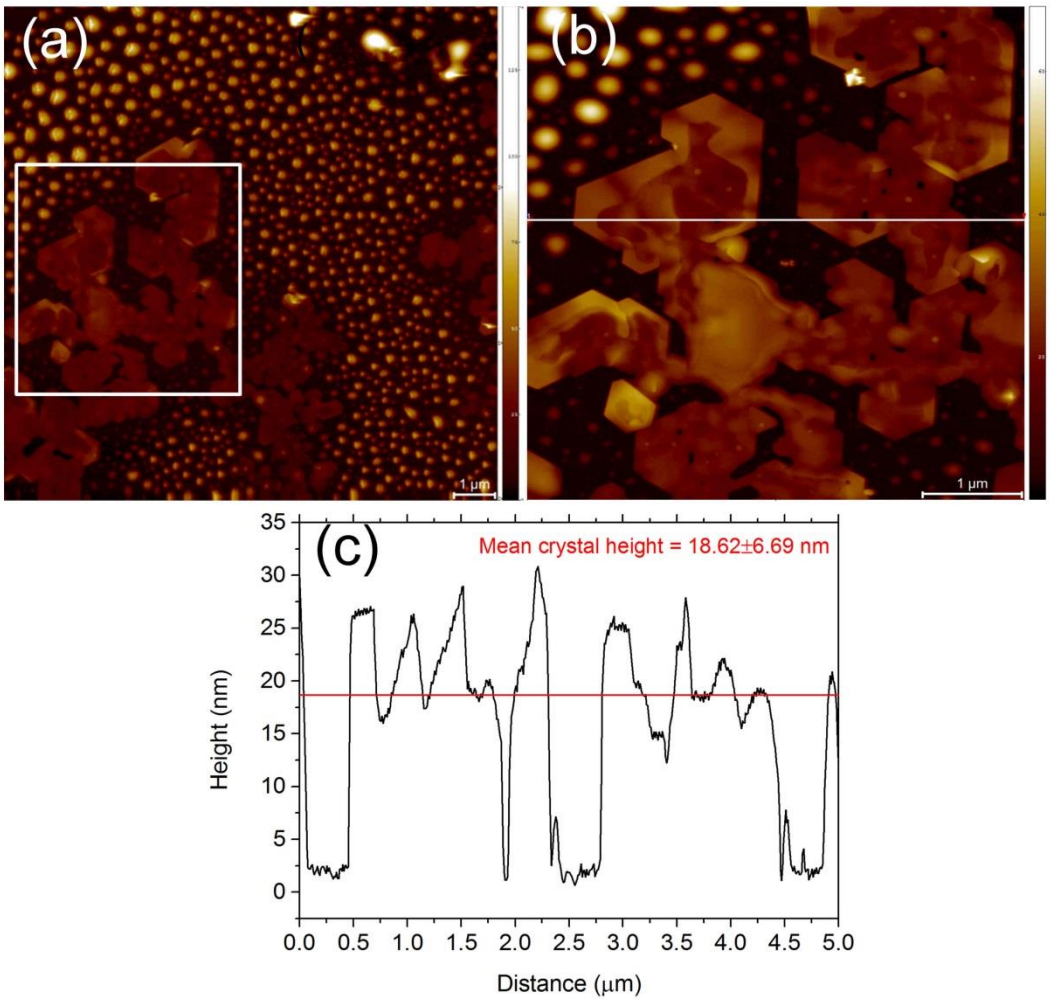

Figure 7.10: (a) 15.0 × 15.0 µm^2 topography image of the central area of the resulting pattern the 0.01 % w/v 1000 bp *without* EDTA case. (b) 5 × 5 µm^2 magnification of the area in the box in (a). (c) Mean height profile corresponding to line in (b).

Figure 7.10 (a) depicts the topography image of the area formed at the centre of the pattern of the 1000 bp without EDTA sample, seen in Figure 7.3 (c). A number of spherical particle aggregates/islands can be easily discerned to have deposited randomly around what appears to be a network of structures with sharp edges. These islands are typical pseudo-dewetting structures (as the surface is still covered by liquid) [106, 153, 154]. Once a sufficient amount of these islands are found in close proximity,

the network with the sharp edges is formed. The propagation and the sharp edges of this network are indicative of particle crystallisation following "faceted growth" [107, 155]. Magnification on these crystalline structures (in Figure 7.10 (b)) allowed the estimation of their dimensions. The average height of the crystals was found to be 18.62 ± 6.69 nm, presented in in Figure 7.10 (c). Lateral dimensions varied which is readily apparent in Figure 7.10 (a). Notably, these crystalline structures are different than the structures observed at the interior of the 100 bp without EDTA case (Figure 7.8), indicating the flexibility effect on the crystallisation process.

7.4. Conclusions

Particle flexibility was found to play a major role in the evaporation process of sessile droplets containing DNA strands. DNA strands namely rigid (100 bp) and flexible (1000 bp), dissolved in aqueous solutions with and without EDTA, were examined. The base fluid, water with 1 mM EDTA, evaporated following an initial CCR stage, which then transitioned into simultaneously decreasing θ and R, and consequently into a second CCR until full evaporation. The addition of the rigid DNA molecules resulted in CCR evaporation throughout the process. On the other hand, the more flexible 1000 bp strands, showed an evaporative behaviour similar to the base fluid. In the absence of EDTA, both the droplets containing the rigid and those containing the flexible strands evaporated following the same behaviour of initial CCR, then simultaneously decreasing of θ and R and a second CCR periods.

Resulting deposit patterns varied widely, as EDTA was found to interfere with DNA mobility. In the absence of EDTA, regular coffee-rings were formed, with flexible strands leading to wider rings. Quantification of the energy barrier pinning the droplets allowed some insight into the TL motion kinetics. In essence, the more rigid particles require higher amounts of energy for (any) depinning to occur.

Additionally, the self-assembly behaviour of the strands within the resulting patterns was investigated. The base fluid, EDTA in water, resulted in the formation of fibril like structures which rendered the identification of DNA structuring impossible. On the other hand, both strands in pure DNA solutions showed different self-assembly behaviours, owing to their different degree of flexibility. To the best of our knowledge, this is the first report of particle flexibility on coffee-stain formation. Still, further experimentation with more DNA chain lengths are required to fully probe the issue.

Chapter 8 Conclusions and Future work

8.1. Conclusions

Nanoparticle addition in evaporating sessile droplets resulted in unexpected results. A disordering region formed at the exterior part of the coffee-ring which has not been predicted or reported in the past. Experimentation with various deposition rates, controlled by lowering environmental pressure and hence increasing evaporation rate, allowed the promotion of crystallinity in the same region. Coupling experimental information with theoretical arguments allowed the proposition of a tentative particle self-assembly mechanism with mainly two components. Particle velocity was found to be the main ordering parameter whereas wedge constraints/disjoining pressure was the main disordering parameter.

The applicability of the proposed particle self-assembly mechanism was tested further for more pressures. Interestingly, a limit on the deposition rate was found after which disordered patterns within the ring-stains appeared. This allowed us to propose a "recipe" for acquiring the best possible crystalline coffee-rings. Moreover, a power law relationship between pressure and evaporation for the nanofluid in question was found. Additionally, the hysteretic energy barrier pinning each droplet was calculated for all pressure and was found to be proportional to evaporation rate.

Having established a "recipe" for the production of crystalline coffee-rings we then attempted to investigate if various particle geometries abide to it. The evaporation and self-assembly behaviours of various particle shapes, categorised according to aspect ratio, were compared. In short, nanospheres, graphene platelets and carbon nanotubes

were examined. We found that the pinning strength increased with aspect ratio. In addition, we thoroughly investigated the nanostructuring of each case with extra attention to the graphene structuring. We found that the particle self-assembly mechanism we proposed is applicable to all particle shapes giving it a universal character.

Particle flexibility was the last parameter investigated and was found to be of paramount importance to the coffee-stain mechanism and the resulting patterns. Rigid and flexible particles evaporated differently and resulted in different deposit patterns. Comparison of the excess free energy accumulating in each system showed particle flexibility and hysteretic pinning barrier to be inversely proportional. Nanoscale investigation unveiled further indications of the importance of particle flexibility. Rigid particles exhibited no crystallinity at the edge of the coffee-ring whereas flexible particles followed the universal self-assembly mechanism we proposed. Interestingly, at the interior of the droplets each particle crystallised following a different path.

8.2. Future work

Although, the evaporation behaviour and nano-structuring of various particle shapes and other physical parameters of the processes were thoroughly investigated in this study, various questions remain elusive. In this section, concepts for future research are presented next. For example, the exact limit of particle diameter for the formation

of a disordered region at the edge of coffee-rings should be examined. This could allow the refinement of the proposed particle self-assembly mechanism.

Knowing the dimensions of the particulate deposit and the distance from the actual liquid front allows the indirect determination of the dimensions of the precursor film Additionally, verification with yet smaller, in diameter, particles as they could reach even closer to the actual liquid front is desirable as it could potentially allow even more accurate measurement of the precursor film dimensions. Knowing these dimensions should have a major impact on the modelling of droplets, may they be binary mixtures, suspensions etc.

Having established a simple, yet applicable, particle self-assembly mechanism, further research into the nanostructuring of various particle shapes, e.g. graphene flakes and rods, within the same coffee-ring should be conducted. Furthermore, the effect of surfactants on the particulate self-assembly mechanism should be assessed. Potentially, knowing the above could lead into various nano-technological applications where bottom-up self-assembly is required, such as inkjet printing and optoelectronics.

Furthermore, the behaviour of nanoparticles at the interface of a binary mixture of two different in volatility liquids should be investigated. This information could potentially be applied in heat transfer industrial applications where particle sedimentation and hence pipe clogging is not welcome.

The study on DNA is rather inconclusive. Therefore, more DNA lengths should be investigated in order to fully comprehend the effect of particle flexibility on the resulting patterns. As the addition of EDTA proved to affect the flexibility of the chains and hence particle self-assembly, various concentrations of this molecule and of various salts, *i.e.* NaCl, producing cations should be investigated. This study could potentially lead to bio-sensing applications amongst others.

Another area of molecules with interesting characteristics is that of polymers. Polymers can be varied in composition, sizes, branching etc., therefore the effect of them on coffee-stain formation and the resulting patterns should be probed. Applications of such systems could vary widely from photovoltaics to bio-medical, to name but a few.

References

1. Young, T., *An Essay on the Cohesion of Fluids.* Philosophical Transactions of the Royal Society of London, 1805. **95**: p. 65-87.
2. Joanny, J.F. and P.G. de Gennes, *A model for contact angle hysteresis.* The Journal of Chemical Physics, 1984. **81**(1): p. 552-562.
3. de Gennes, P.G., *Wetting: statics and dynamics.* Reviews of Modern Physics, 1985. **57**(3): p. 827-863.
4. Xia, Y. and G.M. Whitesides, *Soft lithography.* Annual review of materials science, 1998. **28**(1): p. 153-184.
5. Squires, T.M. and S.R. Quake, *Microfluidics: Fluid physics at the nanoliter scale.* Reviews of modern physics, 2005. **77**(3): p. 977-1026.
6. Reiter, G., *Dewetting of thin polymer films.* Physical Review Letters, 1992. **68**(1): p. 75-78.
7. Bourgesmonnier, C. and M.E.R. Shanahan, *Influence of Evaporation on Contact-Angle.* Langmuir, 1995. **11**(7): p. 2820-2829.
8. Mangel Jr, R.F. and E. Baer, *The evaporation of water drops from a "Teflon" surface.* Chemical Engineering Science, 1962. **17**(9): p. 705-706.
9. Picknett, R.G. and R. Bexon, *The evaporation of sessile or pendant drops in still air.* Journal of Colloid and Interface Science, 1977. **61**(2): p. 336-350.
10. Birdi, K.S., D.T. Vu, and A. Winter, *A study of the evaporation rates of small water drops placed on a solid surface.* The Journal of Physical Chemistry, 1989. **93**(9): p. 3702-3703.
11. Birdi, K.S. and D.T. Vu, *Wettability and the evaporation rates of fluids from solid surfaces.* Journal of Adhesion Science and Technology, 1993. **7**(6): p. 485-493.
12. Hu, H. and R.G. Larson, *Evaporation of a Sessile Droplet on a Substrate.* J. Phys. Chem. B, 2002. **106**(6): p. 1334-1344.
13. Shanahan, M.E.R. and C. Bourges, *Effects of Evaporation on Contact Angles on Polymer Surfaces.* International Journal of Adhesion and Adhesives, 1994. **14**(3): p. 201-205.
14. Sefiane, K., et al., *On the effect of the atmosphere on the evaporation of sessile droplets of water.* Physics of Fluids, 2009. **21**(6): p. 062101-062109.
15. Mollaret, R., et al., *Experimental and Numerical Investigation of the Evaporation into Air of a Drop on a Heated Surface.* Chemical Engineering Research and Design, 2004. **82**(4): p. 471-480.
16. Hu, H. and R.G. Larson, *Analysis of the effects of Marangoni stresses on the microflow in an evaporating sessile droplet.* Langmuir, 2005. **21**(9): p. 3972-3980.
17. Paik, S.W., et al., *Spatially and temporally resolved temperature measurements for slow evaporating sessile drops heated by a microfabricated heater array.* Journal of Heat Transfer-Transactions of the Asme, 2007. **129**(8): p. 966-976.
18. Wong, K.V. and O. De Leon, *Applications of Nanofluids: Current and Future.* Advances in Mechanical Engineering, 2010.

19. Deegan, R.D., et al., *Capillary flow as the cause of ring stains from dried liquid drops.* Nature, 1997. **389**(6653): p. 827-829.
20. Deegan, R.D., et al., *Contact line deposits in an evaporating drop.* Phys. Rev. E, 2000. **62**(1): p. 756-765.
21. Deegan, R.D., *Pattern formation in drying drops.* Phys. Rev. E, 2000. **61**(1): p. 475-485.
22. Singh, M., et al., *Inkjet Printing—Process and Its Applications.* Advanced Materials, 2010. **22**(6): p. 673-685.
23. Carmeli, I., et al., *Photovoltaic Activity of Photosystem I-Based Self-Assembled Monolayer.* Journal of the American Chemical Society, 2007. **129**(41): p. 12352-12353.
24. Heim, T., et al., *Deposition from a drop: morphologies of unspecifically bound DNA.* Journal of Physics: Condensed Matter, 2005. **17**(9): p. S703.
25. Sefiane, K., *On the Formation of Regular Patterns from Drying Droplets and Their Potential Use for Bio-Medical Applications.* Journal of Bionic Engineering, 2010. **7**(0): p. S82-S93.
26. Brutin, D., et al., *Pattern formation in drying drops of blood.* Journal of Fluid Mechanics, 2011. **667**: p. 85-95.
27. Bou Zeid, W. and D. Brutin, *Influence of relative humidity on spreading, pattern formation and adhesion of a drying drop of whole blood.* Colloids and Surfaces A: Physicochemical and Engineering Aspects, 2013. **430**(0): p. 1-7.
28. Kao, M., et al., *Copper-oxide brake nanofluid manufactured using arc-submerged nanoparticle synthesis system.* Journal of Alloys and Compounds, 2007. **434**: p. 672-674.
29. Donzelli, G., R. Cerbino, and A. Vailati, *Bistable heat transfer in a nanofluid.* Physical review letters, 2009. **102**(10): p. 104503-1-4.
30. Han, Z., F. Cao, and B. Yang, *Synthesis and thermal characterization of phase-changeable indium/polyalphaolefin nanofluids.* Applied Physics Letters, 2008. **92**(24): p. 243104-1-3.
31. Ma, H., et al., *Effect of nanofluid on the heat transport capability in an oscillating heat pipe.* Applied Physics Letters, 2006. **88**(14): p. 143116-1-3.
32. Ma, H., et al., *An experimental investigation of heat transport capability in a nanofluid oscillating heat pipe.* Journal of Heat Transfer, 2006. **128**(11): p. 1213-1216.
33. Wasan, D.T. and A.D. Nikolov, *Spreading of nanofluids on solids.* Nature, 2003. **423**(6936): p. 156-159.
34. Matar, O.K., R.V. Craster, and K. Sefiane, *Dynamic spreading of droplets containing nanoparticles.* Physical Review E, 2007. **76**(5): p. 056315-1-9.
35. Craster, R.V., O.K. Matar, and K. Sefiane, *Pinning, Retraction, and Terracing of Evaporating Droplets Containing Nanoparticles.* Langmuir, 2009. **25**(6): p. 3601-3609.
36. Orejon, D., K. Sefiane, and M.E.R. Shanahan, *Stick-Slip of Evaporating Droplets: Substrate Hydrophobicity and Nanoparticle Concentration.* Langmuir, 2011. **27**(21): p. 12834-12843.

37. Orejon, D., K. Sefiane, and M.E.R. Shanahan, *Evaporation of nanofluid droplets with applied DC potential.* Journal of Colloid and Interface Science, 2013. **407**(0): p. 29-38.
38. Orejon, D., K. Sefiane, and M.E.R. Shanahan, *Young-Lippmann equation revisited for nano-suspensions.* Applied Physics Letters, 2013. **102**(20): p. 201601-1-3.
39. Sefiane, K. and R. Bennacer, *Nanofluids droplets evaporation kinetics and wetting dynamics on rough heated substrates.* Advances in Colloid and Interface Science, 2009. **147-48**: p. 263-271.
40. Sefiane, K., *Patterns from drying drops.* Advances in Colloid and Interface Science, 2014. **206**(0): p. 372-381.
41. Denkov, N.D., et al., *2-dimensional crystallisation.* Nature, 1993. **361**(6407): p. 26-26.
42. Cong, H. and W.X. Cao, *Colloidal crystallization induced by capillary force.* Langmuir, 2003. **19**(20): p. 8177-8181.
43. Abkarian, M., J. Nunes, and H.A. Stone, *Colloidal Crystallization and Banding in a Cylindrical Geometry.* J. Am. Chem. Soc., 2004. **126**(19): p. 5978-5979.
44. Meng, L.L., et al., *The role of thickness transitions in convective assembly.* Nano Lett., 2006. **6**(10): p. 2249-2253.
45. Schöpe, H.J., et al., *Fast microscopic method for large scale determination of structure, morphology, and quality of thin colloidal crystals.* Langmuir, 2006. **22**(4): p. 1828-1838.
46. Brewer, D.D., et al., *Mechanistic Principles of Colloidal Crystal Growth by Evaporation-Induced Convective Steering.* Langmuir, 2008. **24**(23): p. 13683-13693.
47. Askounis, A., et al., *Structural transitions in a ring stain created at the contact line of evaporating nanosuspension sessile drops.* Physical Review E, 2013. **87**(1): p. 012301-1-8.
48. Askounis, A., et al., *The effect of evaporation kinetics on nanoparticle structuring within contact line deposits of volatile drops.* Colloids and Surfaces A: Physicochemical and Engineering Aspects, 2014. **441**(0): p. 855-866.
49. Marín, A.G., et al., *Order-to-Disorder Transition in Ring-Shaped Colloidal Stains.* Phys. Rev. Lett., 2011. **107**(8): p. 085502-085505.
50. Asher, S.A., et al., *Photonic Crystal Carbohydrate Sensors: Low Ionic Strength Sugar Sensing.* Journal of the American Chemical Society, 2003. **125**(11): p. 3322-3329.
51. Lu, Y., et al., *Nanophotonic Crescent Moon Structures with Sharp Edge for Ultrasensitive Biomolecular Detection by Local Electromagnetic Field Enhancement Effect.* Nano Letters, 2004. **5**(1): p. 119-124.
52. Xia, Y., et al., *Monodispersed Colloidal Spheres: Old Materials with New Applications.* Advanced Materials, 2000. **12**(10): p. 693-713.
53. Hayashi, S., et al., *Imaging by polystyrene latex particles.* Journal of Colloid and Interface Science, 1991. **144**(2): p. 538-547.

54. Hulteen, J.C., et al., *Nanosphere Lithography: Size-Tunable Silver Nanoparticle and Surface Cluster Arrays.* The Journal of Physical Chemistry B, 1999. **103**(19): p. 3854-3863.
55. Haynes, C.L. and R.P. Van Duyne, *Nanosphere lithography: A versatile nanofabrication tool for studies of size-dependent nanoparticle optics.* Journal of Physical Chemistry B, 2001. **105**(24): p. 5599-5611.
56. Green, M., et al., *Quantum pillar structures on n+ gallium arsenide fabricated using ''natural'' lithography.* Applied Physics Letters, 1993. **62**(3): p. 264-266.
57. Dupré, A. and P. Dupré, *Théorie mécanique de la chaleur*. 1869: Gauthier-Villars.
58. Schwartz, L.W. and S. Garoff, *Contact angle hysteresis on heterogeneous surfaces.* Langmuir, 1985. **1**(2): p. 219-230.
59. Israelachvili, J.N. and M.L. Gee, *Contact angles on chemically heterogeneous surfaces.* Langmuir, 1989. **5**(1): p. 288-289.
60. Woodward, J.T., H. Gwin, and D.K. Schwartz, *Contact Angles on Surfaces with Mesoscopic Chemical Heterogeneity.* Langmuir, 2000. **16**(6): p. 2957-2961.
61. Wenzel, R.N., *Resistance of solid surfaces to wetting by water.* Industrial & Engineering Chemistry, 1936. **28**(8): p. 988-994.
62. Cassie, A.B.D. and S. Baxter, *Wettability of porous surfaces.* Transactions of the Faraday Society, 1944. **40**(0): p. 546-551.
63. Johnson Jr, R.E., R.H. Dettre, and D.A. Brandreth, *Dynamic contact angles and contact angle hysteresis.* Journal of Colloid and Interface Science, 1977. **62**(2): p. 205-212.
64. Yuan, Y. and T.R. Lee, *Contact Angle and Wetting Properties*, in *Surface Science Techniques*, G. Bracco and B. Holst, Editors. 2013, Springer Berlin Heidelberg. p. 3-34.
65. Timmons, C.O. and W.A. Zisman, *The effect of liquid structure on contact angle hysteresis.* Journal of Colloid and Interface Science, 1966. **22**(2): p. 165-171.
66. Chaudhury, M.K. and G.M. Whitesides, *Correlation Between Surface Free Energy and Surface Constitution.* Science, 1992. **255**(5049): p. 1230-1232.
67. Good, R.J., *Contact angle, wetting, and adhesion: a critical review.* Journal of Adhesion Science and Technology, 1992. **6**(12): p. 1269-1302.
68. Robbins, M.O. and J.F. Joanny, *Contact Angle Hysteresis on Random Surfaces.* EPL (Europhysics Letters), 1987. **3**(6): p. 729-735.
69. Heslot, F., A.M. Cazabat, and P. Levinson, *Dynamics of wetting of tiny drops: Ellipsometric study of the late stages of spreading.* Physical Review Letters, 1989. **62**(11): p. 1286-1289.
70. Hazareesing, A. and M. Mézard, *Wandering of a contact line at thermal equilibrium.* Physical Review E, 1999. **60**(2): p. 1269-1278.
71. Bonn, D., et al., *Wetting and spreading.* Reviews of Modern Physics, 2009. **81**(2): p. 739-805.

72. Shanahan, M.E.R., *Meniscus shape and contact angle of a slightly deformed axisymmetric drop.* Journal of Physics D: Applied Physics, 1989. **22**(8): p. 1128.
73. Shanahan, M.E.R., *Simple Theory of "Stick-Slip" Wetting Hysteresis.* Langmuir, 1995. **11**(3): p. 1041-1043.
74. Drelich, J., *The significance and magnitude of the line tension in three-phase (solid-liquid-fluid) systems.* Colloids and Surfaces A: Physicochemical and Engineering Aspects, 1996. **116**(1–2): p. 43-54.
75. Shanahan, M.E.R. and K. Sefiane, *Kinetics of triple line motion during evaporation,* in *Contact Angle, Wettability and Adhesion*, K.L. Mittal, Editor. 2009, Koninklijke Brill NV: Leiden. p. 19-32.
76. Wang, J.Y., S. Betelu, and B.M. Law, *Line tension approaching a first-order wetting transition: Experimental results from contact angle measurements.* Physical Review E, 2001. **63**(3): p. 031601-1-11.
77. Nguyen, T.A.H., et al., *Theoretical and experimental analysis of droplet evaporation on solid surfaces.* Chemical Engineering Science, 2012. **69**(1): p. 522-529.
78. Duursma, G.R., K. Sefiane, and S. David, *Advancing and receding contact lines on patterned structured surfaces.* Chem. Eng. Res. Des., 2010. **88**(5-6): p. 737-743.
79. Singh, S.K., et al., *Evaporation of sessile droplets on nano-porous alumina surfaces.* AIP Conference Proceedings, 2013. **1547**(1): p. 156-163.
80. Shanahan, M.E.R., K. Sefiane, and J.R. Moffat, *Dependence of Volatile Droplet Lifetime on the Hydrophobicity of the Substrate.* Langmuir, 2011. **27**(8): p. 4572-4577.
81. Hu, H. and R.G. Larson, *Analysis of the microfluid flow in an evaporating sessile droplet.* Langmuir, 2005. **21**(9): p. 3963-3971.
82. Adachi, E., A.S. Dimitrov, and K. Nagayama, *Stripe Patterns Formed on a Glass-Surface During Droplet Evaporation.* Langmuir, 1995. **11**(4): p. 1057-1060.
83. Moffat, J.R., K. Sefiane, and M.E.R. Shanahan, *Effect of TiO2 Nanoparticles on Contact Line Stick-Slip Behavior of Volatile Drops.* J. Phys. Chem. B, 2009. **113**(26): p. 8860-8866.
84. David, S., K. Sefiane, and L. Tadrist, *Experimental investigation of the effect of thermal properties of the substrate in the wetting and evaporation of sessile drops.* Colloids and Surfaces A: Physicochemical and Engineering Aspects, 2007. **298**(1–2): p. 108-114.
85. Uno, K., et al., *Particle adsorption in evaporating droplets of polymer latex dispersions on hydrophilic and hydrophobic surfaces.* Colloid and Polymer Science, 1998. **276**(9): p. 810-815.
86. Chhasatia, V.H., A.S. Joshi, and Y. Sun, *Effect of relative humidity on contact angle and particle deposition morphology of an evaporating colloidal drop.* Applied Physics Letters, 2010. **97**(23): p. 231909-1-3.
87. Brutin, D., *Influence of relative humidity and nano-particle concentration on pattern formation and evaporation rate of pinned drying drops of nanofluids.*

Colloids and Surfaces A: Physicochemical and Engineering Aspects, 2013. **429**(0): p. 112-120.
88. Pieranski, P., L. Strzelecki, and B. Pansu, *Thin colloidal crystals.* Phys. Rev. Lett., 1983. **50**(12): p. 900-903.
89. Neser, S., et al., *Finite-size effects on the closest packing of hard spheres.* Phys. Rev. Lett., 1997. **79**(12): p. 2348-2351.
90. Askounis, A., et al., *The effect of evaporation kinetics on nanoparticle structuring within contact line deposits of volatile drops.* Colloids and Surfaces A: Physicochemical and Engineering Aspects, 2012(Article).
91. Nikolov, A.D. and D.T. Wasan, *Mechanisms of the Assembly of Nano- and Microparticle Two-Dimensional Structures in a Wedge Film.* Industrial & Engineering Chemistry Research, 2009. **48**(5): p. 2320-2326.
92. Sefiane, K., *Patterns from drying drops.* Advances in Colloid and Interface Science, 2013.
93. Askounis, A., et al., *Nanoparticle deposits near the contact line of pinned volatile droplets: size and shape revealed by atomic force microscopy.* Soft Matter, 2011. **7**(9): p. 4152-4155.
94. Yunker, P.J., et al., *Suppression of the coffee-ring effect by shape-dependent capillary interactions.* Nature, 2011. **476**(7360): p. 308-311.
95. Yunker, P.J., et al., *Effects of Particle Shape on Growth Dynamics at Edges of Evaporating Drops of Colloidal Suspensions.* Physical Review Letters, 2013. **110**(3): p. 035501-1-5.
96. Yunker, P.J., D.J. Durian, and A.G. Yodh, *Coffee rings and coffee disks: Physics on the edge.* Physics Today, 2013. **66**(8): p. 60-61.
97. Ming, T., et al., *Ordered Gold Nanostructure Assemblies Formed By Droplet Evaporation.* Angewandte Chemie International Edition, 2008. **47**(50): p. 9685-9690.
98. Xie, Y., et al., *Self-Assembly of Gold Nanorods into Symmetric Superlattices Directed by OH-Terminated Hexa(ethylene glycol) Alkanethiol.* Langmuir, 2011. **27**(18): p. 11394-11400.
99. Nobile, C., et al., *Self-assembly of highly fluorescent semiconductor nanorods into large scale smectic liquid crystal structures by coffee stain evaporation dynamics.* J. Phys.: Condens. Matter, 2009. **21**(26): p. 264013-1-5.
100. Li, Q., et al., *Self-Organization of Carbon Nanotubes in Evaporating Droplets.* The Journal of Physical Chemistry B, 2006. **110**(28): p. 13926-13930.
101. Small, W.R., et al., *Carbon Nanotube Network Formation from Evaporating Sessile Drops.* The Journal of Physical Chemistry B, 2006. **110**(26): p. 13029-13036.
102. Denneulin, A., et al., *Impact of ink formulation on carbon nanotube network organization within inkjet printed conductive films.* Carbon, 2011. **49**(8): p. 2603-2614.
103. Zeng, H., et al., *Surface-Induced Patterns from Evaporating Droplets of Aqueous Carbon Nanotube Dispersions.* Langmuir, 2011. **27**(11): p. 7163-7167.

104. Zhang, S., et al., *Ordering in a Droplet of an Aqueous Suspension of Single-Wall Carbon Nanotubes on a Solid Substrate.* Langmuir, 2009. **26**(3): p. 2107-2112.
105. Witten, T.A. and L.M. Sander, *Diffusion-Limited Aggregation, a Kinetic Critical Phenomenon.* Physical Review Letters, 1981. **47**(19): p. 1400-1403.
106. Reiter, G. and J.-U. Sommer, *Crystallization of Adsorbed Polymer Monolayers.* Physical Review Letters, 1998. **80**(17): p. 3771-3774.
107. Zhang, G., et al., *Dendritic-to-faceted crystal pattern transition of ultrathin poly(ethylene oxide) films.* The Journal of Chemical Physics, 2008. **129**(22): p. 224708-1-6.
108. Zhang, G., et al., *Labyrinthine pattern of polymer crystals from supercooled ultrathin films.* Polymer, 2010. **51**(2): p. 554-562.
109. Taguchi, K., et al., *Growth shape of isotactic polystyrene crystals in thin films.* Polymer, 2001. **42**(17): p. 7443-7447.
110. Jradi, K., et al., *Enhancing nucleation and controlling crystal orientation by rubbing/scratching the surface of a thin polymer film.* The European Physical Journal E, 2009. **29**(4): p. 383-389.
111. Calladine, C.R. and H.R. Drew, *Understanding DNA: the molecule & how it works*. 1997: Academic Press.
112. Hagerman, P.J., *Flexibility of DNA.* Annual review of biophysics and biophysical chemistry, 1988. **17**(1): p. 265-286.
113. Smalyukh, I.I., et al., *Structure and Dynamics of Liquid Crystalline Pattern Formation in Drying Droplets of DNA.* Physical Review Letters, 2006. **96**(17): p. 177801-1-4.
114. Nakata, M., et al., *End-to-End Stacking and Liquid Crystal Condensation of 6–to 20–Base Pair DNA Duplexes.* Science, 2007. **318**(5854): p. 1276-1279.
115. Maeda, H., *An Atomic Force Microscopy Study of Ordered Molecular Assemblies and Concentric Ring Patterns from Evaporating Droplets of Collagen Solutions.* Langmuir, 1999. **15**(24): p. 8505-8513.
116. Novoselov, K.S., et al., *Electric Field Effect in Atomically Thin Carbon Films.* Science, 2004. **306**(5696): p. 666-669.
117. Novoselov, K.S., et al., *A roadmap for graphene.* Nature, 2012. **490**(7419): p. 192-200.
118. Schinwald, A., et al., *Minimal oxidation and inflammogenicity of pristine graphene with residence in the lung.* Nanotoxicology, 2014. **8**(8): p. 824-832.
119. Seabra, A.B., et al., *Nanotoxicity of Graphene and Graphene Oxide.* Chemical Research in Toxicology, 2014. **27**(2): p. 159-168.
120. He, S., et al., *A Graphene Nanoprobe for Rapid, Sensitive, and Multicolor Fluorescent DNA Analysis.* Advanced Functional Materials, 2010. **20**(3): p. 453-459.
121. Kuila, T., et al., *Recent advances in graphene-based biosensors.* Biosensors & Bioelectronics, 2011. **26**(12): p. 4637-4648.
122. Yamaguchi, H., et al., *Highly Uniform 300 mm Wafer-Scale Deposition of Single and Multilayered Chemically Derived Graphene Thin Films.* ACS Nano, 2010. **4**(1): p. 524-528.

123. Stratakis, E., et al., *Plasmonic organic photovoltaic devices with graphene based buffer layers for stability and efficiency enhancement.* Nanoscale, 2013. **5**(10): p. 4144-4150.
124. Stankovich, S., et al., *Graphene-based composite materials.* Nature, 2006. **442**(7100): p. 282-286.
125. Luo, J., et al., *Graphene Oxide Nanocolloids.* Journal of the American Chemical Society, 2010. **132**(50): p. 17667-17669.
126. Shih, C.J., et al., *Bi- and trilayer graphene solutions.* Nature Nanotechnology, 2011. **6**(7): p. 439-445.
127. Monteux, C. and F. Lequeux, *Packing and Sorting Colloids at the Contact Line of a Drying Drop.* Langmuir, 2011. **27**(6): p. 2917-2922.
128. Das, S., S. Chakraborty, and S.K. Mitra, *Ring stains in the presence of electrokinetic interactions.* Physical Review E, 2012. **85**(4): p. 046311-1-8.
129. Popescu, M.N., et al., *Precursor films in wetting phenomena.* Journal of Physics: Condensed Matter, 2012. **24**(24): p. 243102.
130. Shmuylovich, L., A.Q. Shen, and H.A. Stone, *Surface morphology of drying latex films: Multiple ring formation.* Langmuir, 2002. **18**(9): p. 3441-3445.
131. Shanahan, M.E.R. and K. Sefiane, *Kinetics of Triple Line Motion during Evaporation*. Contact Angle, Wettability and Adhesion, Vol 6, ed. K.L. Mittal. 2009, pp. 19-32, Leiden: in: K. L. Mittal, Contact angle, Wettability and Adhesion, Vol 6, Vsp Bv-C/O Brill Acad Publ. 19-32.
132. Wayner, P.C., *Intermolecular forces in phase-change heat transfer: 1998 Kern award review.* AIChE Journal, 1999. **45**(10): p. 2055-2068.
133. Faraudo, J. and F. Bresme, *Stability of particles adsorbed at liquid/fluid interfaces: Shape effects induced by line tension.* The Journal of Chemical Physics, 2003. **118**(14): p. 6518-6528.
134. Bresme, F. and M. Oettel, *Nanoparticles at fluid interfaces.* Journal of Physics: Condensed Matter, 2007. **19**(41): p. 413101-1-33.
135. Duggal, R., F. Hussain, and M. Pasquali, *Self-Assembly of Single-Walled Carbon Nanotubes into a Sheet by Drop Drying.* Advanced Materials, 2006. **18**(1): p. 29-34.
136. Eckstein, E.C. and F. Belgacem, *Model of platelet transport in flowing blood with drift and diffusion terms.* Biophysical Journal, 1991. **60**(1): p. 53-69.
137. Vahidkhah, K., S.L. Diamond, and P. Bagchi, *Hydrodynamic Interaction Between a Platelet and an Erythrocyte: Effect of Erythrocyte Deformability, Dynamics, and Wall Proximity.* Journal of Biomechanical Engineering, 2013. **135**(5): p. 051002-051002.
138. Ploehn, H.J. and C. Liu, *Quantitative Analysis of Montmorillonite Platelet Size by Atomic Force Microscopy.* Industrial & Engineering Chemistry Research, 2006. **45**(21): p. 7025-7034.
139. Stankovich, S., et al., *Synthesis and exfoliation of isocyanate-treated graphene oxide nanoplatelets.* Carbon, 2006. **44**(15): p. 3342-3347.
140. Kim, T.Y., et al., *Self-Organized Graphene Patterns.* Advanced Materials, 2011. **23**(24): p. 2734-2738.

141. Hamamoto, Y., J.R.E. Christy, and K. Sefiane, *Order-of-magnitude increase in flow velocity driven by mass conservation during the evaporation of sessile drops.* Physical Review E, 2011. **83**(5): p. 051602-1-5.
142. Zhurkin, V., et al., *Sequence-Dependent Variability of B-DNA*, in *DNA Conformation and Transcription*. 2005, Springer US. p. 18-34.
143. Gueroult, M., et al., *How cations can assist DNase I in DNA binding and hydrolysis.* PLoS computational biology, 2010. **6**(11): p. e1001000-1-11.
144. Fang, X., et al., *Drying of DNA Droplets.* Langmuir, 2006. **22**(14): p. 6308-6312.
145. Dugas, V., J. Broutin, and E. Souteyrand, *Droplet Evaporation Study Applied to DNA Chip Manufacturing.* Langmuir, 2005. **21**(20): p. 9130-9136.
146. Bezanilla, M., et al., *Adsorption of DNA to Mica, Silylated Mica, and Minerals: Characterization by Atomic Force Microscopy.* Langmuir, 1995. **11**(2): p. 655-659.
147. Bloomfield, V.A., *DNA condensation by multivalent cations.* Biopolymers, 1997. **44**(3): p. 269-282.
148. Askounis, A., et al., *Effect of particle geometry on triple line motion of nano-fluid drops and deposit nano-structuring.* Advances in Colloid and Interface Science, 2014(0).
149. Eaton, P. and P. West, *Atomic Force Microscopy*. 2010: OUP Oxford.
150. Erts, D., et al., *Spatial and Mechanical Properties of Dilute DNA Monolayers on Gold Imaged by AFM.* The Journal of Physical Chemistry B, 2003. **107**(15): p. 3591-3597.
151. Kosaka, P.M., et al., *Atomic force microscopy reveals two phases in single stranded DNA self-assembled monolayers.* Nanoscale, 2013. **5**(16): p. 7425-7432.
152. Li, B., et al., *Macroscopic Highly Aligned DNA Nanowires Created by Controlled Evaporative Self-Assembly.* ACS Nano, 2013. **7**(5): p. 4326-4333.
153. Hare, E.F. and W.A. Zisman, *Autophobic Liquids and the Properties of their Adsorbed Films.* The Journal of Physical Chemistry, 1955. **59**(4): p. 335-340.
154. Kalloudis, M., et al., *Thin Films of Poly(isoprene-b-ethylene Oxide) Diblock Copolymers on Mica: An Atomic Force Microscopy Study.* Langmuir, 2013. **29**(7): p. 2339-2349.
155. Zhang, G., et al., *Morphology Diagram of Single-Layer Crystal Patterns in Supercooled Poly(ethylene oxide) Ultrathin Films: Understanding Macromolecular Effect of Crystal Pattern Formation and Selection.* ACS Macro Letters, 2011. **1**(1): p. 217-221.